New RF Coil Arrays for Static and Dynamic Musculoskeletal Magnetic Resonance Imaging

Dissertation zur Erlangung des naturwissenschaftlichen Doktorgrades der Julius-Maximilians-Universität Würzburg

vorgelegt von

Sairamesh Raghuraman

aus Bangalore (Indien)

Würzburg, 2019

Eingereicht am: ———————

bei der Fakultät für Physik und Astronomie

1. Gutachter: Prof. Dr. Peter Jakob

2. Gutachter: Prof. Dr. Herbert Köstler

3. Gutachter: ———————

der Dissertation

Vorsitzende (r) ———————

1. Prüfer: Prof. Dr. Peter Jakob

2. Prüfer: Prof. Dr. Herbert Köstler

3. Prüfer: Prof. Dr. Haye Hinrichsen

im Promotionkolloquims

Tag des Promotionskolloquiums: 10th of March 2020

Doktorurkunde ausgehändigt am:———————

Contents

List of Figures

Preface

The phenomenon of Nuclear Magnetic Resonance (NMR) has found a range of applications and uses, right from structural determination in chemistry till quantum computing and non-destructive testing. One among these myriad applications is Magnetic Resonance Imaging (MRI) of human bodies. Over the last few decades, MRI has proven itself as a powerful non-invasive imaging modality, offering excellent soft-tissue contrast and resolution. With decades of scientific research and development, it has emerged as an essential diagnostic tool found in all major hospitals and medical research centres throughout the world.

One of the areas, where diagnosis with MRI is crucial is Musculoskeletal imaging. Musculoskeletal (MSK) MR imaging refers mainly to the use of MR techniques to image connective tissues in joints of the human body. Recognised for its potential in the early years of MRI, scientific progress has led to the development of dedicated MR scanners, sequences, and associated hardware & accessories. Despite the above, there is still a tremendous need and scope to improve imaging and diagnosis. Increased spatial resolution is demanded to achieve ultra high resolution necessary to comprehend diseases like Rheumatoid Arthritis (RA) and Hand OsteoArthritis (HOA) that affect tens of millions of lives. New techniques with high temporal resolution are being developed that can image joints in motion, to give additional insights into affected or treated region. Developing optimized RF coils as part of these techniques, are of significant interest due to the

scope they offer and their place in the RF chain.

RF coils's importance in the acquisition/reconstruction chain is due to the fact that they have the ability to transform the inherent SNR of the MR imaging experiment into a practical measure and set the base standard for subsequent components and processors. RF coils have to be tailor made for specific applications, taking into account a variety of factors like SNR, penetration depth and the extent of parallel imaging required. A whole lot of coil types and configurations have been developed and are being developed for sophisticated imaging applications involving low and high field strengths.

In this work, new RF coil arrays for MRI have been developed and optimized for dynamic imaging of the knee of an animal model and human beings, to study regenerated/re-engineered ligaments and joint mechanics. The coils have been constructed in a systematic way taking into account the factors mentioned above, to have an optimum spatio-temporal resolution. The constructed coils are electrically characterized and the results are presented. A new coil configuration is proposed and constructed to image human hand and wrist in ultra high resolution at 7 T.

In this thesis report, apart from the results presented, there are a couple of chapters devoted to basics, from which one can expect to get a fair knowledge of MRI RF coils and their construction techniques.

Is there, I ask, can there be, a more interesting study than that of alternating currents?

- Nikola Tesla

.

.

.

.

May the field be with you

Chapter 1

Basics - NMR, MRI and RF coils

The origins of Nuclear Magnetic Resonance (NMR) started with the seminal paper published by Rabi et. al. [1] in which the nuclear magnetic moments of Lithium nuclei are determined by measuring their frequencies of precession in a static magnetic field. An oscillating magnetic field perpendicular to the static field, at the frequency of precession, i.e. Larmor frequency, is used to effect the transitions between energy levels corresponding to different orientations of nuclear spin. Continuing his work, Purcell and Bloch observed the same in solid materials containing protons, thereby laying the foundation for a whole new field, NMR, that is being widely used for a whole range of purposes. The following sections describe in short, the physics of NMR followed by an introduction to the principles of Magnetic Resonance Imaging (MRI) and RF coils.

1.1 The phenomenon of NMR

Atomic nuclei of various elements and isotopes, have intrinsic nuclear angular momentum characterized by a distinct quantum mechanical property called 'spin' or spin quantum number. Depending on the number of protons and neutrons, the spin quantum number can either be zero, a fraction or an integer. Table 1.1 below shows the spin quantum numbers of certain nuclei relevant for MR imaging and spectroscopy.

The rules of Quantum Mechanics state that a nucleus of spin I will have 2I + 1 states of energy. For e.g. a proton (^{1}H) with a nuclear spin of 1/2 will have 2 energy states.

Nuclei	Nuclear Spin	$\gamma/2\pi$ in MHz/T
^{1}H	1/2	42.58
^{13}C	1/2	10.71
^{19}F	1/2	40.08
^{23}Na	3/2	11.27
^{31}P	1/2	17.25

Table 1.1: ***Nuclear spin and Gyromagnetic ratio ($\gamma/2\pi$) of certain nuclei:*** *While the Gyromagnetic ratio of the shown nuclei are positive, there are nuclei having negative gyromagnetic ratio, the magnetization of which would precess in a direction opposite to that of the other nuclei*

In the presence of an external field, as shown in figure 1.1, Zeeman splitting causes the magnetic moment of the lower energy state + 1/2 to get aligned with the field and the magnetic moment of the higher energy state - 1/2 to get aligned opposite to the field.

The difference in the above states of energy is

$$\Delta E = \gamma \hbar B_0 \tag{1.1}$$

As seen above, this difference is proportional to the external applied magnetic field (B_0). In normal conditions, the number of spins in the lower energy (parallel) state, is slightly more than that of the spins in the upper energy (anti - parallel) state, as given by the following equation:

$$\frac{N_{+1/2\,parallel}}{N_{-1/2\,antiparallel}} = e^{\frac{\Delta E}{k_B T}} \tag{1.2}$$

where k_B is the Boltzman's constant and T is the absolute temperature.

As a first approximation, the above equation can be written as

$$\frac{N_{+1/2\,parallel}}{N_{-1/2\,antiparallel}} = 1 + \frac{\Delta E}{k_B T} \tag{1.3}$$

From the above equation, the difference in the number of spins between the lower and

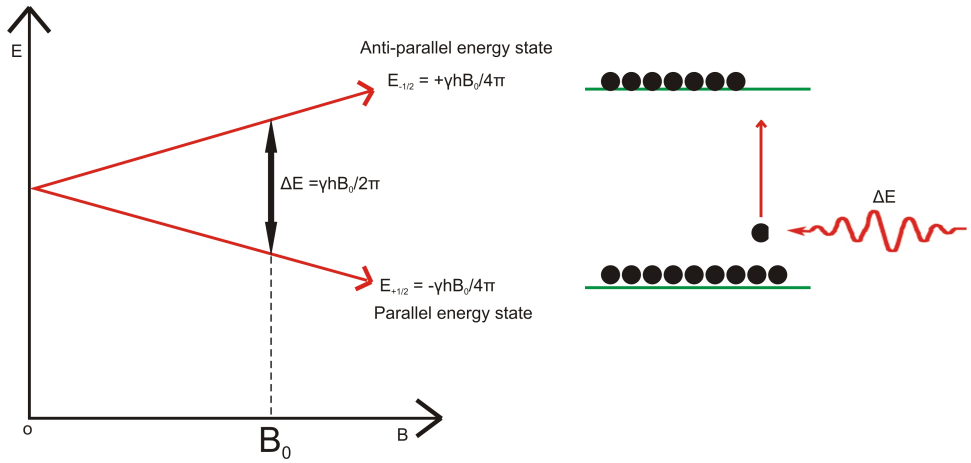

Figure 1.1: ***Zeeman split of the energy levels of proton in the presence of an external magnetic field:*** *The difference between the energy levels ΔE is proportional to the applied external field B_0 as shown in the graph on the left. A photon of energy equal to the energy difference, can be used to transition the spins from the lower energy state to the higher energy state, as shown on the right.*

upper energy states is,

$$N_{parallel} - N_{antiparallel} = N_{antiparallel} * \frac{\Delta E}{k_B T} \approx \frac{N_s \Delta E}{2 k_B T} \tag{1.4}$$

where N_s refers to the total number of spins in a volume.

The above equation can be rewritten using Eq: 1.1 as

$$N_{parallel} - N_{antiparallel} \approx \frac{N_s \gamma \hbar B_0}{2 k_B T} = \frac{N_s \gamma h B_0}{4 \pi k_B T} \tag{1.5}$$

The signal observed in NMR is proportional to the above difference between the number of spins in the lower energy state and the number of spins in the higher energy state. At the moment, a clinically approved MRI scanner, is manufactured only up to a field strength of 3 T and at this field strength, the fraction of spins that contribute to a useful MR signal at room temperature is only up to 10 ppm [1]. This one little calculation would prove beyond doubt to any reader that the entire NMR (including its most important application in the world - Magnetic Resonance Imaging) is a *fight* for the signal.

[1] this number varies depending on the nucleus that is used in the experiment

As can be seen from Eq: 1.1, the difference in energy between the two states can correspond to an angular frequency given by the following equation.

$$\Delta E = h\nu = \gamma\hbar B_0 \tag{1.6}$$

$$\Rightarrow \omega = \gamma B_0 \tag{1.7}$$

From the above equation, it can be inferred that a transition of a spin from one state to another can be effected by introducing a photon whose energy corresponds to the difference in energy between the two states. To put in other words, the transition can be effected by a photon whose angular frequency equals the one given in Eq: 1.7. Upon removal of the photon, the spin which has 'transitioned' to the higher energy anti-parallel state, 'relaxes' to the lower energy state, releasing energy, which is again equal to the difference in energy between the two states.

The whole NMR experiment is about capturing this released energy, from an ensemble of spins and characterizing the nature of the material based on the relaxation.

The above phenomenon can also be described in classical physics perspective as follows. ^{1}H protons immersed in a static magnetic field (B_0) have the magnetization aligned along the direction of the static field (or in the direction opposite to the static field). The transverse component of the magnetization precesses around the B_0 field at an angular frequency given by Eq: 1.7. Upon application of a dynamic magnetic field perpendicular to B_0, at this angular frequency, the magnetization vector is moved away from its equilibrium state, as shown in figure 1.2, at an angle that is proportional to the applied magnetic field, described by the below equation.

$$\alpha = \int_0^t \gamma B_1^+ \, \mathrm{d}t \tag{1.8}$$

In the above equation, α is referred as Flip Angle - the angle by which the magnetization vector is tipped from the longitudinal axis towards the transverse plane and B_1^+ refers to the rotating component of the magnetic field applied perpendicular to the B_0 static field. This rotating component, as will be explained in further sections, is assumed to

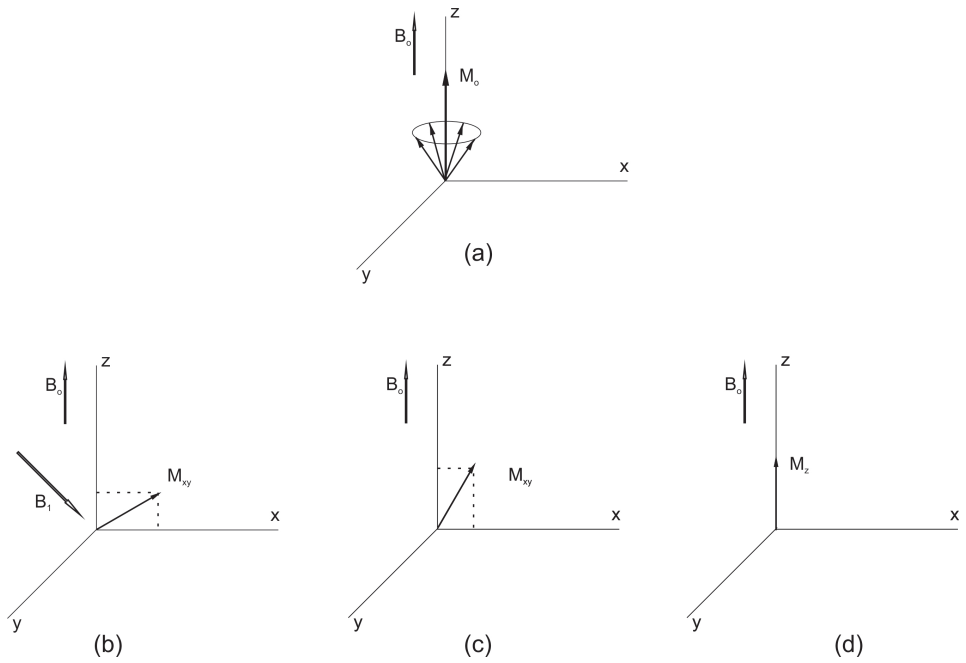

Figure 1.2: ***Change in Macroscopic Magnetization M_0 upon application of RF field B_1:*** *The Magnetization M is oriented along Z axis under the influence of the field B_0 (a). The application of the RF field B_1 tilts the Macroscopic Magnetization to XY plane resulting in the development of M_{xy} (b). Upon the removal of the RF field, the Magnetization relaxes back to Z axis (c and d).*

rotate along the direction of precession of magnetization, i.e. clockwise or anti-clockwise. The change in the magnetization vector, upon application of B_1, can be represented by the following equation:

$$\frac{d\vec{M}}{dt} = \gamma\vec{M} \times \vec{B}_{tot} \tag{1.9}$$

where B_{tot} is the net effective magnetic field ($= B_0 + B_1$).

Expanding the above vector cross product leads to the following equations,

$$\begin{aligned} \frac{dM_x}{dt} &= \gamma(M_y B_0 - M_z B_y) \\ \frac{dM_y}{dt} &= \gamma(-M_x B_0 + M_z B_x) \\ \frac{dM_z}{dt} &= \gamma(M_x B_y - M_y B_x) \end{aligned} \tag{1.10}$$

where as per convention the component B_z has been replaced by the static field B_0.

In MR experiments, the magnetic field B_1 applied perpendicular to the static field B_0, is present for a very short time. Upon removal of this field, the magnetization doesn't

remain tilted, but rather relaxes to its equilibrium along z-axis, which is characterized by first-order time constants T_1 and T_2. The time constant T_1, known as longitudinal or spin-lattice relaxation time, characterizes the rate at which the component of M parallel to the static field, i.e. M_z returns to equilibrium (i.e. the re-growth of longitudinal magnetization). The time constant T_2, known as transverse or spin-spin relaxation time characterizes the rate of decay of the transverse components of magnetization, M_x and M_y, due to loss in phase coherence (or de-correlation) of spins caused by variations in local precession frequencies. Taking into account these relaxation times, Felix Bloch re-formulated the above equations [2] as

$$\begin{aligned} \frac{dM_x}{dt} &= \gamma(M_y B_0 - M_z B_y) - \frac{M_x}{T_2} \\ \frac{dM_y}{dt} &= \gamma(-M_x B_0 + M_z B_x) - \frac{M_y}{T_2} \\ \frac{dM_z}{dt} &= \gamma(M_x B_y - M_y B_x) - \frac{M_x - M_0}{T_1} \end{aligned} \tag{1.11}$$

The equations shown in 1.11 completely characterize the way in which the magnetization evolves in an NMR experiment. Bloch also showed that the rotating magnetization M_{xy} can induce an RF signal in a coil placed along y axis, even if the field B_1 is produced by a coil oriented along x axis. The induced signal can be detected to give the NMR spectrum.

1.2 Magnetic Resonance Imaging

Nuclear Magnetic Resonance and spectroscopy, the basics of which were explained in brief in the last section, had found widespread acceptance and applications in multiple fields of research. But it wasn't until 70s that scientists like Lauterbur, Mansfield and Damadian ([3], [4] and [5]) realized that the relaxation times of protons in combination with spatially varying static fields can be used to characterize tissues within human body and ultimately image it. Soon after, rapid advances in instrumentation and techniques led to the whole new field of Magnetic Resonance Imaging (MRI), the usage of which led to MRI (and hence NMR) being recognized as one of the fundamental tools in medical diagnosis. This section explains in brief, as to how the concept of NMR was used to

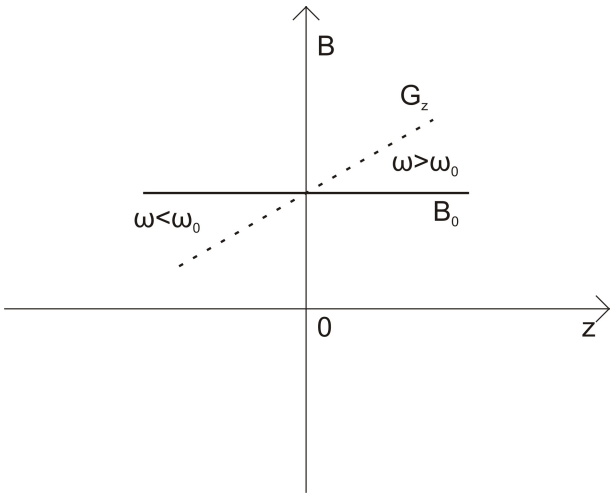

Figure 1.3: ***Z gradient field:*** *Z-gradient G_z shown by dotted lines spatially superimposed over the static field B_0 shown by the dark line. While the applied field B_0 causes the spins to have a proportional precession frequency ω_0, application of the gradient field causes the frequency to vary linearly over the Field Of View.*

conceive MRI.

It is known from equation 1.7 that the fundamental precessional frequency of spins in a magnetic field is proportional to the applied static magnetic field B_0. Over this static field, if a linear gradient field G is superimposed, the frequency of precession becomes a function of space, as shown in the below equation (1.12). Hence as seen in the figure 1.3, the magnetization of spins precesses exactly at ω_0 (which is the Larmor frequency of precession for the applied B_0 field) only at a particular point (or a region) in space, whereas at other points, they are either greater than or less than the ω_0.

$$\omega = \gamma(B_0 + zG_z) \tag{1.12}$$

This is the fundamental idea behind spatial localization of spins. In MRI, the slice of human body which needs to be imaged, is selected based on the above idea, by using a gradient field, the amplitude of which (in the order of mT/m) is much less than the main static field (in the order of T). Along with the application of this slice selection gradient, when a RF pulse of a specific Bandwidth centered around ω_0 is applied, the magnetization of spins is tipped to the transverse plane, but only in the selected slice. Rest of the spins, having their frequency of precession away from ω_0 would have their

magnetization undisturbed.

While localization of MR signal along one direction can be achieved in the above way, the signal received would still represent the magnetization from the complete slice and not from any particular voxel. Hence the signal needs to be localized further along the rest of the dimensions, and this is done by techniques known as phase and frequency encoding. This involves application of gradient fields along the rest of the two dimensions, resulting in modification of the precession frequencies. For e.g. application of linear time-independent gradient fields along x and y axes would result in

$$\begin{aligned} \omega_x &= \gamma(B_0 + xG_x) \\ \omega_y &= \gamma(B_0 + yG_y) \end{aligned} \tag{1.13}$$

During imaging the gradient along the x-direction [2], referred as read encoding gradient is played out during the entire time of acquisition of the signal. The received signal would compose of frequency components which can then be directly correlated via an Inverse Fourier transform to the spatial distribution of spins along the x-direction. On the contrary, the gradient along the y direction, referred as the phase encoding gradient, is applied only for a short time before the actual acquisition. The application of this gradient causes the spins to acquire spatially dependent frequencies along the y direction and upon its removal (i.e. immediately after the gradient is switched off), the spins would have a spatially dependent phase. This modulation of phase remains for the frequency encoding period that follows it after which the phase encoding steps are repeated with a different gradient levels, so as to acquire the complete slice.

It is easier to comprehend the acquisition of MR signals in spatial frequency domain, which is also called as k-space, the concept of which is explained below.

The application of gradient fields results in a spatial distribution of precessional frequencies and hence the complex signal from the spin system, neglecting the effects of relaxation, can be written as

[2] In reality the direction of slice, phase and read encoding gradients can be either of the 3 axes.

$$
\begin{aligned}
S(t) &\propto \int_V \rho(\vec{r}) e^{i\int_0^t \omega(\vec{r},t')dt'} d^3\vec{r} \\
&\propto \int_V \rho(\vec{r}) e^{i\int_0^t (\omega_0+\gamma G(t')\vec{r})dt'} d^3\vec{r} \\
&\propto e^{i\omega_0 t} \int_V \rho(\vec{r}) e^{i\int_0^t \gamma G(t')\vec{r}dt'} d^3\vec{r}
\end{aligned} \tag{1.14}
$$

In the above equation, if $\gamma \int_0^t G(t')$ is considered simply as $\vec{k}$, the signal received can be written as

$$
S(k) \propto \int_V \rho(\vec{r}) e^{i\vec{k}\vec{r}} d^3\vec{r} \tag{1.15}
$$

which is nothing but the Fourier transform of the spin density $\rho(\vec{r})$. Hence the spin density can be obtained from the received complex signal as

$$
\rho(\vec{r}) = F^{-1}(S(k)) \tag{1.16}
$$

This important and critical realization by [6] opened the gates of NMR to the widely used Fourier imaging methods. While the terminology of $\vec{k}$ space has been used since then to denote the spatial frequency domain formed by the gradient fields in multiple directions, the term $\vec{k}$ trajectory put forward by [7] denotes the methodology used to traverse the spatial frequency space.

While the actual application of gradient fields along x and y directions as stated in equation 1.13 may vary based on the actual pulse sequence used, in the basic gradient and spin echoes, one of the gradients (either x or y) is applied after slice selection for a short duration causing the spins to acquire a spatially dependent phase upon removal of the same. The other gradient is applied during acquisition to cause spatially dependent frequencies which are sampled at fixed points in frequency space.

1.3 Introduction to RF coils and signal detection

The complete hardware of a MRI system consists of multiple varieties of coils to generate the following fields:

- A static magnetic field in the order[3] of 0.2 to 9.4 T, to effect the Larmor precession of the spins.
- Spatially varying gradient fields in the order of few mT/m to 70 mT/m, to localize the spins in terms of their frequency and phase.
- An RF field in the order of few μT to 30μT to tip the magnetization towards the transverse plane.

The Radio Frequency (RF) coils, being the focus of this research work, are introduced and explained in a elaborate way in the following sections.

1.3.1 Types and Classifications

The primary purpose of RF coils is twofold: 1) Transmission of RF Electromagnetic energy to tip the magnetization in the object and 2) Reception of the signal generated by the relaxing magnetization. Accordingly the coils can be classified as:

- Transmit coils - coils which are configured to generate the field in the imaging volume.
- Receive coils - coils which are configured only to receive the signal from the object.
- Transmit/Receive coils - coils which are configured for both the above said purposes.

While it is possible to configure the transmit coils to receive as well, dedicated Receive coils (or array of coils) are preferred for their ability to provide a better Signal to Noise Ratio of the acquired signal and accelerate acquisitions. It should be mentioned here that coils are seldom designed as transmit only coils, as the receive capability of the same transmit coils can be used for purposes like to correct RF field inhomogeneities.

[3]The values of the B_0 and gradient fields shown here are in the range of commonly used values.

Based on the target region of interest and on the way in which the currents are formed in the coils (or emf induced), they can be classified as:

- Volume coils - Coils which encompass a volume, mostly in a radially symmetric manner, wherein currents are formed to generate a uniform transmit field.
- Surface coils - Coils which are formed out of single antenna (usually in the form of a loop) or an array of loops, to receive signals from the object with enhanced sensitivity.

Volume coils like Birdcages or TEM resonators are used predominantly as transmit coils (though designed as T/R coils) due to their ability to produce highly uniform fields over a large region, whereas surface coil arrays are used as receivers, as mentioned above, for improved sensitivity and for their ability to be used in partially parallel acquisitions. Transmit coils made of an array of loops or an array of microstrip antennae are increasingly being used in higher field strengths ($\geq$7 T) as they offer a way to drive loops individually (unlike Birdcages) to minimize field inhomogeneity.

1.3.2 Reciprocity

In order to comprehend the characteristics of RF coils during the transmit and receive phase of the system, it is important to understand Reciprocity and its role in MR.

Reciprocity in Electromagnetism states that the relationship between an alternating current and the field produced at a point would be the same even if their spatial positions are swapped. Take the case of a single loop antenna shown in figure 1.4, where the circulating current I in the loop produces a magnetic field around it. The field produced by this loop at point 1, located physically close to the loop would be, in magnitude, greater than the field produced at point 2, farther away from the loop. In MR, as per principle of reciprocity, magnetization precessing at point 1 would induce a larger *emf* across the terminals AB of the loop, compared to the same magnetization at point 2.

In other words (as is known in Antenna theory), it can be stated that the transmit and receive properties of an antenna are similar. The same is true in the case of RF coils

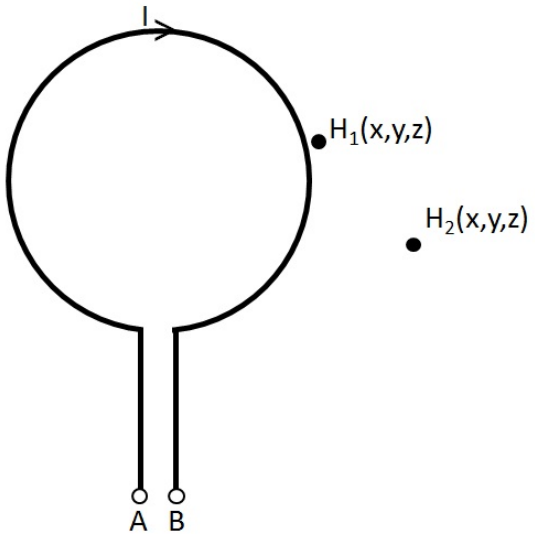

Figure 1.4: ***Reciprocity:*** *The magnitude of magnetic field produced by the loop antenna at point 1 denoted by H_1, would be greater than the magnitude of field produced at point 2 denoted by H_2. As per reciprocity, a precessing magnetization at point 1 would induce a larger emf across terminals AB than a magnetization at point 2.*

used in MRI, which are nothing but antennae used in their near-field regions.

1.3.3 Induced Signal

It is known from Faraday's law that a changing magnetic flux through a loop of wire generates an *emf* proportional to the rate of change of flux. If the flux is considered as the integral of flux density $\vec{B}$ over the area S covered by the loop, the *emf* can be represented by

$$emf = -\frac{d}{dt}\iint_S \vec{B} \cdot d\vec{S} \tag{1.17}$$

As shown in [8], using the vector potential of the field quantity $\vec{B}$ and Stoke's theorem, it can be proven that,

$$emf = -\frac{d}{dt}\iiint_{Volume} \vec{B_{rx}}(r) \cdot \vec{M_{xy}}(r,t) d^3r \tag{1.18}$$

where

$$\vec{B_{rx}} = \frac{\mu_0}{4\pi}\vec{\nabla} \times \oint \frac{d\vec{l}}{|\vec{r} - \vec{r_1}|} \tag{1.19}$$

The equation 1.18 shows mathematically how the signal induced in the loop is related to the fictitious field produced by the loop per unit current $\vec{B_{rx}}$. The fact that Reciprocity is being used here should be noticed. The term $\vec{B_{rx}}$ is known as the receive sensitivity of the loop.

It should also be noticed that the signal induced is related to the transmit as well as receive properties of the RF coil. While the Transverse Magnetization $\vec{M_{xy}}$ is caused due to the transmit field B_1^+, the term $\vec{B_{rx}}$ characterizes as to how sensitive the loop (or an MR RF coil) is to receive signal from the relaxing magnetization.

1.3.4 Induced Noise

RF coils, like all other electronics, are highly susceptible to noise. This is compounded by the fact that the signal received by the coils from the relaxing magnetization is low, compared to many other fields of EM reception. The root mean square of the Johnson-Nyquist noise voltage generated during signal reception in a MR RF coil can be given as

$$U_n = \sqrt{4k_bTR_t\Delta f} \tag{1.20}$$

where R_t refers to the total resistance seen by the RF coil and Δf indicates the bandwidth over which the signal is acquired. The terms k_b and T represent Boltzmann's constant and absolute temperature respectively. Losses in the coil and in the phantom contribute to the series resistance R_t in the coil as shown in figure 1.5.

These losses include:

- Loss due to the finite conductivity and skin depth of traces (usually Cu) used in the coil elements and the associated circuits.
- Loss due to electric and magnetic coupling between coil elements and surrounding cables / circuits.

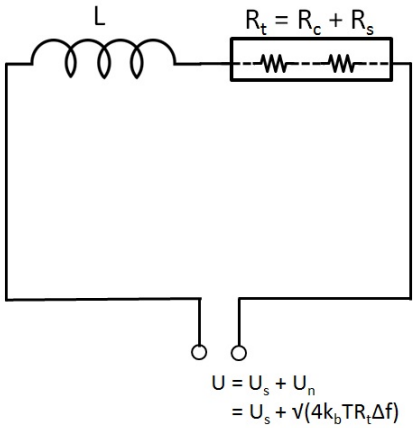

Figure 1.5: ***Noise equivalent circuit:*** *A loop antenna (or an element) receiving MR RF signal can be represented as an inductance in series with a resistance. The resistance in the Johnson-Nyquist equation given in equation 1.20 is the sum of the different resistances seen in the coil and in the conductive phantom / object.*

- Loss due to eddy and displacement currents induced in the conductive phantom by the magnetic and electric fields of the coil, respectively.
- Loss due to far field radiation of coils, away from the region of interest of the object.

During transmit, these losses can result in significant wastage of power due to reduction in transmit efficiency ($B_1^+/sqrt(W)$) and during reception, the losses manifest themselves as induced noise due to Reciprocity. While these losses can be significantly minimized by careful design of the coil elements (as would be shown in subsequent chapters), the loss due to currents generated by the changing magnetic field inside the sample cannot be avoided. The design of the coil element should ensure field patterns targeted over only the region of interest in order to avoid losses in other regions.

Chapter 2

RF coils - characterization and design

RF coils used in MRI scanners have evolved tremendously over the past two decades with designs to improve sensitivity, homogeneity and parallelization. Technologies from other fields have been or are being adapted with the primary focus being improved resolution and patient comfort. Alongside the development of coils, new tools and techniques for their characterization have emerged that enable an RF engineer to study, understand and develop coils to address specific issues. In this chapter, a few baseline parameters that characterize RF coils are introduced and their measurement techniques are briefed. This is then followed by block diagrams and equivalent circuits for certain major coil types, their associated circuits and bench characterization. Alongside the basics, things learned by the author during the course of the thesis work are also written.

2.1 Q factor

One of the most important indicators of an RF coil's quality, is a figure of merit, called Q factor. A measure of a resonator's damping, Q factor can be defined as the ratio of energy stored in the resonator and the energy lost per cycle. This can be expressed by

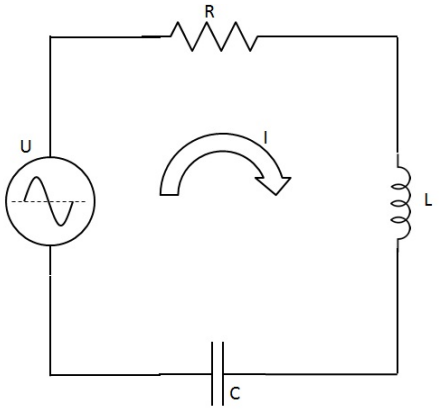

Figure 2.1: ***A series RLC circuit***

the following equation:

$$Q = 2\pi \frac{Energy\ stored}{Energy\ lost\ per\ cycle} \tag{2.1}$$

For a simple LC circuit shown in figure 2.1, it can be shown equivalent to

$$Q = \frac{1}{R}\sqrt{\frac{L}{C}} = \frac{\omega_0 L}{R} \tag{2.2}$$

and practically measured as

$$Q = \frac{\omega}{\Delta\omega} \tag{2.3}$$

where ω represents the frequency of resonance of the circuit and $\Delta\omega$ represents the 3 dB bandwidth around the frequency of resonance. As can be inferred, an increased resistance in the circuit (or in our case - RF coil) can increase the power dissipated per cycle and hence mean a decreased Q. A sample illustration of the response of circuit with higher resistances is shown in figure 2.2.

In the case of RF coils, as stated in the section on Induced Noise in the previous chapter, the total resistance in the setup is a sum of resistance due to the coil (R_c) and that due to the phantom / object (R_s). Hence the Q factors can be distinguished as loaded and unloaded, as shown in the following equations depending on whether the coil

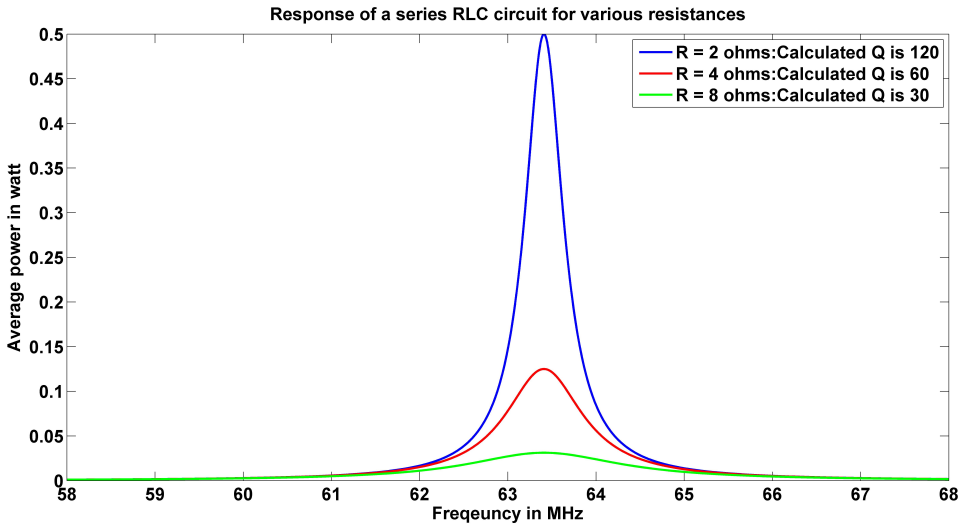

Figure 2.2: ***Q factor and damping:*** *The Q calculated from the resonant frequency for the simple RLC circuit shown in figure 2.1, for different series resistances, with a source of 1 V, an inductance of 600 nH and a capacitance of 10.5 pF. As can be seen there is an increased dampening for circuits with increased resistances*

is loaded with the conductive phantom or not.

$$\begin{aligned} Q_{un} &= \frac{\omega_0 L}{R_c} \\ Q_l &= \frac{\omega_0 L}{(R_c + R_s)} \end{aligned} \tag{2.4}$$

It is to be mentioned that for RF coils used in MRI scanners, it is good to have the loaded Quality factor that is much less than the unloaded quality factor, so that the fields from the coils are sensitive to the object that is to be imaged. In this regard, a measure of sensitivity would be the ratio between the loaded and unloaded Q factors shown below.

$$\frac{Q_{un}}{Q_l} = \frac{R_c + R_s}{R_c} \tag{2.5}$$

As shown in [9], the ratio can be related to the ideal sensitivity that can be obtained from a coil as

$$S = S_0 \sqrt{(1 - \frac{Q_l}{Q_{un}})} \tag{2.6}$$

The Q ratio needs to be high so that the noise from the sample dominates and that the relative noise contribution from the coil is less. A rule of thumb in this aspect would be

the following:

$$\frac{Q_{un}}{Q_l} >= 5 \tag{2.7}$$

2.2 Signal to Noise Ratio (SNR)

The Signal to Noise Ratio of an RF coil, commonly defined as the ratio between the induced voltage and the voltage generated by the noise, is the most important quantity to characterize the performance of an RF coil.

The induced emf and the noise voltage have been shown as per equations 1.18 and 1.20 in the previous chapter. The SNR of a coil can be expressed from them as

$$SNR = \frac{-\frac{d}{dt}\iiint_{Volume} \vec{B_{rx}}(r).\vec{M_{xy}}(r,t)d^3r}{\sqrt{4k_bTR_t\Delta f}} \tag{2.8}$$

SNR measured in the above way, as can be seen from the equation, is a quantity relevant more for the experiment, than for the RF coil. If one has to separate the terms relevant for coil alone, then SNR in the above equation is proportional to $\frac{B_1}{\sqrt{P.T}}$ where P characterizes the total power lost in the object. While this equation characterizes the instantaneous SNR, a more practically relevant way is to measure the SNR in the obtained image. As far as coils are concerned, the quantity measured this way is a relative term, used often to compare different coils or configurations.

While there are multiple ways of SNR measurement in images ([10], [11], [12], [13], [14], [15], [16],), the 'gold standard' way to measure the same is to obtain a series of images, using the same setup and protocols and calculate SNR as

$$SNR = \frac{Mean\ of\ the\ signal\ through\ the\ stack\ of\ images}{Standard\ Deviation\ of\ the\ signal\ through\ the\ stack} \tag{2.9}$$

This, known as **Multiple Acquisitions method** would give a pixel by pixel SNR for the obtained images. The assumption here is that the signal from the coil stays the same whereas the noise varies with a Gaussian distribution for different images. A high number of samples is required to minimize the error in the calculated SNR, as the error

is inversely proportional to the root of number of samples in a Gaussian distribution.

Though obtaining SNR this way is simple and straight forward for a coil setup with a phantom, it is practically difficult to subject a patient through the whole lot of iterations. A way to mimic the iterations over time was presented in [14] in which only one normal image is obtained along with a noise image. Replicas of iterations are then acquired by random reordering of the acquired noise image and adding the same with the acquired image, generating replicas of normal image. SNR is then calculated using this stack of replicas. Different coil configurations presented in this work use this method for SNR comparison.

2.3 Single element coil

A single element RF coil, generally contains one circular loop or rectangular element[1] along with associated electronics, generating the B_1^+ field required (if used for transmission) or receiving the induced emf and feeding the received signal onto the further receive chain of the MR scanner (if used for reception). Though single element coils are hardly used nowadays in actual clinical imaging, due to the advancement of multi-channel coil arrays of various types, it is briefed here as they are the building blocks of the coil arrays presented in this thesis work.

Figure 2.3 shows the block diagram of a single element Transmit/Receive and a Receive only coil. While the inductance that creates the B_1 field (be it the $B_1{}^+$ for transmission or the imaginary $B_1{}^-$ for reception) is formed by the dimension of the loop, fixed capacitors are used to tune the loop to the frequency of interest. A matching network is used to transform the impedance given by the loop to the characteristic impedance of the system (which is usually 50 Ω) and a balun (cable trap) suppresses the common mode currents on the outside of the coax line. The MR signal is then amplified with a minimum Noise Figure by a Low Noise Amplifier and then passed on to the Receive chain of the MR system. In the case of a Transmit/Receive coil, a T/R switch is used to

[1] Other antenna types like Microstrip lines, Dipoles etc. are also being increasingly explored especially at high frequencies.

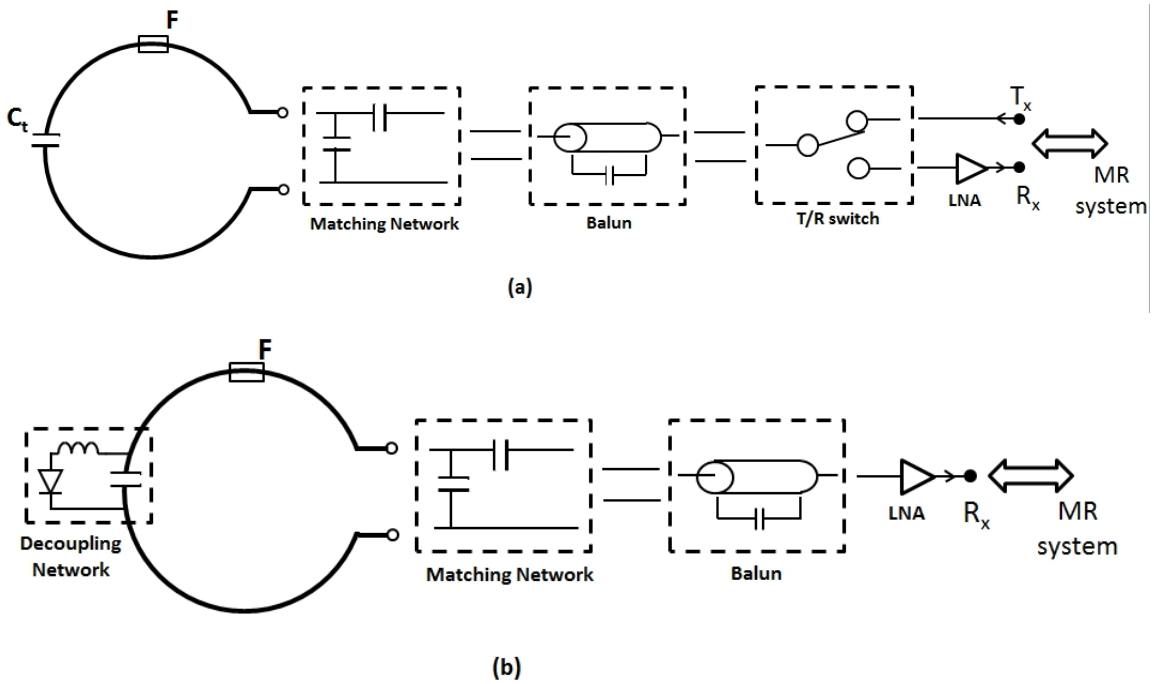

Figure 2.3: ***Single element coil:*** *The top portion shows the circuits connecting a single element Transmit/Receive coil to the MR system and the bottom portion shows the circuits for a single element Receive only coil.*

isolate the sensitive components in the Receive chain during the 'transmit' phase of the scan, when high power is fed into the coil to generate the magnetic field. Coils designed only for Reception will make use of a transmit coil (typically the Body Coil found within MR systems) and hence they need to be decoupled during the transmit phase using a decoupling network.

The circuits / networks mentioned in the above paragraph are explained in detail in the coming sub-sections.

2.3.1 Tune of RF coil elements

The tune of elements in RF coils is achieved using more than one capacitor, depending on the dimension of the element. This has the following advantages:

- Higher Q of the element, due to low radiation: As the circumference of the element increases and approaches quarter wavelength, the loop starts to radiate, decreasing the unloaded Q of the elements. This can decrease the efficiency of the loop - $\frac{B_1^+}{\sqrt{W}}$

- during transmission and the SNR of the loop during reception. However this can be minimized by distributing capacitors across the element, bringing down the RF potential difference between any two points in the loop.

- Distribution of electric fields: E fields of a loop are concentrated around the capacitances used in the loop. In the case of a loop tuned with only one capacitor, the E field concentration around this capacitor tends to be high, whereas in the case of a loop tuned with multiple capacitors, E fields of lesser magnitudes are distributed around the loop due to higher values of capacitances used. This minimizes the electric field coupling to the phantom and hence decreases the losses due to the displacement currents created by the E fields. As an example, EM field simulation results of two simple loops of dimensions 5 x 5 cm^2, tuned with one and three capacitors each, are shown in figure 2.4, energized by a power source. E field distributions on a surface 0.5 mm below the loops show that their magnitudes are higher for the loop tuned with one capacitor. Integration of magnitude of E fields over the surface also reveals the same. The radiated power observed at a boundary of 30 x 30 x 30 cm^3 shows a higher value for the loop with one capacitor, compared to the loop tuned with two capacitors.

- Stray capacitances developed in the MR environment ([17]) have a larger effect on the loop tuned with lesser number of capacitors, due to the shorter values of capacitors used.

The above advantages of capacitor distribution are more relevant for coils with a high ratio of coil size to wavelength, whereas during design of coil elements with low ratios, one needs to wary of any increase in coil loss due to addition of capacitors.

2.3.2 Impedance matching of an RF coil

Impedance matching of the loop is done for two purposes. The first is to keep the reflections in a transmit coil low so that the majority of incident power is accepted by the coil. The second is to make sure that the Noise Figure of the preamplifier is under control

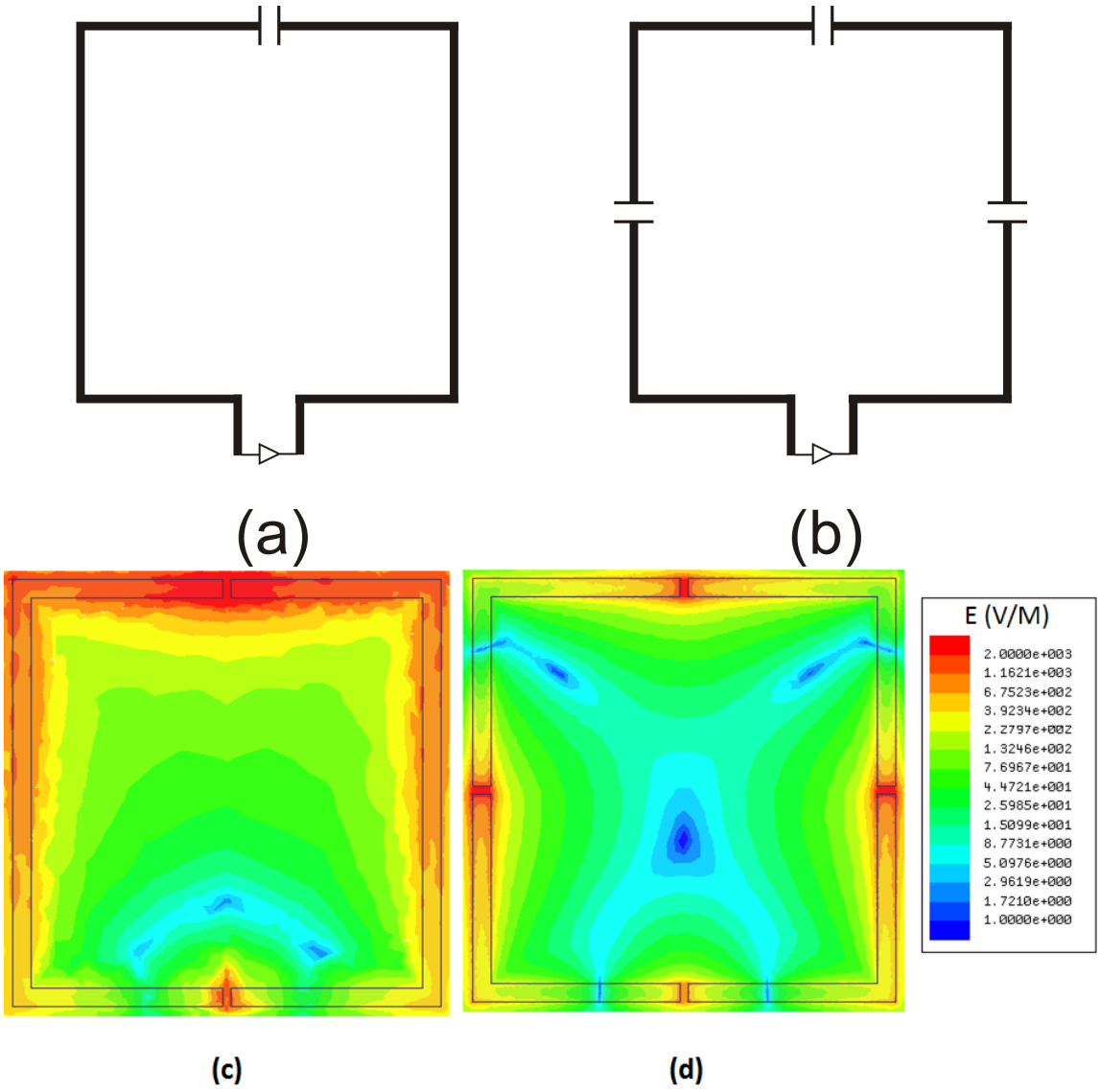

Figure 2.4: ***Capacitor distribution and E fields*** - *E field distributions (for a total input of 1 W) obtained by EM simulations, for loops tuned with different number of capacitors. The loop in figure a has been tuned to 300 MHz with just one capacitor, whereas the loop in figure b has been tuned to the same frequency with 3 distributed capacitors. It is clear from the distribution that the E fields for the loop tuned with one capacitor, shown in figure c, is higher than the one tuned with 3 capacitors, shown in figure d. Sum of the absolute magnitude of the E fields over the surface gives a value of 53.6 V/m for the single-cap loop and 32.5 V/m for the 3-cap loop. The electric flux obtained by integrating the dot product of the E field vector and the surface normal, over the surface gives a value of 27.79 Vm for the single cap loop and 17.09 Vm for the 3 cap loop. The complex magnitude of H field produced at the center of the loop tuned with one cap is 3.94 A/m (for a delivered power of 1 W into the coil) whereas for the loop tuned with 3 caps, its 5.3 A/m, showing that the transmit efficiency increases with better distribution of capacitors.*

(preferably < 0.5 dB) during reception. Usually the Preamplifiers are noise matched to a particular range of impedances, around 50 Ω (characteristic impedance of the system) and hence the loops need to be matched to 50 Ω as well. Matching can be achieved by shunt or series capacitors, inductors, impedance transformers or even a section of coaxial cable. It needs to be made sure that the network in itself doesn't add any resistive component to the circuit as a whole.

2.3.3 Baluns in RF coils

Baluns, as said before, act as a common mode suppressor preventing currents on the outer part of the coaxial cable. While connecting the unbalanced system side and the balanced coil side, Baluns also ensure minimum coupling between closely spaced parallel coaxial cables. Being a part of the circuit through which the RF signal traverses, it is essential to make baluns with a 50 Ω characteristic impedance. There are multiple ways in which Baluns can be realized [18] and all of them provide a high impedance in the 'ground' of the transmission line, isolating the system side ground and the coil side virtual ground, while maintaining the characteristic impedance for the signal to pass through. Baluns used in the RF coils presented in this work, make use of coaxial cables wound in the form of solenoid or a toroid, that provides the inductance in the ground line. This is then tuned with a capacitor in shunt, as shown in figure 2.5 to the frequency of interest. The Bazooka balun shown in the figure is also used commonly in MR RF coils.

It needs to be mentioned that the ground line in a balun, being a high impedance tank with a large Q, is susceptible to increased temperatures during long scans. Hence the impedance provided by the balun needs to be carefully optimized by adjusting the inductance and/or the frequency of tune, to decrease the circulating currents. Placement of the baluns and the separation between them needs to be optimized as well. The value of tune capacitance used in the balun should be large (typically > 10 pF) so as to minimize the large Electric field build up that can heat up the balun and damage the capacitor. Having more tune capacitors in series helps in this aspect. But the value of capacitor should not be so large to decrease the impedance obtained in the tank circuit formed.

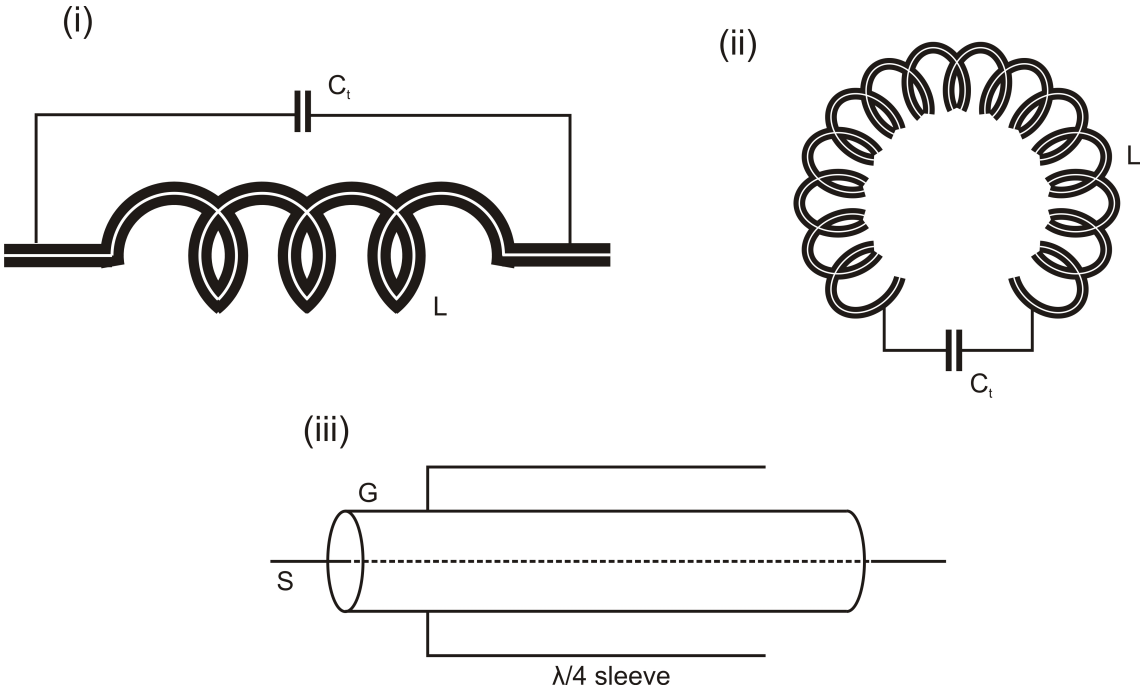

Figure 2.5: ***Baluns in RF coils:*** *In the solenoidal and toroidal baluns shown in 'i' and 'ii' respectively, the inductance is formed by the coaxial cable wound around a core, and then tuned with a shunt capacitor. This creates a high impedance in the outer part of the outer conductor, minimizing the common mode currents. In the balun shown in 'iii', called as "Bazooka" balun, a $\lambda/4$ line is attached as a sleeve to the outer conductor of the coax cable, effectively cancelling the shield currents by offering a high impedance.*

Care should also be taken during the construction of the balun to physically separate the two grounds that are isolated, as there would be a large potential difference between them, especially in a transmit coil.

For long cables in the receive chain, it is essential to include multiple baluns seperated by appropriate distances. A rule of thumb here can be a $\lambda/10$ distance between two baluns. Location of a balun in a RF coil cable also plays a role in reducing cable waves. At times, a balun wouldn't seem to decrease common mode currents, even though its finely tuned and seem to offer high impedance. This is due to the reason that its location in the cable is close to a voltage node. Presence of baluns near voltage node has no effect on the shield currents, as the high voltage points (i.e. antinodes) are not suppressed. In this case, moving the balun either side, can make a significant difference to the standing waves. It should also be ensured that the baluns do not couple with the surrounding circuits themselves and that they are isolated. If found to couple, having a shield around the same, connected to the system side (i.e. unbalanced side) ground reduces the same.

2.3.4 Decoupling

Coils designed only for reception should be detuned during the transmit phase of the scan for the following reasons:

- Coupling between the resonant transmit coil and the receive coil can shift the frequency of the transmit coil (depending upon the size of the receive loop) due to mutual inductance, thereby increasing the reflection of the RF power on the transmit chain. While the transmit chains in the existing scanners are made to handle the reflected power, this can result in higher power requirements from the RF amplifier.

- The transmit coil can induce very strong currents in a resonant receive loop, which can be harmful to the components in the coil as well as to the patient, as the currents tend to heat up the surface temperature of the coils.

- Currents induced in a receive coil can produce fields of their own, opposing the original transmit field, thus creating inhomogeneous regions of magnetization flip angle within the patient or phantom, resulting in inhomogeneous images. The currents induced can also cause B_1^+ hotspots resulting in an inadvertent increase of Local SAR.

Transmit coils are also detuned during reception to minimize coupling to the receive elements, as the mutual inductance can result in a receive element's impedance getting changed and hence affecting the SNR.

The decoupling in a receive element is normally achieved in a coil using a resonant network consisting of an inductor placed in parallel to one of the tune capacitors, and the network tuned to the frequency of operation of the scanner. A diode placed in the network can be switched based on the decoupling needs of the coil. At resonance, the network offers a high impedance across the tune capacitor, suppressing the induced currents in the coil. The circuit can be designed to have the diode actively switched, or anti-parallel diodes can be used to make passive decoupling networks. Usage of a single diode in series in a receive element can also decouple the same, but is not advisable due to the finite resistance of the diode decreasing the Q of the element. Nevertheless diodes can be used in series in transmit coils to achieve decoupling during reception.

In receive coils having large elements or in large transmit coils, one decoupling network may not be enough to sufficiently decouple the coil and hence more than one network per element might be used. RF currents through an actively biased diode can raise its temperature and hence care should be taken to ensure that the diode and the inductor can handle them. It should also be ensured that the temperatures reached by the components do not raise the surface temperature of the coil. Distortion of B_0 field by the circulating DC current can cause artefacts in the image. Care should be taken to ensure minimum distortion by decreasing the area of the loop formed by the DC currents and by having traces that carry the opposing DC currents close to each other. Orientation of the decoupling inductor perpendicular to the B_1^+ (transmit) field would help to decrease any current directly induced on the decoupling inductor thereby distorting the field locally.

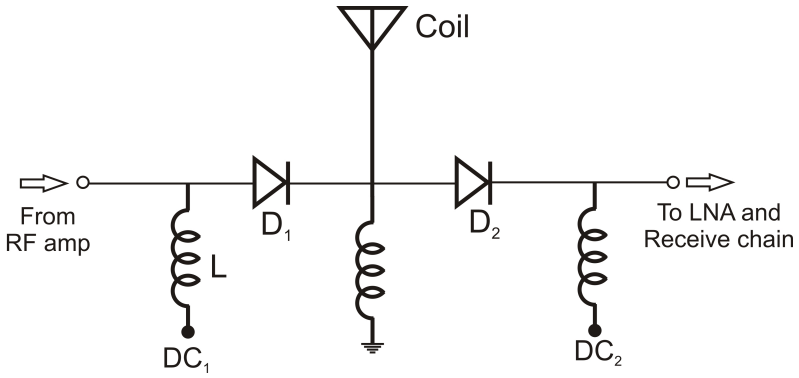

Figure 2.6: ***A simple T/R switch:*** *During transmit, the diode D1 is forward biased whereas D2 is reverse biased, by appropriate DC voltages or currents through the DC lines DC1 and DC2. Hence the power from the RF amplifier is sent towards the coil. During reception, the diode D2 is forward biased and D1 reverse biased. While the above T/R switch would work in principle, usage of diodes in series in a receive line is not advisable as it can switched by the high voltage during the transmit phase and the finite resistnace can add to the noise during reception.*

2.3.5 Transmit/Receive switch

Coils that are designed to have transmit as well as receive capability, would need a Transmit/Receive (T/R) switch in their circuit chain. This is to direct the RF power from the Power Amplifier towards the coil during transmission and isolate the sensitive Low Noise Amplifiers in the receive chain.

This can be realized using appropriate diodes and pi networks. A simple T/R switch is shown in figure 2.6. Use of diodes in the receive chain can add to the resistance and hence additional noise. This can be avoided by having $\lambda/4$ pi networks with shunt diodes.

2.3.6 Preamplifiers

The purpose of a preamplifier at the start of a receive chain is to amplify the extremely weak signal (typically of the order of nV) provided by the RF coil for further processing. Designed as a Low Noise Amplifier (LNA), the preamplifier should add as low a noise as possible in the process of amplification. Noise figure and gain are two crucial parameters that characterize LNAs. Keeping in mind Frii's formula for the noise figure of a cascaded receive chain (Equation 2.10) where F and G refer to the noise factor and gain of a particular stage of the chain respectively - it is essential to have a minimum Noise Figure

and an appropriate gain from the LNA, so as to not increase the overall noise figure of the chain, which would have a direct impact on the SNR of the reconstructed image.

$$F_{total} = F_1 + \frac{F_2 - 1}{G_1} + \frac{F_3 - 1}{G_1 G_2} + ... \frac{F_n - 1}{G_1 G_2 ... G_{n-1}} \tag{2.10}$$

Apart from noise figure and gain, it is also required to have the stability of the preamp under control, with its Rollet's stability factor K $>$ 1. Input Impedance and Reverse Isolation are other crucial parameters that determine the overall coil's performance and stability as would be shown in coming sections.

2.3.7 Field distribution

Design of a loop for a particular application of MRI requires a knowledge of its field distributions. This enables one to choose the right dimension of the element, to image an object at a particular depth. While the complete list of factors to be taken into account for a coil design is explained in the next chapter, effect of dimension of the loop on its sensitivity has been shown by plots of the axial field distributions of few loops of different dimensions.

The axial B field data obtained by full wave EM simulations of loops of dimensions 10, 15, and 20 cms diameters at 128 MHz are shown in figure 2.7 and the field distribution is shown in figure 2.8.

Measured axial SNR plots of loops of different diameters, at 64 MHz, show similar variations.

The following points can be noted from the shown plot:

- Loops of smaller diameter have a higher B_1^+ field closer to the loops compared to loops of higher diameter. Hence as per reciprocity, smaller loops are more sensitive to the spins close to the loop and hence exhibit a higher SNR at a shorter depth.

- Loops of larger diameter on the other hand tend to have higher SNR at larger depths compared to small loops.

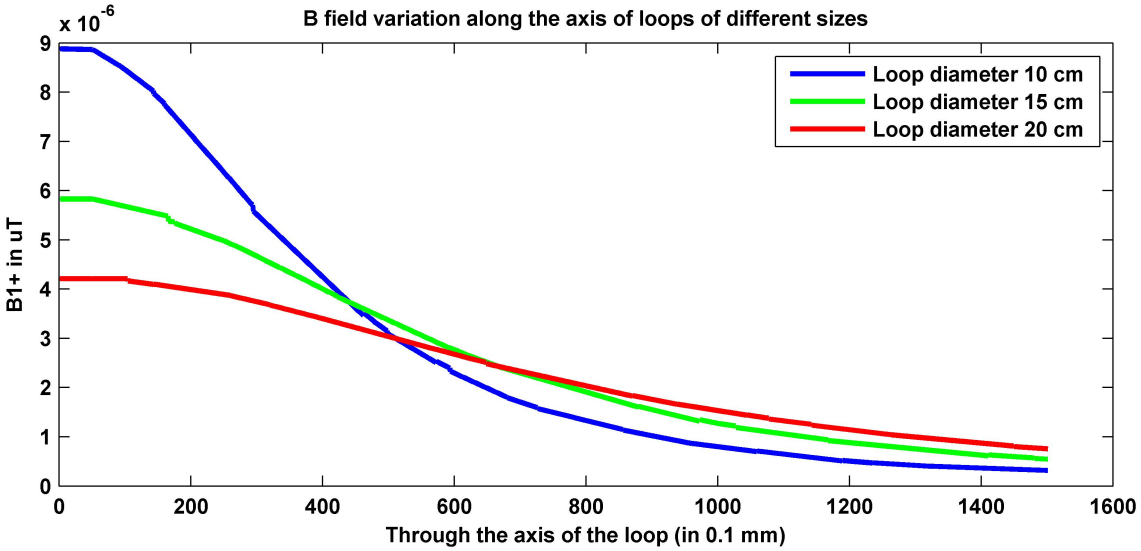

Figure 2.7: B_1^+ ***field for loops of diameters 10, 15 and 20 cm, excited by a series current source (1 A):*** *Among these loops, for a depth of upto 4.5 cm, one can choose the 10 cm diameter loop, for depths upto 6.5 cm the 15 cm diameter loop and for even larger depths, the 20 cm diameter loop.*

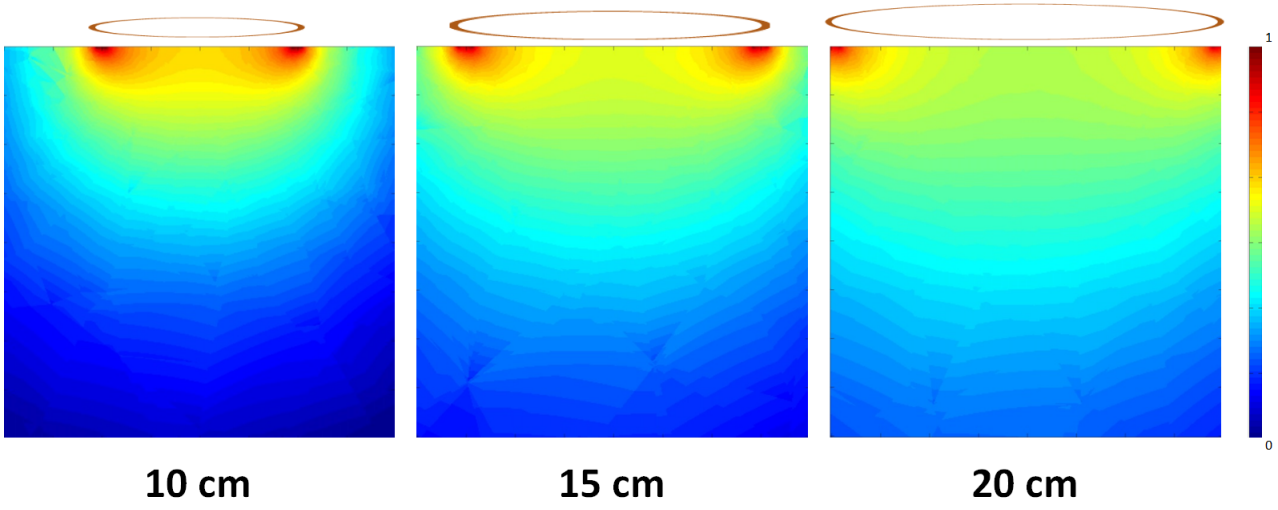

Figure 2.8: B_1^+ ***field distributions for loops of diameters 10, 15 and 20 cm, excited by a series current source (1 A):*** *The normalized distributions that characterize the sensitivity of loops show that while smaller loops have higher sensitivity at lower depths, larger loops have higher sensitivity at higher depths.*

- The simulations and experiments done show that, to get the highest SNR at depth 'd', the loop diameter should be 2d.

Though single element coils can be designed to provide an optimum SNR at a particular depth, it has its limitations in terms of coverage and acquisition time. Receive coil arrays were introduced to mainly overcome the above obstacles.

2.4 Phased array coils

Phased array coils are in principle a combination of multiple single element coils, geometrically located over the region of interest to provide higher SNR, coverage and spatial signal encoding. Presented by Roemer in his seminal paper [10], phased arrays were initially adapted from defence and telecommunications industries. Advancements in hardware and reconstruction over the years have made them the de-facto standard receive coils for MR clinical imaging. Further innovations in the design of arrays, associated electronics, patient comfort and new applications are being explored by research scientists.

A simple block diagram of a multichannel array is shown in figure 2.9. Comparing this with figure 2.3, one can readily notice that every element of a receive coil array would have all the electronics of a single channel receive coil. Dimension of the loops and their placement can be tailor-made as per the geometry of the region of interest. However resonant structures, when placed close to each other, detune themselves and no longer resonate at the frequency in which they were tuned, due to the mutual inductance between them. A simple example of the responses of two loops placed at a close distance is shown in figure 2.10. Apart from the shift in frequency, noise coupling between the loops can negate the SNR gained in a coil array, unless specific reconstruction techniques are used ([10]).

This necessitates decoupling different elements of a phased array. A few techniques to decouple neighbouring elements are shown in figure 2.11. The loops can be overlapped to neutralise the mutual inductance between them, as the 2nd loop has a portion of its area on either side of the 1st loop's current carrying element. So if there is a current

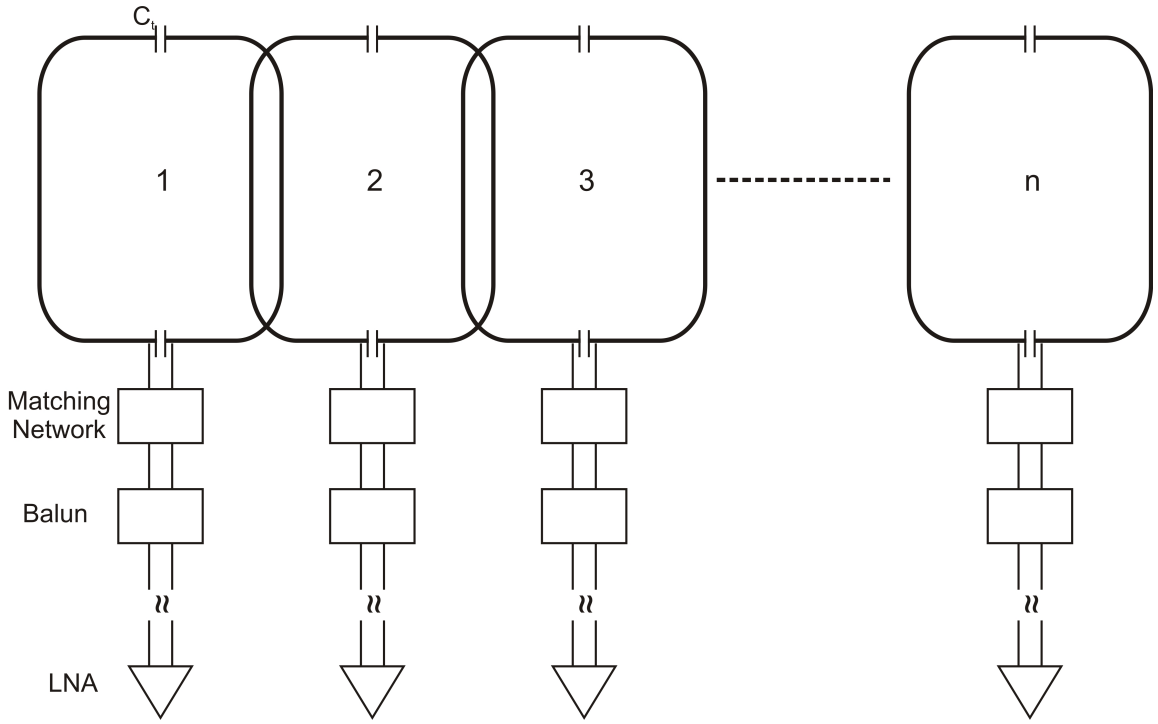

Figure 2.9: ***Block diagram of a linear receive coil array:*** *Multiple Loops of different shapes can be can be arranged over the region of interest to obtain the desired SNR and acceleration over the ROI. Loops are connected to low input impedance preamplifiers to decouple them from each other during reception. The length of the transmission line between the matching network and low input impedance preamplifier is altered to effect the preamplifier decoupling.*

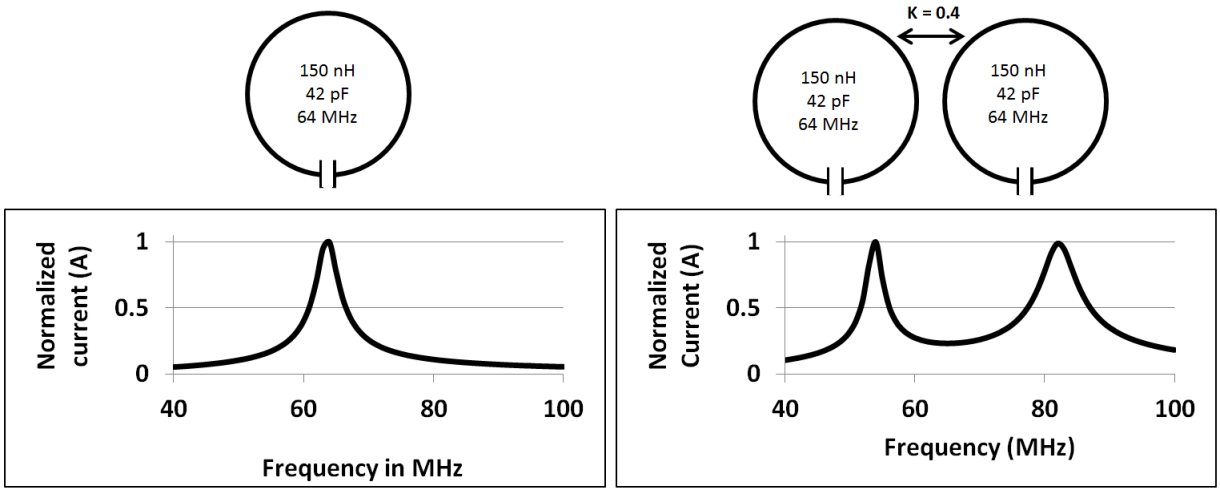

Figure 2.10: ***Resonance split:*** *Two loops having similar resonant frequencies couple strongly with their current response getting split as shown. This is due to the presence of a mutual inductance between the loops in addition to their own inductances. The inductance, capacitance and coupling coefficient values used to obtain the plots are also shown above.*

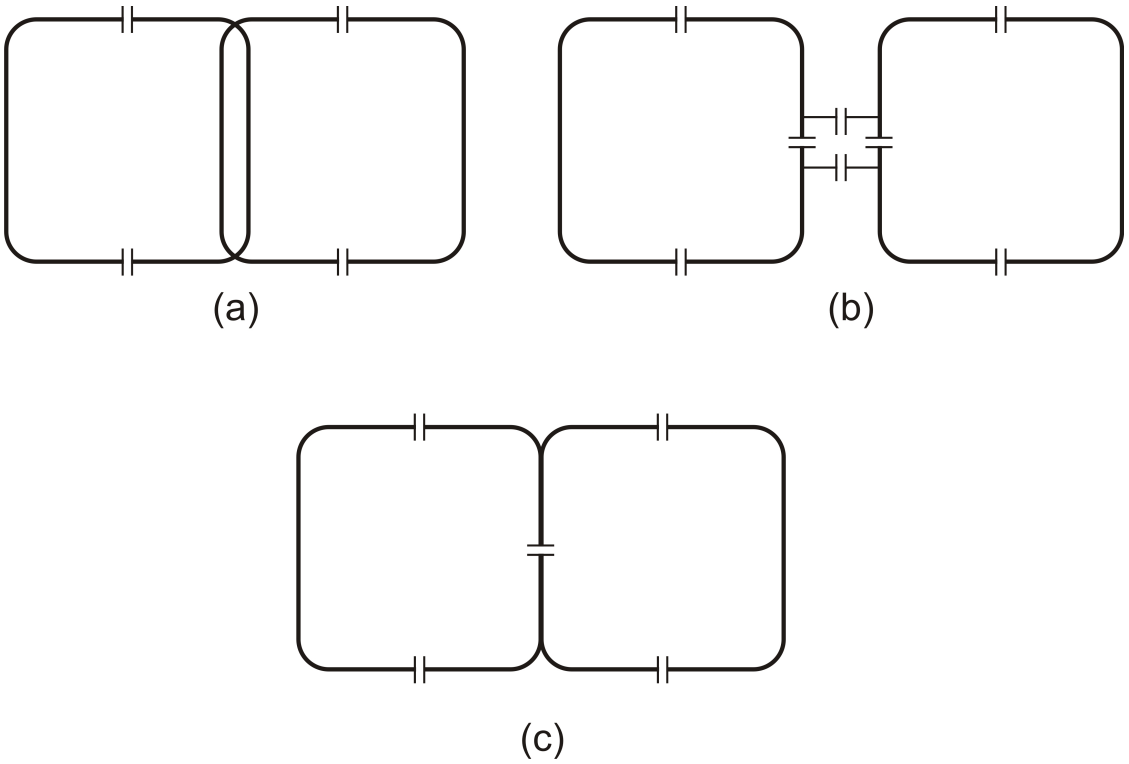

Figure 2.11: ***Decoupling techniques used in phased array coils:*** *Part 'a' shows inductive decoupling achieved by overlapping two adjacent loops, whereas in parts 'b' and 'c', the loops are capacitively decoupled. Overlap decoupling is the most preferred, as capacitive decoupling would involve multiple 'back and forth' changes in capacitor values to achieve a good decoupling*

flow in the 1st loop, opposing magnetic flux linkages in the 2nd loop minimizes the total induced emf. At the critical overlap, the mutual inductance is zero and hence the loops resonate at their own frequencies.

Neighbouring elements can also be decoupled using capacitors to cancel out the mutual inductance between them as shown in parts 'b' and 'c' of figure 2.11.

While neighbouring elements can be decoupled in the above said ways, there is still a strong mutual inductance between elements which are not adjacent to each other. This mutual inductance between non adjacent elements too results in frequency shifts, noise coupling and hence degradation in SNR and homogeneity.

A commonly used technique to decrease the mutual inductance between the loops is called preamplifier decoupling where all the receive elements in a phased array are connected to low input impedance preamplifiers, as shown in figure 2.12. The technique can be understood by keeping in mind the following things:

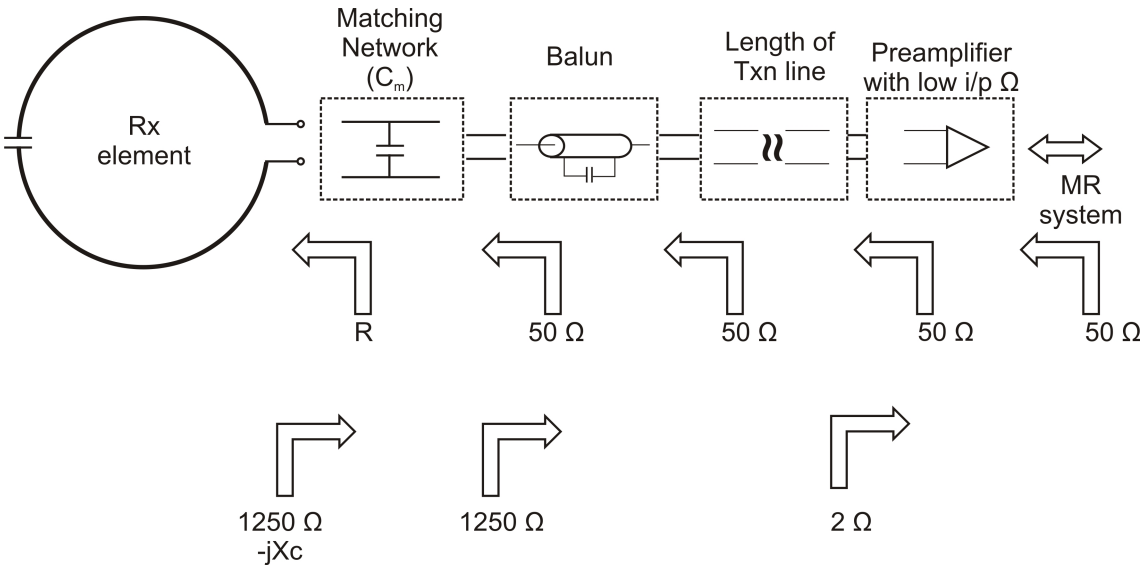

Figure 2.12: ***Preamplifer decoupling - Impedance transformation in preamplifier decoupling along with the nominal values:*** *Preamplifiers used in MR coils usually have an input impedance in the range of 2 Ω, which gets transformed into 1250 Ω at the matching network. The loop in turn sees this impedance along with the reactance from the matching network.*

- The preamplifiers are designed with a LC circuit at the input which in turn is connected to a voltage controlled device such as a FET. Hence the preamplifiers are sensitive only to voltage, which in our case is the induced emf.

- Coupling between elements is caused by the flux linkage from one element to the other. The magnetic flux in turn, is caused by the flow of current in elements

Hence if the flow of the current in a loop is minimized, it's coupling to the surrounding loops is minimized as well. In phased arrays, this is done by using the transmission line in between the matching network and the preamplifier. The length of the transmission line (along with the balun) is adjusted to be an odd multiple of $\lambda/4$. This transforms the low input impedance of the preamplifier (obtained by the LC circuit in front of the FET stage) to a high impedance across the matching network. This high impedance in turn manifests itself across the terminals of the loop, modified by a small extent by the matching network reactance. During reception of the signal from the object, due to the presence of this high impedance, the induced emf doesn't transform itself into a flow of current. As there is no flow of current, the loop doesn't couple with other elements, while

the induced emf is faithfully amplified by the voltage controlled FET in the first stage of the preamp.

On one direction, there is an impedance transformation as seen by the loop, but the preamp, on the other side, still sees the impedance from the matching network, as both the balun and the transmission line are designed to have the same characteristic impedance which is equal to the matched impedance (usually 50 Ω).

The transmission line between the balun and the preamplifier can be adjusted either by having a physical length of a line (say coaxial cable) or a phase shifter having the same characteristic impedance. This phase shifter would then produce the phase shift to effect the impedance transformation, along with the balun.

The described phased arrays have been constructed for a wide variety of applications and for various geometries. With one of the main purposes of this thesis work being construction of phased array designs for dynamic imaging of knee, design aspects and other considerations are explained in detail in the next chapter.

2.5 Birdcage coils

Birdcage coils represent an elegant solution to achieve a highly uniform field over a large volume. Introduced by Hayes et.al.([19]), the coils can be configured to produce a homogeneous rotating magnetic field in the axial plane within its volume, at the frequency of operation of the MR scanner.

The construction of a birdcage coil consists of two circular end rings connected by straight parallel segments (rungs) as shown in figure 2.13. The coils can be designed with tune capacitors located in the end ring segments (high pass birdcage) or on the rungs (low pass birdcage)[2] . Resonant frequencies of the ladder equivalent circuit for a high pass birdcage can be obtained by solving Kirchoff's voltage law as ([20])

$$\omega_m = \frac{1}{\sqrt{C(L + 2Msin^2\frac{\pi m}{N})}} \tag{2.11}$$

[2]Birdcages can also be designed with capacitors in both end rings and rungs (band pass configuration). This configuration is useful for large coils at high frequencies to minimize radiation effects [9].

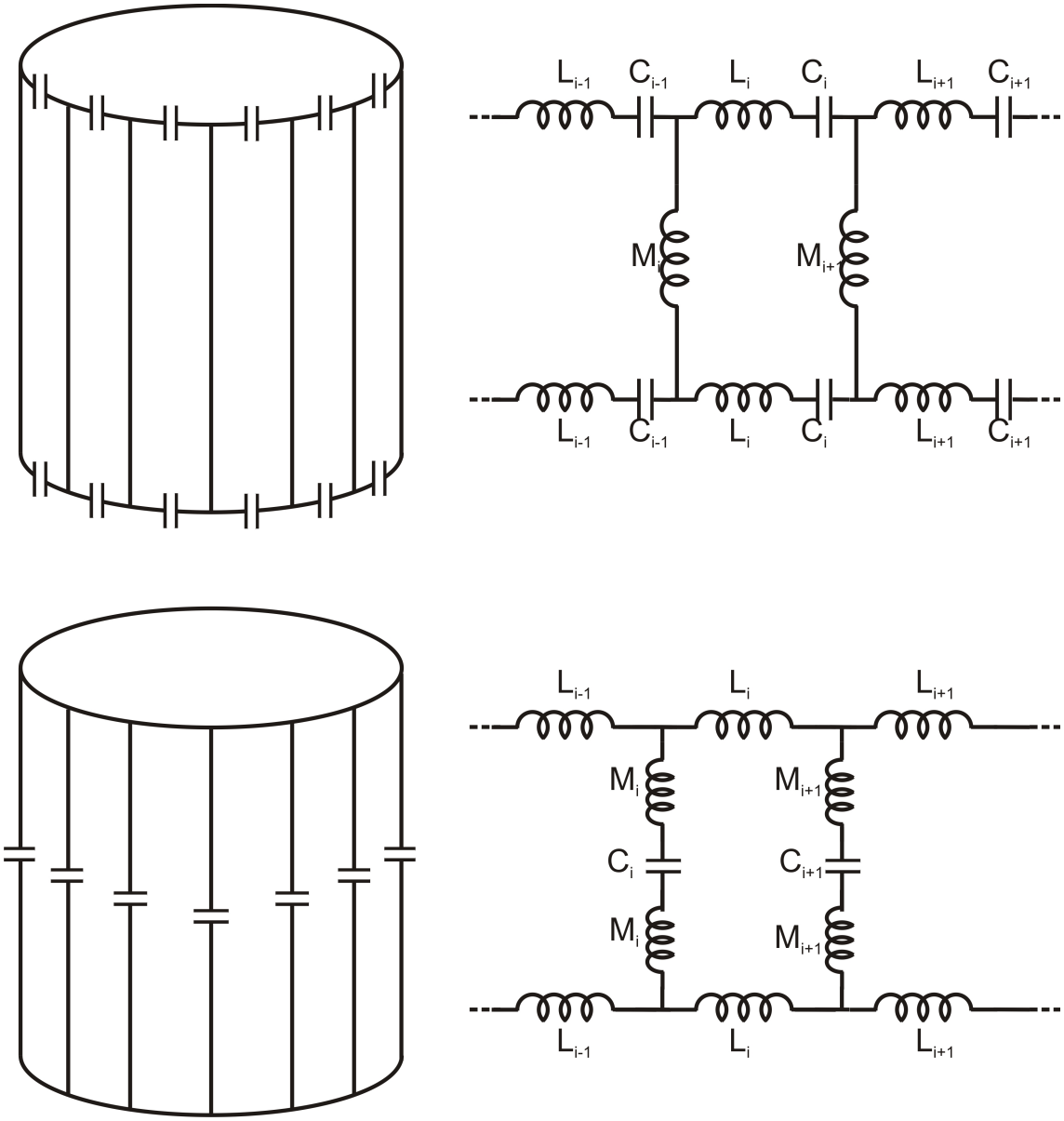

Figure 2.13: ***Birdcage coils and their equivalent network:*** *The top figures show a high pass configuration of the coil, with the tune capacitors on the end rings, whereas the bottom figures show a low pass configuration where the coil is tuned with the capacitors located on the rungs. As shown, the rungs are connected on both ends using circular end rings.*

where C corresponds to the effective capacitance of one end ring segment, M the effective self inductance of one rung and N the number of rungs. 'm' is an integer varying from 0 to N/2 and hence a birdcage of N rungs would have N/2 + 1 resonant modes[3]. The mode obtained by having $m = 0$ would then have a constant current in the end rings. Having the highest resonance frequency in a high pass birdcage, this mode is called the end ring mode. The mode obtained by having m = 1 has a sinusoidal current distribution around the rung corresponding to one sine wave.

When a birdcage is driven with two ports where the inputs have a constant amplitude but 90 deg. phase difference (quadrature drive), the sinusoidal current distribution then rotates as the phase varies in the two ports. The variation of currents in the birdcage and the resultant rotating field is shown in figure 2.14.

The absolute magnitude of the complex B_1^+ field shown over the central axial and sagittal planes in figure 2.15 give an idea about the uniformity of magnetic field produced by the birdcage. Except near the current carrying conductors, the field is fairly constant throughout the volume of the coil.

The choice between having a low pass design or a high pass design depends primarily on the Larmor frequency and whether there is another coil built along with it. High pass birdcages are generally preferred at high frequencies due to the fact that the tune capacitors are present in the end rings thereby reducing stray E-field coupling to the sample and minimizing the gradient induced eddy currents.

It is necessary to have an optimized shield as part of the birdcage, especially for high frequency coils (> 100 MHz), to minimize radiation and interaction with the surroundings. Care should be taken in the shield design to reduce gradient induced eddy currents that can distort the gradient waveforms thereby inducing artifacts in images.

The B_1 Field distribution, however uniform as said before, depends a lot on the symmetry of the structure and the load that is placed within. Non uniform distribution of capacitors and non uniform geometry of the rungs or the shield can have a detrimental

[3]This particular solution is an approximation and does not take into account the mutual inductance between the rungs. Solutions with the mutual inductance can be referred in [20]. Though usually M refers to the mutual inductance, in this approximation, with the mutual inductance neglected, it refers to the self inductance of the rungs.

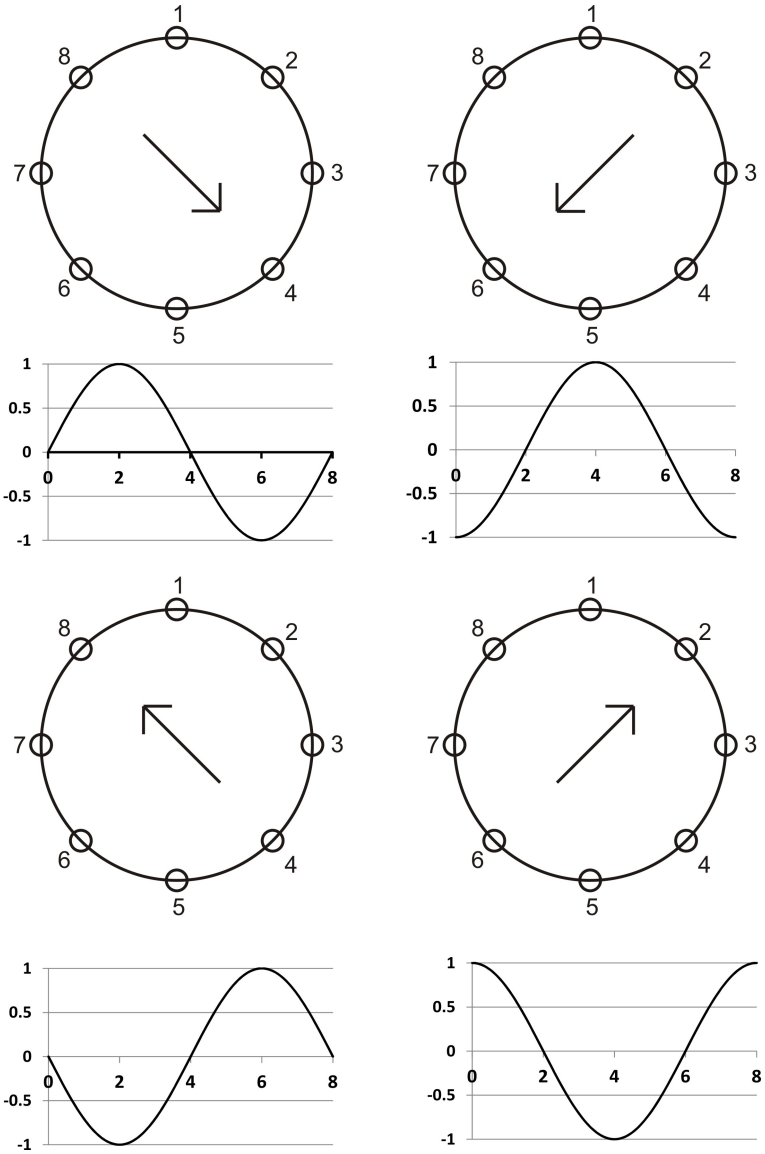

Figure 2.14: ***Rotating field in a birdcage arising out of sinusoidal variation of currents across the rungs:*** *In the pictures above, x-axis of the waves represent the rung numbers and the y-axis represent the amplitude of currents. The birdcage is represented by rungs marked as circles, connected by end ring. When there is a peak positive current through the rung numbered 2, the peak negative current would be through the rung numbered 6. This would mean that the direction of the peak field would be from rung numbered 8 to the rung numbered 4. It can be seen that as the peak current moves from the rung-2 to rung-4 and rung-6, the direction of the field rotates clockwise.*

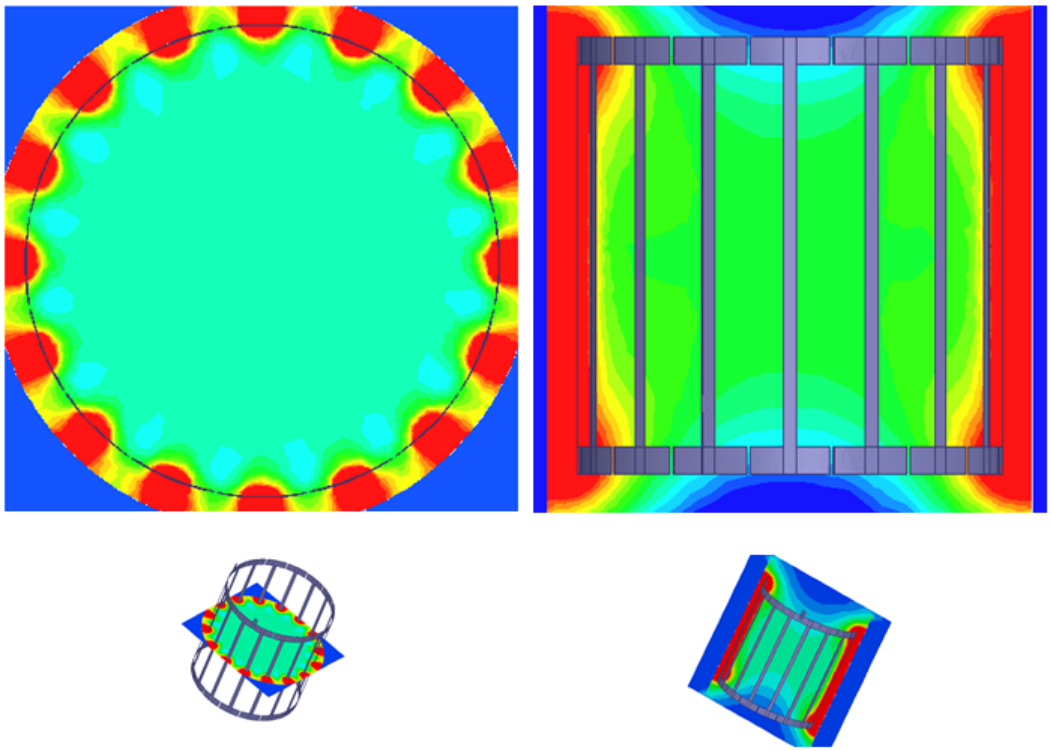

Figure 2.15: ***B_1^+ distributions*** *of a 16 rung birdcage shown over central axial (figure on the left) and sagittal (figure on the right) slices. The locations of the slices within the resonator are shown below.*

effect on the homogeneity of the generated B_1^+ and hence the images. The isolation between the In-phase and Quad-phase channels of a quadrature driven birdcage would also be affected in case of asymmetry, thereby causing a decreased efficiency (B_1^+ / sqrt(W)) and SNR as well.

2.6 Coils for Musculo Skeletal (MSK) Imaging

It is known that Magnetic Resonance Imaging is widely used in Healthcare to diagnose a range of pathologies associated with soft tissues in human body. While the methodologies developed have vastly improved imaging, there is still a tremendous need felt in improving existing hardware and techniques to broaden our understanding of human anatomy, disorders and simplify examinations for patients.

One such area that is being studied is Musculo Skeletal (MSK) Imaging. Associated predominantly with imaging tissues in peripheral joints of human body [4] like knee, ankle

[4] A number of references are presented in subsequent chapters on research in MSK and dynamic

and elbow, research in MSK imaging has evolved from developing tools for diagnosing injuries to developing hardware for sophisticated high resolution imaging of reconstructed tissues and studying their development.

Contrary to MR static imaging of joints, which are widely used and have become a default clinical standard to diagnose related injuries, dynamic imaging of MSK joints - where the tissues are studied in motion - haven't found favor among clinical practitioners, especially at higher field strengths. This is due to the fact that the techniques and hardware used for dynamic imaging of joints are yet to be developed to acceptable standards. While hardware for dynamic imaging are available with 'open bore' scanners, the low SNR obtained limits their usage for conclusive diagnosis.

In this work, a hardware solution (a receive coil array designed specifically for the anatomy and a movement device) is developed for dynamic imaging of a large animal model (minipig) that has internal tissues similar to human body. The solution is then modified and extended to a human knee, where dynamic imaging is achieved at a high spatio-temporal resolution. The RF receive arrays designed as part of these solutions are characterized for their quality parameters like noise performance, SNR, acceleration etc. and resultant dynamic images from the setup are shown as screenshots.

Apart from hardware for dynamic MSK imaging, the work also provides a hardware solution for high resolution imaging of hand and wrist, at 7 T. The results obtained from the developed Transmit coil and Receive array show that neither B_1 inhomogeneity nor SAR - challenges faced with high field imaging - are issues as far as MSK imaging of hands are concerned.

imaging.

Chapter 3

A 13 channel receive array for dynamic imaging of a minipig's knee

3.1 Introduction

The knee is the largest and one of the most complex bio-mechanical joints in the human body. Injuries to the knee joint, that supports and transmits almost the entire weight of the body and often several times the body weight during routine activities, have an enormous impact on the patient and often reduce their quality of life dramatically.

Ruptures and tears of the anterior cruciate ligament (ACL), torn cartilage or meniscus and osteoarthritis are few of the most common knee injuries/ailments in athletes [21, 22]. Due to drawbacks and controversies surrounding the existing treatment options [23–25], new therapies based on tissue engineering [26–29] and regeneration are being studied. These new methods are validated *in vivo* making use of orthopedic large animal models [30–34] like minipigs, pigs or sheep, having knees comparable to the human body.

As part of the validation in animal models, internal structures within the joint are imaged and their mechanical properties evaluated both before and after the reconstruction/therapy. While Magnetic Resonance Imaging is a useful non-invasive diagnostic modality to identify ACL tears and related injuries, the invasive arthroscopy is still considered the standard procedure to confirm the presence of fibers in good position and to

evaluate their mechanical properties. Moreover, even in regular diagnosis of knee injuries, in spite of continuous improvements in MR protocols and hardware, there are significant ambiguities and the sensitivity/specificity numbers vary from 68-100% [35]. This is especially true in cases of partial tears [35, 36] and ruptures of the ACL close to the bone, as they may appear like a stump in the MR image and therefore be misinterpreted as healthy ACLs.

For the above said complexities and issues in the biomechanical evaluation of internal structures of the joint, and for the diagnosis of ACL tears, it is believed that dynamic MR imaging of knee with high spatial/temporal resolution and high Signal-to-Noise Ratio (SNR) will offer substantial improvements. Compared to static imaging (or passive loading followed by static imaging), the complex muscle activation pattern that occurs during movement, is better represented in dynamic imaging (as the leg is in motion). Dynamic imaging has the potential to characterize and quantify mechanics of internal structures *in vivo* [37]. Soft tissue movements and abnormal internal motions can also be captured. Moreover, in the case of a torn ligament, where the tear is close to the bone, clear and precise dynamic imaging can help in an improved diagnosis and removal of ambiguities.

Numerous studies related to kinematic/dynamic imaging of human knee have been carried in the recent past and a substantial portion of the same [38–43] track and characterize movements of bones in the knee using MRI. However the motion is only quasi static, in that the knee is imaged at fixed angles and not in continuous motion like in reality. There have been studies that image knee in motion [44, 45] but they exhibit limited spatio-temporal resolutions due to limitations in coils or associated hardware. Existing techniques [46] such as Goniometers, 6 degree of freedom linkage systems and optical tracking systems are limited to study the motion of the joint as a whole by characterizing the relative position of femur and tibia and hence cannot be used to study the mechanics of underlying soft tissues. These limitations have constrained dynamic imaging from being used as a standard clinical practice.

Improvements and advances are being proposed to overcome the above said difficulties

and to make this non-invasive technique more acceptable for radiologists and comfortable for patients. As a step in this direction, dynamic imaging of the knee of an animal model (minipig) is achieved in this work by using a dedicated high-density multichannel receive array and a movement device. Minipigs are well established animal models in pre-clinical studies for orthopedic surgeries/therapies (e.g. regenerative therapies) and research due to similarities with humans in terms of skeletal parameters and bone healing rates [47]. Therefore dynamic MRI with minipigs can provide valuable and necessary data for the establishment of novel therapies for later application in humans.

Though there have been attempts in the past to image the knee in motion [44, 45, 48, 49], in this work, the advantage of combining a dedicated high-density array with a movement device is demonstrated to perform dynamic imaging of the knee of an animal model with a high spatio-temporal resolution, at 1.5 T. The chapter describes the construction and characterization of the 13 channel RF array and the movement device. The designed array is electrically characterized and the movement device is checked for reproducibility of motion. Acquired high resolution static images and snapshots from dynamic images are presented.

3.2 Materials and Methods

3.2.1 Design of the receive array

The design of a receive array for this particular subject and application involves consideration of the following important aspects:

(i) Region of interest, dimensions and geometry of the minipig's knee

(ii) Shape of coil housing adapted to the minipig's leg

(iii) Signal-to-Noise Ratio (SNR) at the region of interest (ROI)

(iv) Applicability of acceleration (partially parallel acquisitions)

(v) Electrical aspects like active/passive detuning, connector cables and cable traps

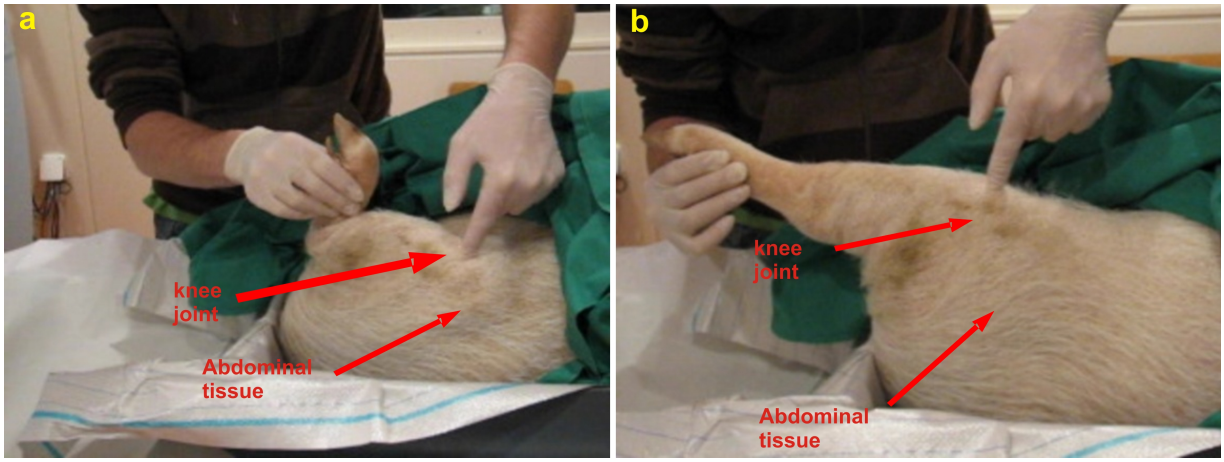

Figure 3.1: ***Curvature of the minipig's knee:*** *While the leg is in relaxed position (a), the knee is partially embedded in the abdominal tissue but when it is pulled (b), the knee moves out of the body.*

Apart from the above, changes in load and variation of the distance of the ROI from the surface during the dynamic acquisition have to be considered as well. The above points were taken into account systematically and combined with empirical results for deciding the best possible element size for the array.

3.2.2 Region of interest and coil housing

It was essential to allow an unobstructed and uniform movement of the minipig's knee during the acquisition of the "dynamic" MR signal. Therefore, the geometry of the coil had to be adapted to the minipig's knee/leg and had to be optimized to obtain the best sensitivity, SNR and parallel imaging capabilities.

The internal anatomy of a minipig's knee is structurally similar to that of a human knee, to an extent. However the complex curvature of the exterior, with the knee surrounded by abdominal muscles (as shown in Figure 3.1), makes it relatively difficult to image the internal structures in high resolution. Dynamic imaging of a minipig's knee is further complicated, as there are changes in the relative geometry of the surrounding muscles, when the knee is moved. While in the relaxed position the knee is partially embedded in the abdominal tissue (skin, fat and muscles), the knee moves out of the body when it is elongated or flexed. The regions of interest (ROI) in this study are the ligaments and the articular cartilage of the minipig's knee. They are at a depth of

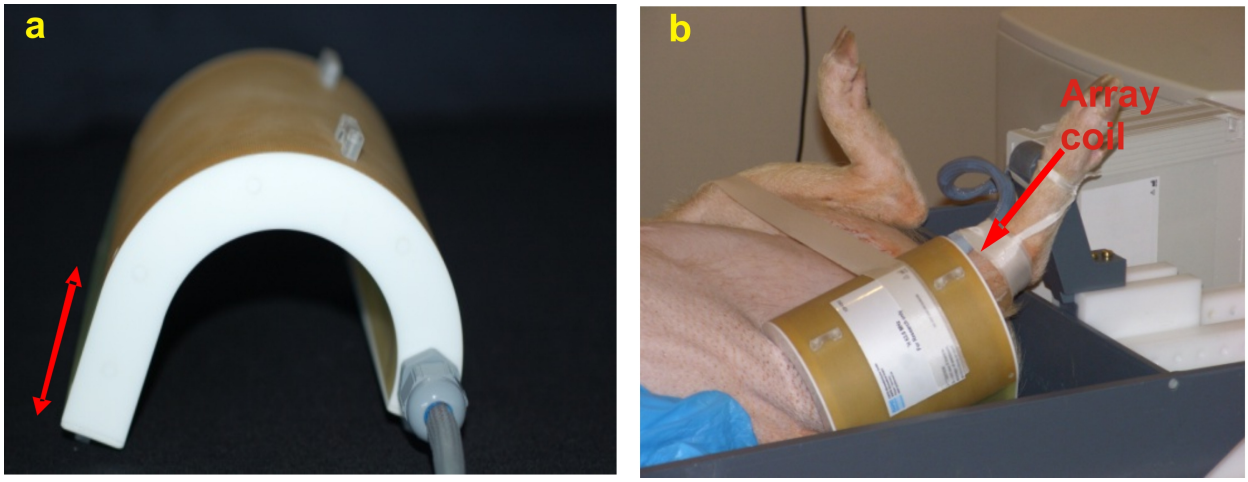

Figure 3.2: ***Coil housing shaped to the curvature of the minipig's knee:*** *The semi-circular surface is extended on one side (as shown by the arrow in a) to provide additional coverage for the ROI. The coil housing is shown placed in the minipig's knee in b.*

approximately 2 cm below the surface and this varies depending on the position of the knee during movement (as shown in the 'Results' section). The whole movement covers a length of 12 - 16 cm depending upon the size and weight of the minipig.

The coil and its housing were designed to meet these anatomical demands and limitations: A semicircular surface of 77 mm inner diameter and a length of 12 cm covers the whole knee and allows to place array elements on three sides of the knee as close as possible to the region of interest (Figure 3.2). The fourth side of the knee is "obstructed" by the minipig's body. In order to increase the coverage even further, the coil housing was extended by 47 mm on one side (the lateral side, when placed on the minipig's leg). Thus, during the whole motion the knee is covered as much as possible by the coil and an optimum filling factor[1] is achieved at all positions.

3.2.3 Determination of element size and array setup

Having decided the shape of the coil housing, the best possible element size was determined empirically. To this purpose, copper loops of various diameters (20-160 mm, width of loops having diameter less than 50 mm was 1.5 mm, width of loops having diameter

[1]Fill factor is a measure of confinement of magnetic field to the targeted ROI. As indicated in [9] and [50] a higher fill factor indicates a better sensitivity, as the losses in regions other than ROI are minimized. A higher fill factor would also lead to a higher Q ratio.

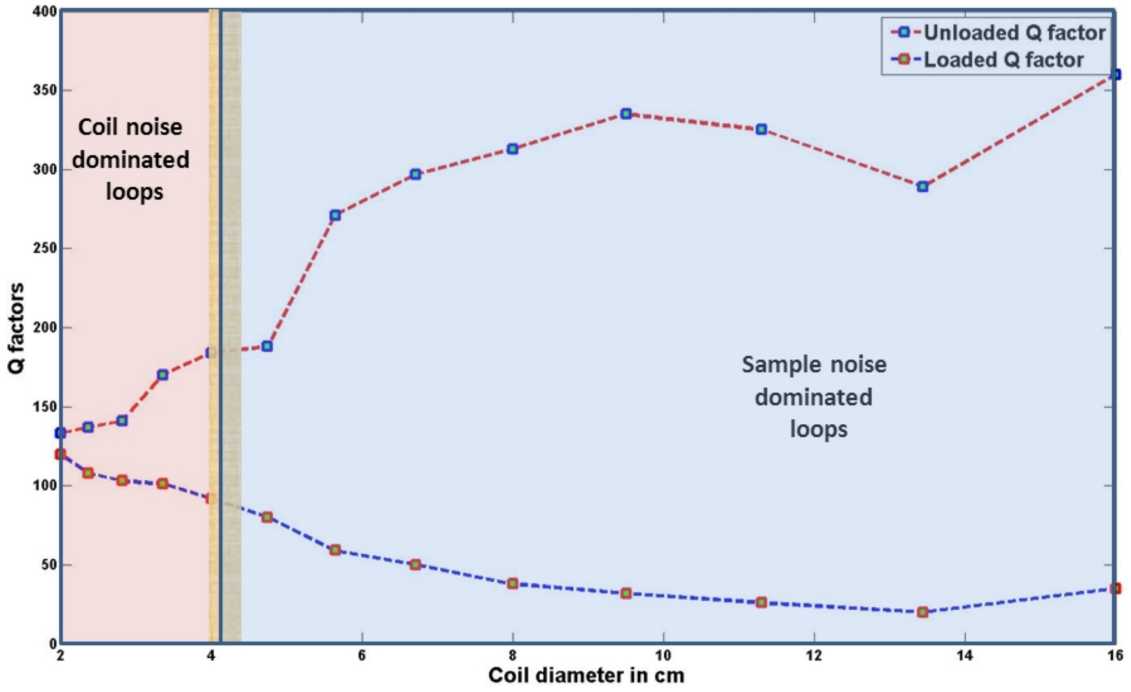

Figure 3.3: ***Change of loaded and unloaded Q factors with change in diameter of the loops:*** *As the diameter of the loops increases, the noise from the sample becomes more dominant. The coil noise and sample noise dominant loops are marked and the boundary region, where sample noise begins to dominate is marked by a light brown colored texture. While only one capacitor was used to tune the loops due to the small circumference, the loop of diameter 160 mm alone was tuned with two capacitors, as it showed a significant increase in Q on distribution of the capacitance.*

larger than 50 mm was 3 mm) were tuned to 63.6 MHz, the Larmor frequency of ^1H for a 1.5 T whole body clinical scanner (Siemens Healthcare, Erlangen, Germany), for which the array was to be designed. The loaded and unloaded Q factors of the loops were measured on the work-bench using a network analyzer and an inductively decoupled pickup loop [9]. In the case of loaded Q factor measurements, the loops of various diameters were uniformly loaded with a saline solution of conductivity 0.42 S/m (similar to that found in biological tissues) filled in a cubical container with a side of 250 mm.

The measured loaded and unloaded Q factors of the loops are shown in Figure 3.3. The relations, between the inductance of the loop (L), coil/sample resistance (R_c and R_s), sensitivity of a coil (S) and sensitivity of an ideal coil (S_0) are given here for reference (equations 1 - 3).

$$Q_{unloaded} = \frac{\omega L}{R_c} \tag{3.1}$$

$$Q_{loaded} = \frac{\omega L}{(R_c + R_s)} \tag{3.2}$$

$$S = S_0 \times \sqrt{(1 - \frac{Q_{loaded}}{Q_{unloaded}}} \tag{3.3}$$

While the reason for this type of variation of loaded and unloaded Q factors is established and well documented [9, 51], the experiment was done to determine the boundary between coil and sample noise dominated loops, at this particular frequency and to choose loops that are neither coil noise dominated nor highly sample noise dominated. This is because, though sample noise dominated loops show a larger sensitivity of the sample, the SNR tends to vary significantly, even with slight changes in load, due to change in the dominant effective sample resistance. This change in SNR is less for coil noise dominated loops, though the SNR values as such are low. In this particular case of coil design, as there is a change in load during acquisition, loops in the boundary between coil and sample noise domination were chosen, to avoid a high change in SNR during movement.

In addition to the SNR considerations, the size of the array elements directly determines the number of elements for the given geometry of the knee. While loops of larger size definitely produce higher Q drops, the number of loops that can be incorporated in an array is lower, compromising the parallel imaging capabilities of the array. The factor by which the number of phase encoding lines can be reduced depends directly on the number of loops in an array [52, 53]. It is necessary to have a large number of loops to achieve high acceleration factors, which are essential in dynamic imaging to increase the number of frames per unit time and/or spatial resolution.

Thus, the choice of smaller loops (at the boundary between coil and sample noise domination) are expected to provide high parallel imaging, though their SNR is less at higher depths. It is known that volume arrays [54] having smaller loops have higher SNR closer to the periphery of the object, whereas arrays having larger loops tends to display comparatively higher SNR in the center of the object.

With above considerations in mind, a compromise between SNR in the depth and

parallel imaging capability was achieved and 11 loops of size 43×43 mm^2 were distributed as shown in Figure 3.4, with an overlap of 7.6 mm between adjacent elements. In order to obtain an overall rectangular sensitivity profile two additional loops of size 37×25 mm^2 were placed in the remaining gaps (loops numbered 2 and 13).

In summary, the chosen size of the loops (43×43 mm^2) ensures that they are neither coil noise dominated nor highly sample noise dominated (with a Q ratio of 2.2) and offers a large number of loops for parallel imaging. The dimensions arrived were also expected to provide an optimum SNR at the depth of the ROI.

The loops were tuned to 63.6 MHz using ATC100B non-magnetic ceramic capacitors and overlapped with neighboring elements. Decoupling of the elements during transmission was achieved using actively biased PIN diodes that made a parallel LC circuit with hand wound inductors along with one of the loop capacitors. In order to allow unobstructed and uniform movement of the minipig's knee during the dynamic imaging it was important that the coil was light weight and the connection cables were flexible. To achieve this goal, the Preamplifiers of the individual elements were housed in a separate box to reduce the weight of the coil. A dedicated cable of 13 lines of 6YC6Y RF cables (Leoni AG, Germany), surrounded with heat shrink and braid was built to connect the elements with the Preamplifiers, because the commercially available cables for RF transmission did not provide sufficient flexibility. The same RF cables were used to feed the bias current required for active decoupling during transmission. Multiple cable traps for each RF channel were necessary as the length of the cable between the coil housing and preamplifier box was larger than $1/10^{th}$ of the signal wavelength in cable. The individual RF channels were realized with a minimum of 2 cable traps within the coil housing (one immediately after the loop and one before entering the connection cable) and two more in the preamplifier box. This ensured that the standing waves were suppressed and that there is little additional coupling between the channels that could directly affect the SNR. In addition, preamplifier decoupling was achieved, by a pi phase shifter (C-L-C or L-C-L depending on the actual phase shift required for individual channels) network between coil elements and Preamplifiers, to enforce further decoupling between the coil loops.

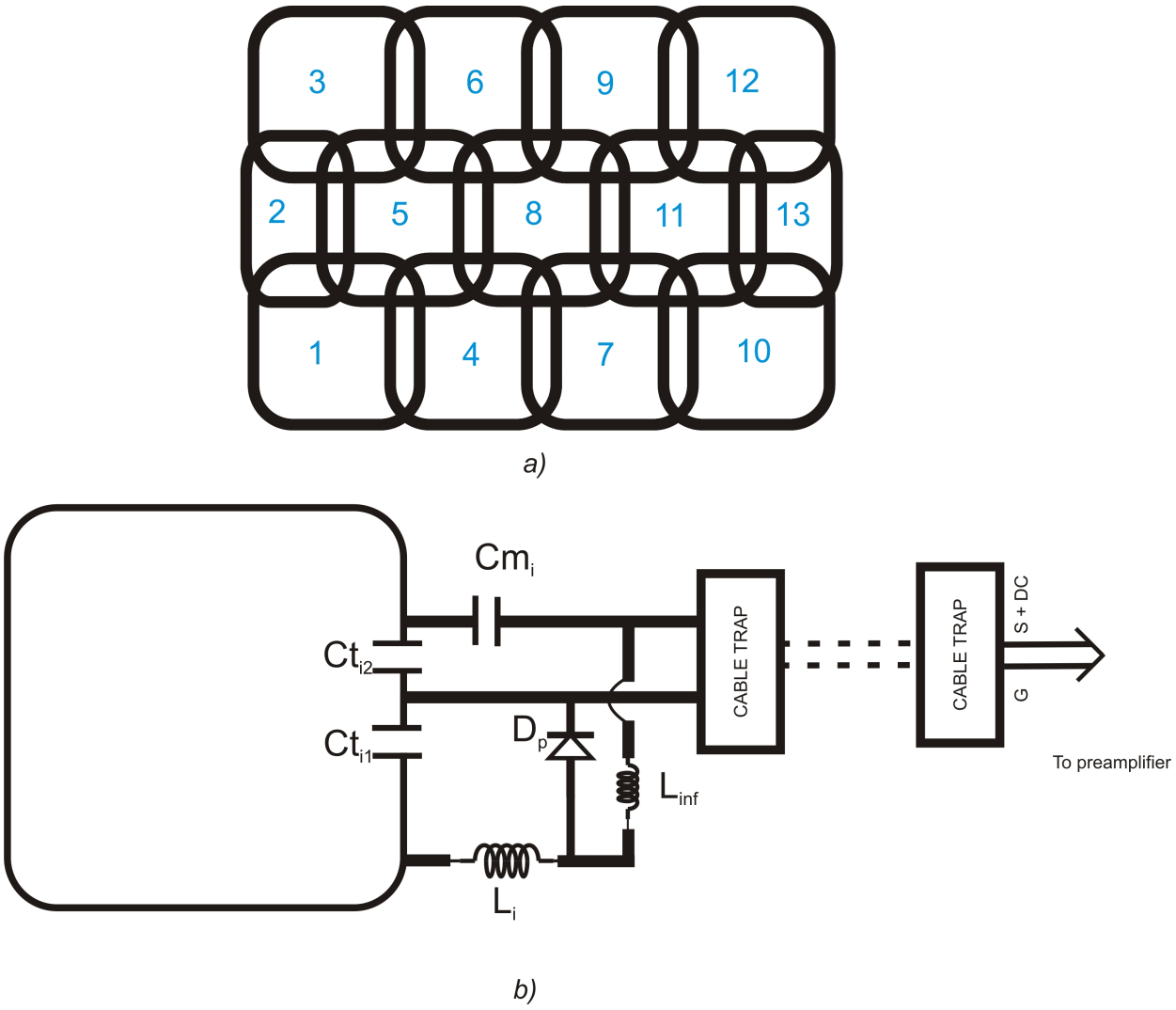

Figure 3.4: ***Array layout and equivalent circuit:*** *Part 'a' shows the distribution of the individual loops in the housing. 11 loops of size 43 × 43 mm and 2 additional loops of size 37 × 25 mm, whereas part 'b' shows the equivalent circuit of a single element. The actual overlap between the elements varied depending on the curvature in the housing where they were placed and also on the size of elements. The placement of tune/match capacitors (C_t, C_m) and active detuning inductor (L_i) are shown in the equivalent circuit.*

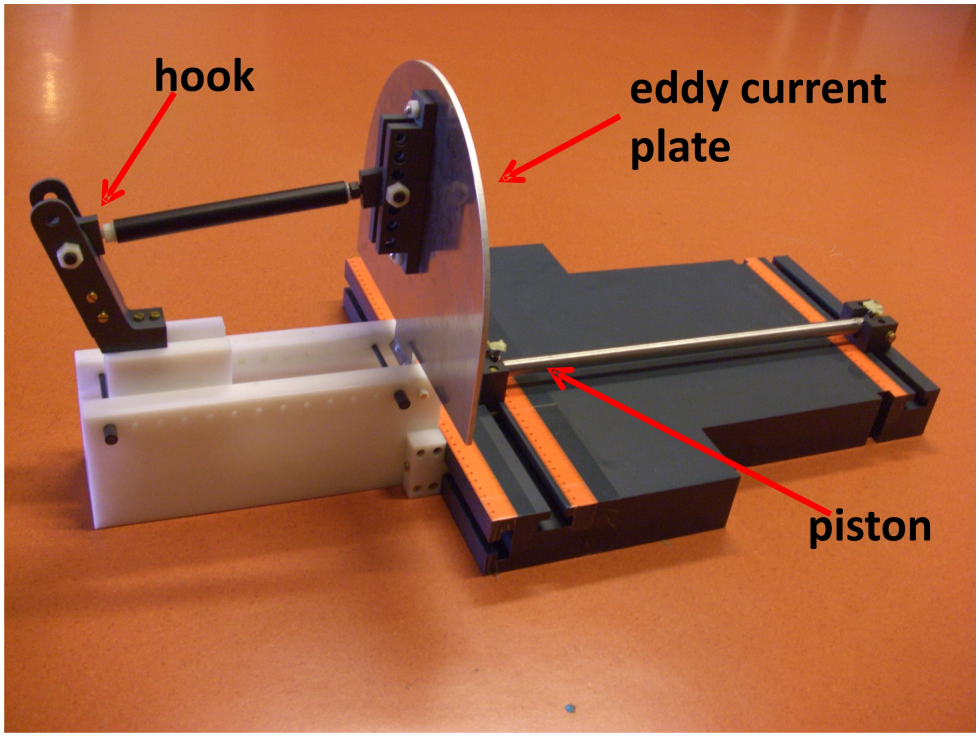

Figure 3.5: ***The movement device:*** *The hook, eddy current plate and the piston can be seen. While the pneumatically driven piston extends the minipig's knee, currents induced in the eddy current plate act as a brake to slow down the fast recoil of the knee.*

3.2.4 Movement device

To guide the movement of the minipig's knee during the measurements and in order to perform a reproducible motion during the whole acquisition, a dedicated device was constructed (as shown in Fig 3.5). The device consists of a hook connected to a piston and affixed to a PVC base. The piston was powered by pressurized air from a compressor via a pressure limiter. The inflow and outflow of air were adjusted according to the desired speed of the movement. By varying the time in which the pressured air was applied, the length of the covered distance could be adjusted. Both compressor and pressure limiter were located outside the magnet room and air was conveyed to the piston in the movement device by means of flexible ducts. An eddy current brake, in the form of an aluminium plate oriented in such a way that the surface normal of the plate is parallel to the Z axis of the system, was attached to achieve speed dependent damping. The eddy currents induced in this plate serve to minimize the recoil of the animal's knee improving the reproducibility of motion.

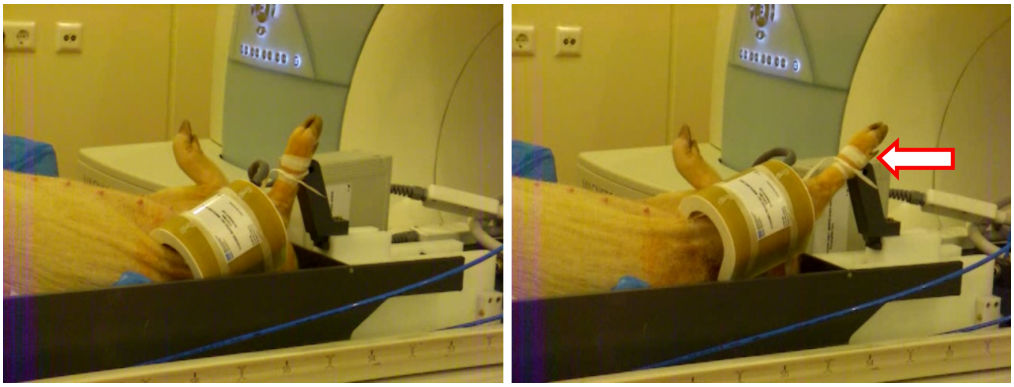

Figure 3.6: ***The coil placed above a minipig's knee:*** *The hook of the movement device (shown by the arrow) was tied to the foot of the minipig. The foot is thus pulled by the movement device to effect the motion of the knee. The photograph on the left shows the position where the knee is completely relaxed and the photograph on the right shows the position where it is elongated. Note that the array moves along with the minipig's knee. The anesthetized animal is kept in the shown test rig with the movement device and coil lying adjacent to it in the z-axis.*

An external trigger was needed to synchronize the movement device with the MR acquisition. To achieve this, a 5V voltage pulse is generated by the movement device at the beginning of every cycle. The whole setup, put in place with the minipig, is shown in Figure 3.6. As pointed by the arrow, the foot of the minipig is attached to the hook of the movement device.

3.2.5 Measurements

In order to evaluate the performance of the 13 channel array, the SNR of the constructed array and an existing array in house were compared using the pseudo-multiple acquisitions method, based on bootstrapped statistics [55]. A standard gradient echo sequence (TR = 200 ms, TE = 3.68 ms, BW= 501 Hz/pixel) and a noise scan were used to obtain the *in vivo* images for SNR comparison. The reference coil chosen for the comparison, is a commercially available 8 channel array consisting of (4+4) elements located on two separate curved housings that can be positioned close to the anatomy of interest on adjustable fixations. It is a general purpose coil that can be used for clinical imaging of a wide range of regions like ankle, knee and elbow, giving a good SNR up to a depth of 5 cm. It was the best existing array in house that could be used to try and image a minipig's

knee and it fits closely around the minipig's knee. It is important that the constructed movement device does not distort the B_0/B_1 fields and produces a reproducible consistent motion over a period of time. While the field homogeneities were checked and confirmed by mapping the fields with and without the movement device, its reproducibility was tested by observing the movement of a tubular agarose gel phantom with its motion restrained by a spring (spring constant – 110 N/m). A single projection was used to track the phantom and 50 such measurements were made in 10 minutes. Testing the repeatability of the device using a phantom enabled independent characterization of the constructed movement device.

In vivo dynamic images were acquired using a segmented FLASH sequence (TR = 4.8 ms, TE=2.38 ms, BW = 391 Hz/pixel) over 07:42 minutes (excluding the waiting time between the movement cycles. A waiting time of 2 s, for e.g. would cause the total acquisition time to be 08:30 min).

3.3 Results

3.3.1 Noise Correlation and SNR

While the isolations between adjacent elements were measured during construction of the array directly with a network analyzer and it was made sure that they were less than -15 dB (with the actual values ranging from -16 dB to -21 dB), the noise correlations obtained with MR measurements, provided a measure of isolation between other elements. Figure 3.7 shows the noise correlation matrix of the 13 channel array. The maximum correlation between any two channels is 34 %, whereas the average correlation between channels stands at 14 %.

The *in vivo* SNR reconstruction of the constructed array in comparison to a standard 8 channel coil is shown in Figure 3.8. It was obtained using a bootstrap method with 250 pseudo replicas of one image. The improvement in SNR for the new array was calculated and found to be better than the existing reference array as follows: the average SNR over the entire knee region is 130 % higher than the 8 channel reference array used in

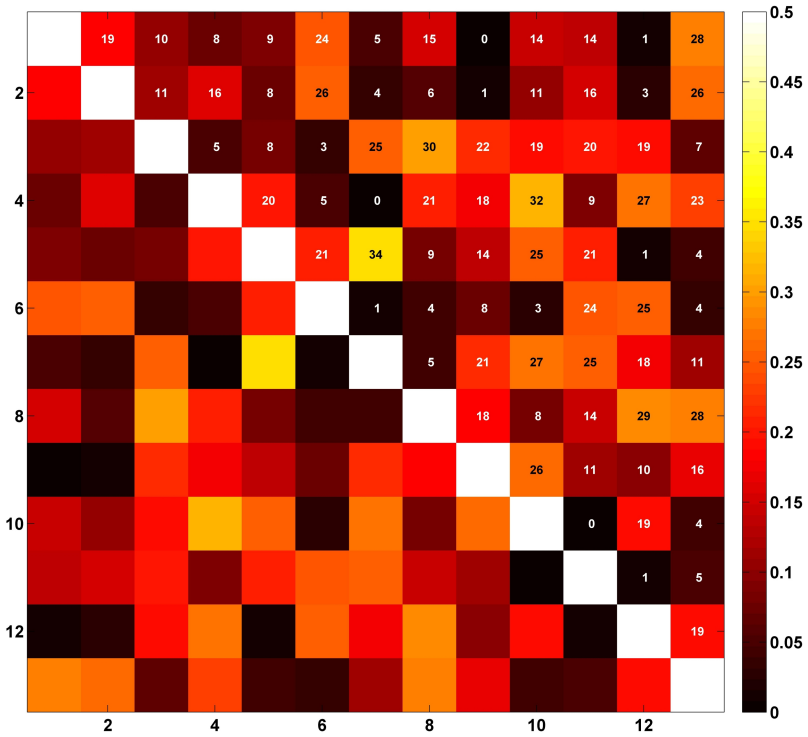

Figure 3.7: ***Noise correlation matrix of the 13 channel minipig knee array***, *with the minipig's knee as the load. Maximum correlation is 34 % and the average correlation between any two channels is 14 %. The numbering of channels correspond to the element numbers found in figure 3.4.*

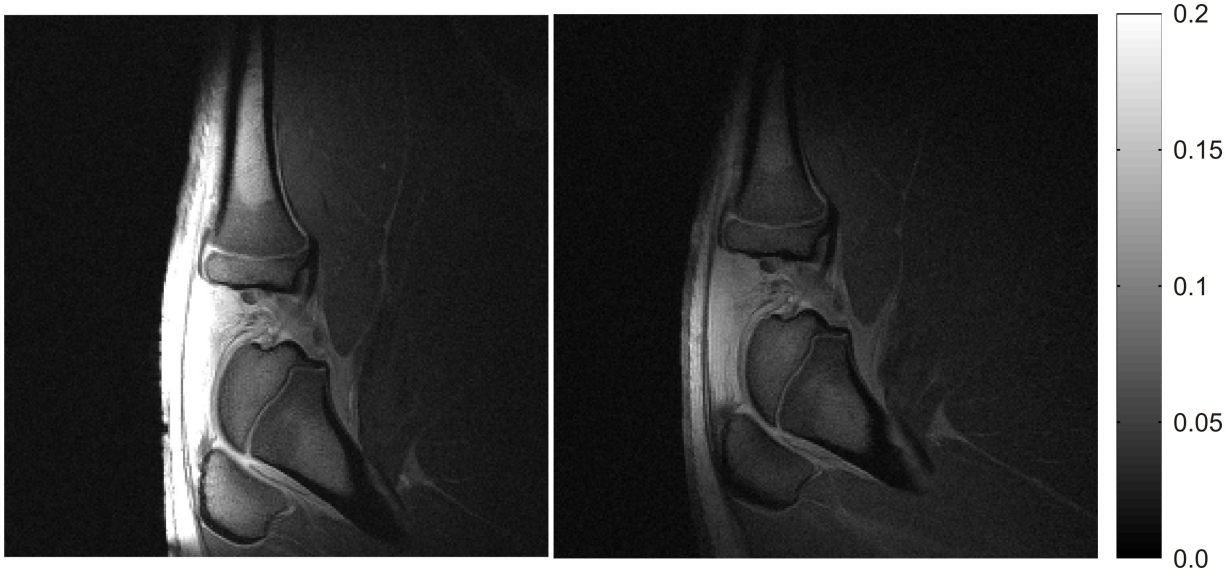

Figure 3.8: ***SNR reconstructions of a Minipig's knee*** *with the newly constructed 13 channel array (left) and an existing 8 channel coil (right), obtained with a method based on bootstrap statistics. The improvement in SNR in the region of interest with the new array is readily seen.*

comparison. When averaged only over the ROI (i.e. articular cartilages and ligaments), the SNR of the newly constructed coil is 76 % higher than that of the reference coil. The higher SNR in the periphery of the knee, due to the optimized elements, can be clearly seen. When the same SNR reconstruction is done on a phantom, the SNR at the periphery is higher by a factor of about 4, compared to the SNR at a distance of 2.5 cms. It has to be noted that the 8 channel array with larger elements, provided more uniform sensitivity profile, compared to the 13 channel array, with smaller elements. This is due to the already explained reason that the sensitivity of smaller loops decreases from the surface at a rate higher than that of larger loops. The array's parallel imaging capabilities were evaluated by means of 1/g maps in a phantom. These maps give a measure of the decrease in SNR with acceleration. The slices obtained and reconstructed using GRAPPA [52], and the 'g' maps calculated using [56] reveal (shown along with *in vivo* images in Figure 10) that an acceleration of up to 3, along the breadth of the array, is possible without any significant reduction in SNR in the ROI.

3.3.2 Reproducibility of the movement device

The measured reproducibility of the movement device is shown in Figure 3.9. The forward direction where the phantom along with the spring is pulled is shown in the part of the curve marked with an upward arrow (↑) and the reverse direction where the phantom and spring are moved backwards is marked with a downward arrow (↓). The difference in time taken by the device for forward and reverse motions is clearly seen.

3.3.3 Images and snapshots from videos

The 2D turbo spin echo static image (Fig. 3.10 – top left) demonstrates the high resolution (0.375×0.375 mm^2) obtained at the level of articular cartilage in the minipig's knee. A different slice obtained with the same sequence (Fig. 3.10 – top right) shows the posterior cruciate ligament (PCL) with high contrast. The 3-fold and 4-fold accelerated acquisitions reveal the decrease in SNR.

Snapshots of dynamic MRI of minipig's knee, done with segmented FLASH at a fine

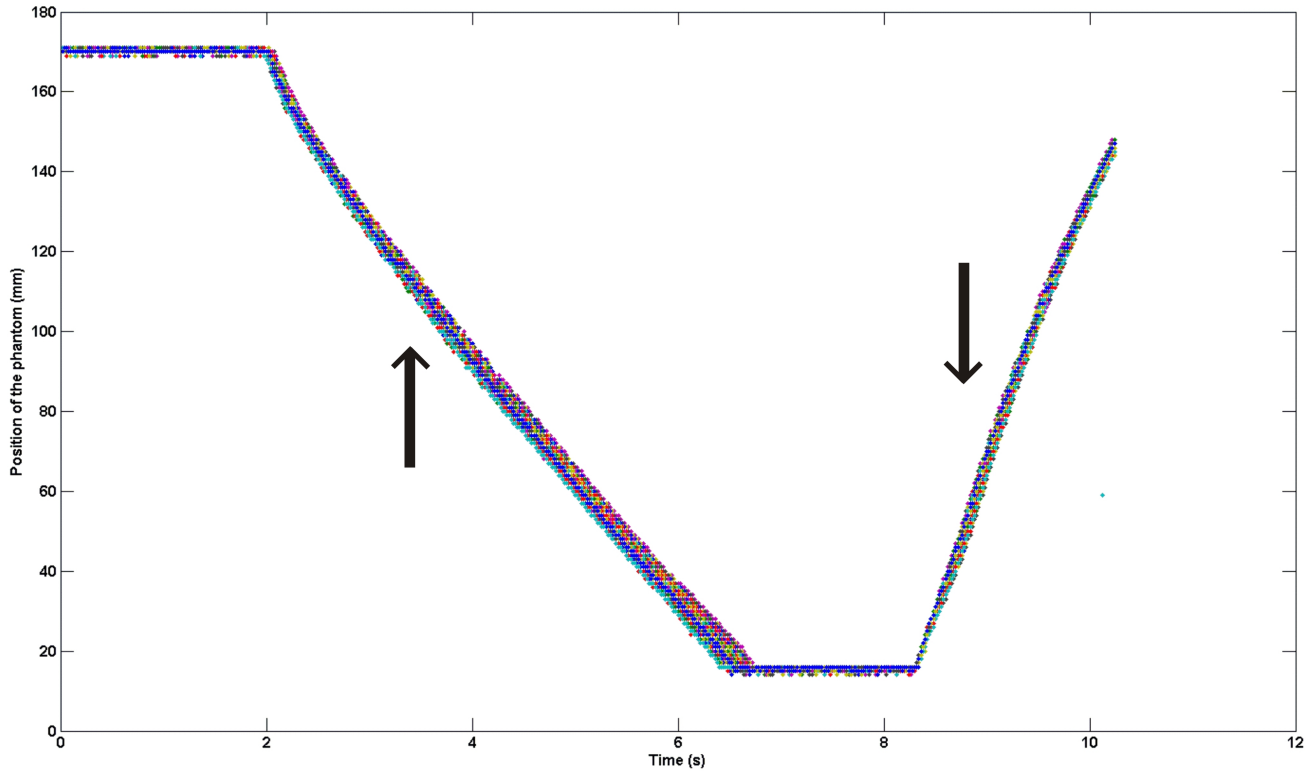

Figure 3.9: ***Reproducibility of the movement device*** *over time, shown for 50 movement cycles. The forward motion where the phantom and spring are pulled by the device is represented by the part of the curve shown by* ↑ *and the reverse motion by* ↓*. The standard deviation of the position of the phantom (along z-axis), over 50 movement cycles shows a value of 1.35 mm. This value gives a measure of reproducibility of the device.*

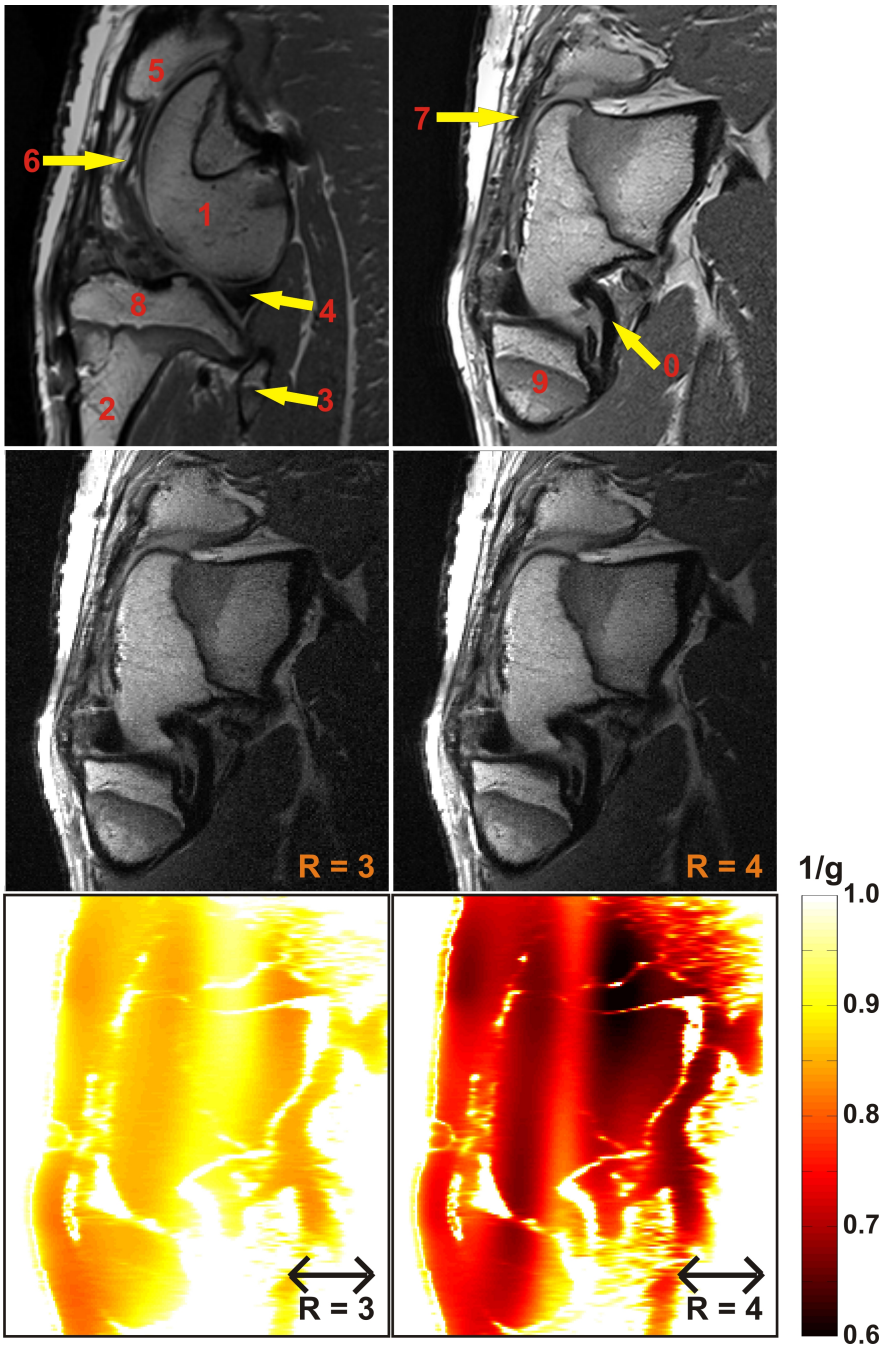

Figure 3.10: ***2D Turbo Spin-Echo static images (top row) obtained with the newly constructed array*** *in a resolution of 0.375 × 0.375 mm^2 (TR = 2150 ms TE = 18 ms BW = 100 Hz/pixel), revealing the following anatomical structures. 1 – Femur, 2 – Tibia, 3-Fibula, 4 – Meniscus, 5 – Patella, 6 - Intrapatellar fatpad, 7 - Patellar tendon, 8 – Epiphysis, 9– Metaphysis, 0 – Posterior Cruciate ligament. The middle row of images are 3 fold and 4 fold accelerated and reconstructed using GRAPPA, while the bottom row of images show the corresponding 1/g maps.*

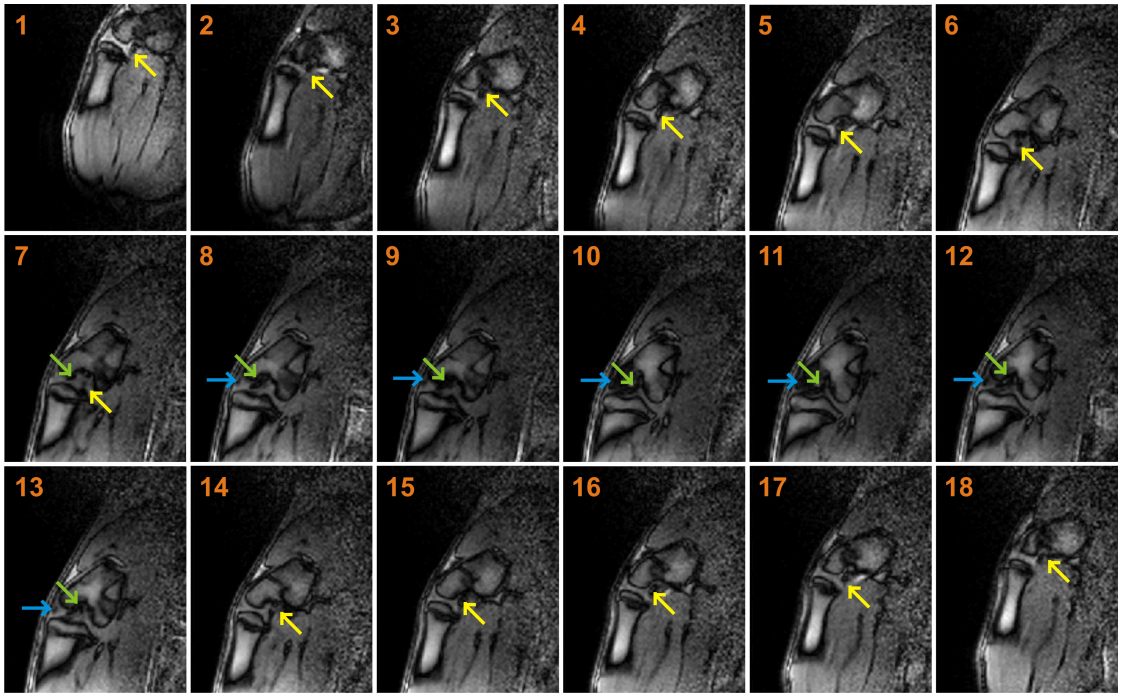

Figure 3.11: ***Snapshots of dynamic images****, covering one cycle of movement of the minipig's knee (chronological). While the yellow colored arrow shows parts of posterior cruciate ligament emerging with time, the green colored arrow shows parts of anterior cruciate ligament. Parts of extensor tendon can also be seen (blue colored arrow).*

spatial resolution of 1.16 × 1.16 mm^2 and a temporal resolution of 308 ms are shown in Figure 3.11. Complete series covering one cycle of movement of the knee from its relaxed position till its flexed position are shown, numbered chronologically. These shots are from one among the multiple slices acquired. It can be seen that parts of PCL (marked by yellow colored arrow) start to appear first followed by parts of ACL (green colored arrow) as the knee is stretched. Parts of an extensor tendon can also be seen coming into the slice along with ACL. Figure 3.12 shows some of the snapshots enlarged. Both the ligaments can be traced from their origin in the intercondyloid notch till the head of tibia at different points in time.

3.4 Discussion

In this work, a high density multichannel array with optimized elements and a movement device has been constructed for dynamic imaging of a minipig's knee. Prior to this construction, with the existing hardware it was only possible to perform static imaging of

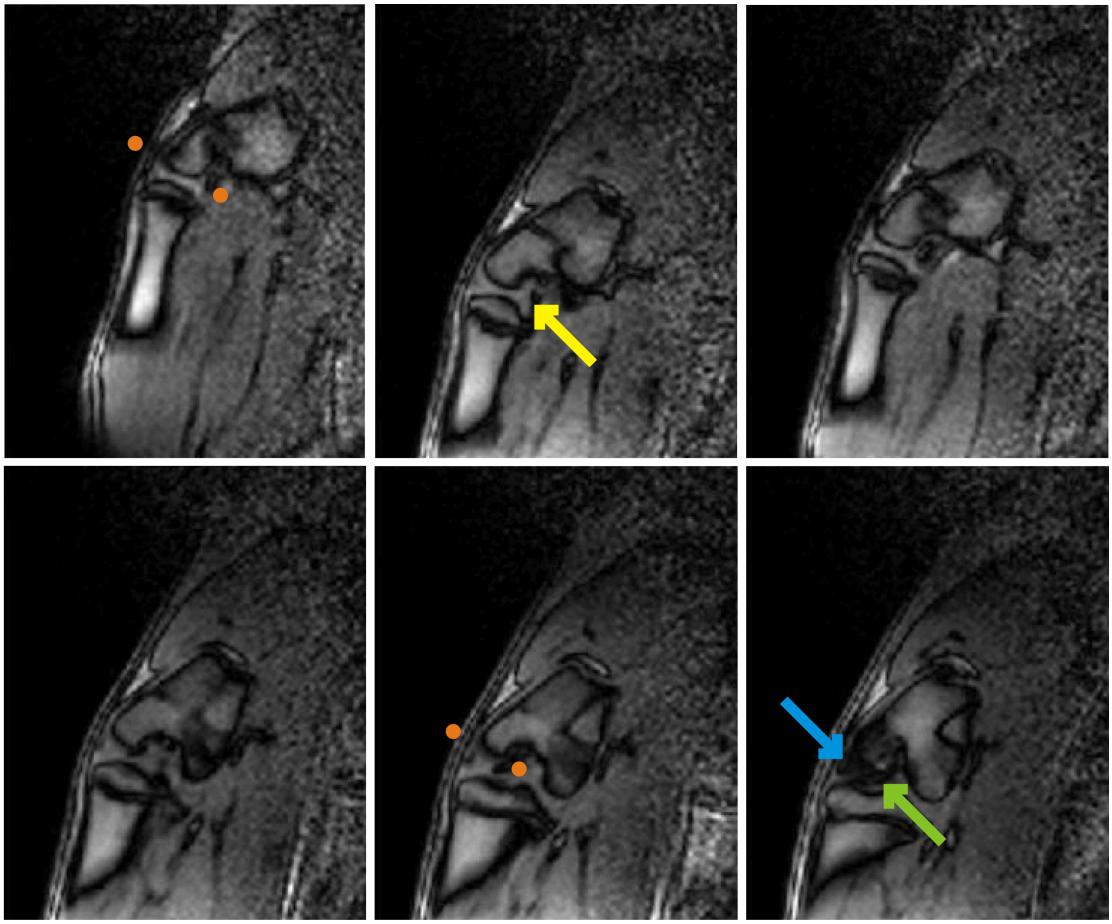

Figure 3.12: ***Snapshots from dynamic images*** *enlarged (segmented FLASH, TR = 4.81 ms TE = 2.38 ms BW = 391 Hz/pixel) acquired at a spatial resolution of 1.16 × 1.16 mm^2 and a temporal resolution of 308 ms. The two orange colored dots show a measure of the distance of the region of interest, measured at the intercondyloid notch, from the periphery. It varies from 29 mm while the knee is relaxed, as in the top left image to 22 mm in the bottom middle image, when the knee is completely stretched. Parts of posterior cruciate ligament (PCL marked by yellow arrow) can be seen attached to the head of tibia and the medical condyle in the snapshot shown in top row middle, whereas the other two images show sections of PCL between its ends. Similarly, the ACL (green arrow) can be seen in the bottom row of shots, along with parts of extensor tendon (blue arrow).*

the knee under a nominal resolution. With the unavailability of a movement device and a dedicated array, dynamic imaging of the knee of an animal model could not be carried out. The constructed optimized receive array along with the designed movement device has overcome these limitations and has been shown useful to acquire images at very fine spatial and temporal resolutions.

The static images acquired (Fig. 3.10) at an inplane resolution of 375 × 375 µm^2 reveal articular cartilage, ligaments and surrounding tissues in great clarity and detail. The contrast in the region of interest can also be seen.

Dynamic imaging on the other hand, with a high temporal resolution, reveals less anatomical details than static images, as can be seen from the time-series of snapshots shown in Figure 3.11. Nevertheless the main internal structures can be seen and traced throughout the movement of the joint from its relaxed position to a completely flexed position and then back to the relaxed position. It should be noted that it was not possible to image the ligaments as a whole, during dynamic motion, in a single slice, due to the translation and rotation of the knee. Hence sections of ligaments have to be followed in different slices at different points in time. However the entire length of the ligaments can be traced in the snapshots. This means that when the right slice is chosen, the entire length of ligaments will pass through it enabling us to image the same in motion. Parts of the entire length of PCL, right from its origin in the medial condyle of femur, till its end in posterior intercondylar area of tibia, can be traced in the snapshots 1 till 6 of Figure 3.11. And as the knee is stretched, the ACL emerges in and the PCL disappears out of the observed slice (snapshots 7 to 13 of Figure 3.11). Parts of the extensor tendon can also be seen and the entire length of ACL can be traced, like PCL.

An abnormality in either of these ligaments will manifest in the form of a missing portion that cannot be traced at any time-point, i.e. in any snapshot. As said, this is especially useful in case of tears close to the ends of ligaments, which normally appear as a 'stump' in the MR image. The ambiguity can be better resolved with dynamic imaging, as the clinician/radiologist will be able to see the entire length from its origin, minus the missing part.

It has to be mentioned that, while procedures for construction of a MRI RF receive array have been well established, there were ambiguities on deciding the size of the elements in the receive array. There were uncertainties on the kind of compromises, between large elements (for higher penetration and uniform sensitivity profile) and small elements (with high surface sensitivity and benefits of partially parallel acquisitions). Moreover, as pointed out before, there is a change in the filling factor of the coil with motion and there is also a change in depth of the ROI. As shown in Figure 3.12, the distance of the intercondyloid notch from the surface decreases by around 25 % when the knee is stretched.

With the help of the Q factor study, a coil optimized for dynamic imaging has been realized which is highly sensitive and at the same time, its sensitivity at the ROI is almost unaffected by motion. The 43 $\times$ 43 mm^2 loops chosen for the array, are close to the boundary between coil noise and sample noise dominated loops (Fig. 3.3) which avoids large changes in SNR during the motion.

The reduced weight of the coil (0.5 kg) due to placement of Preamplifiers in a separate box and a custom built flexible cable aid the free movement of the knee during dynamic imaging. Multiple cable traps help in suppressing cable waves and in improving the isolation between the channels.

The noise correlation values obtained are well below the generally accepted limit of 40 % above which strong artifacts would be induced due to distortion of B_1 homogeneity. Adjacent loops that are overlapped and preamplifier decoupled, show low correlation values of less than 20 %, whereas loops which are 'next nearest' neighbors, like loops numbered 10 and 4 (refer Figure 3.4), 8 and 3, 7 and 5, 12 and 8 show higher correlation values (slightly more than 30 %). Additional decoupling could be incorporated between these loops but the amount of copper in the high density receive array has to be kept in mind, as further addition would shield the transmit field.

The SNR comparison between the newly constructed 13 channel array and an existing 8 channel coil shows that there is a significant improvement in SNR in the region of interest, and this is largely due to the optimization of the size of the elements. Due to

the small size of elements in the newly constructed coil, the sensitivity of the coil is higher by a factor of about 3.5 near the surface, compared to the region of interest, which is at a depth of about 2 cm, below the skin. This sacrifice of uniformity in sensitivity (compared to the 8 channel coil that has a better uniformity due to its larger elements but lower SNR at the ROI) is outweighed by the benefits of small loops as shown by the SNR, 1/g maps and accelerated images [2] .A factor of 3 acceleration is tolerable and this can be utilized effectively in dynamic acquisitions to further improve the temporal resolution.

It has to be mentioned that due to the geometry of the minipig's knee and the fact that the legs do not come out straight out of the body (unlike humans), during dynamic imaging the coil gets into a position wherein it is not completely parallel to z-axis (B_0 axis). However, this way, the coil is close to the region of interest during all points in movement, thereby giving a high filling factor (which would not have been the case if the coil is positioned perfectly parallel to z-axis).

The coil could have been made longer (16 cm instead of the created 12 cm) and positioned using a fixture to cover the whole movement of the minipig's knee. This way the coil would not move and hence at certain points during movement, the filling factor achieved would be less, due to the way the knee moves. In order to get better SNR, the coil was made shorter, in such a way that it covers the whole knee for static imaging with a high filling factor and it can be allowed to move with the knee.

With segmented acquisitions as stated, the temporal resolution, SNR and the total number of acquisition cycles can be traded with one another to achieve a suitable compromise and produce dynamic images/videos as shown. The use of a movement device was mandatory, to guide and in effect drive the movement of the minipig's knee, to its full extension. This also offered an advantage in the form of uniform movement enabling the use of segmented sequences. It was noticed during examinations that though the animal was anesthetized, with certain animals, there were involuntary convulsions and hence the knee, during the motion, came back to its relaxed state at a much higher speed than at which it was pulled by the device. The use of an eddy current plate reduced this effect

[2]The non-uniformity of sensitivity can be corrected to an extent in post processing

and enabled a further uniform and smooth movement of the knee.

3.5 Conclusion / Outlook

Currently, Musculo-skeletal radiologists and surgeons involved in ligament reconstruction rely on MR for non-invasive imaging of joints. Though static imaging of joints is well established with detailed techniques and procedures, dynamic imaging at clinical scanners of 1.5 T and above is yet to be optimized. This study is a step in the direction of optimizing dynamic imaging and diagnosis at higher field strengths.

The use of a movement device along with a dedicated high density array can be extended for human applications. While a movement device is a must for dynamic imaging of knees in animal models, it offers distinct advantages even in the case of dynamic imaging of a human knee. The motion of the knee can be supported with a pneumatic/electric device, like the one used in this study. This makes the movement to be partially involuntary, thus reducing the strain on the patient, who, otherwise has to move the leg voluntarily. The whole acquisition can be over longer durations, as the strain is reduced, thus improving the spatial resolution and SNR. The uniform periodic movements achieved with the movement device can also be transferred to an increase in SNR, unlike voluntary motion where a patient might tend to have varying speeds of motion (and hence requiring a higher number of acquisitions and averages). It is believed that this combination of a high resolution receive array along with a movement device will be highly helpful in the examination and treatment of knee injuries, in the future.

Chapter Acknowledgements

While I acknowledge all those (mentioned in the Acknowledgements page at the end of this dissertation work) who guided me in this work, there are a couple of individuals whose contributions are significant in this chapter. I acknowledge the contribution of my colleagues, Joachim Schrauth and Daniel Weber, in the construction and characterization of the movement device and also in imaging the animal.

Chapter 4

A 16 channel receive array for dynamic imaging of a human knee

4.1 Introduction

Knee injuries form a major chunk of all the sports injuries reported [57–60]. Tears to ligaments, menisci and injuries to articular cartilage severely degrade the quality of life with high chances of subsequent arthritis [61–63]. Though treatments and therapies have been standardized for some of these issues, there is still a large need for research and improvement, due to the existing ambiguities and doubts [24,25]. While novel techniques on ligament reconstructions and surgeries are being developed [29,64], there is an acute demand to advance the diagnostic modalities of imaging due to the following reasons:

(i) The sensitivity and specificity of diagnoses of tears varies [35], with high ambiguities if the tears are close to the ends of the ligaments.

(ii) There is a need to monitor the treatment of articular cartilage and reconstructed or engineered ligaments in high resolution, with the knee in motion.

(iii) Non-invasive study and quantification of *in vivo* joint mechanics after therapy.

In this context, it is believed that dynamic imaging of human knee will substantially augment the existing means of diagnoses and improve our understanding of the internal

structures within the joint. Compared to static imaging or passive loading followed by static imaging, dynamic imaging represents the complex muscle activation pattern that occurs in reality, more closely. It is possible in principle to view the internal structures and observe the changes the tissues effect upon one another during the motion. Instead of quantifying the mechanics of a joint as a whole, as is done now by characterizing the relative position of tibia with respect to the femur [37, 46], dynamic imaging can be used to quantify the mechanics of tissues within the joint. In combination with static images, the videos can be used to increase certainty in the diagnoses and extent of tears. This reduces the need for invasive arthroscopy.

Despite more than a decade of research, dynamic imaging is yet to be accepted as a clinical standard, especially at high field strengths (1.5 T and above). This has a multitude of reasons that range from patient discomfort to insufficient resolution and motion artifacts. Though a controlled motion of the knee is achieved in an open MRI scanner [65] the resolution obtained is inadequate to study internal structures of the knee in motion. While some of the existing techniques of high field dynamic MR imaging use devices to move the knee [44, 66], either the range of motion is limited or the motion is not reproducible and the accompanying RF coil technology does not allow one to image the inner structures under a reasonable resolution. To overcome these restrictions, and as a step towards optimizing dynamic imaging for use in clinical practice, in this work, a whole setup consisting of a fully reproducible movement device and an optimized & dedicated multi-channel RF phased array along with an interleaved acquisition scheme is presented. The construction of the movement device and RF array are explained in detail. The setup is characterized for its reproducibility of motion and SNR/parallel imaging capabilities. Results of *in vivo* dynamic imaging are presented in the form of snapshots and 3-D reconstructions.

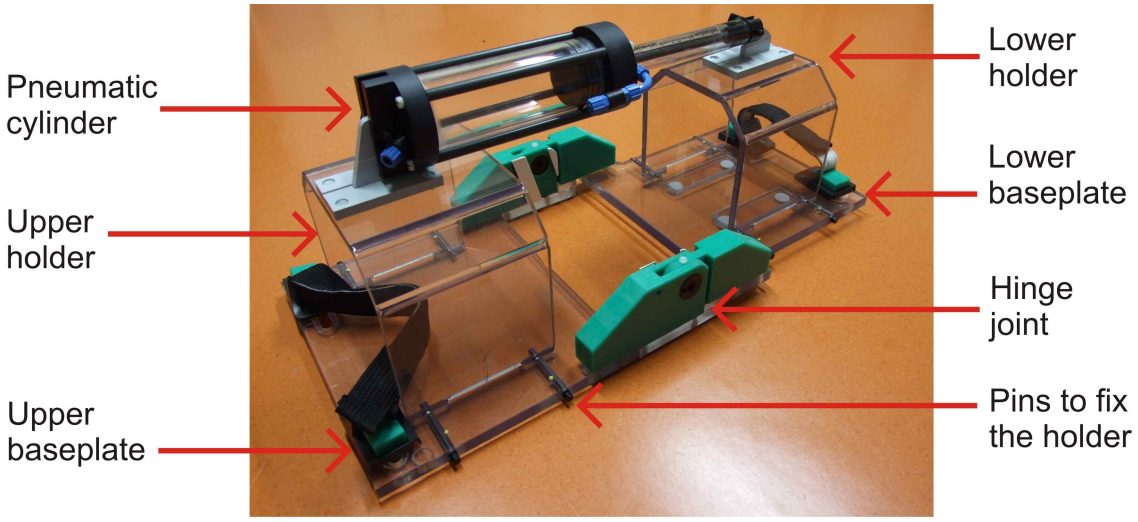

Figure 4.1: ***The movement device and its parts:*** *The pneumatic piston in the cylinder moves the lower holder along with the leg to effect the motion.*

4.2 Materials and Methods

4.2.1 Movement Device

A device to move the knee was constructed primarily to achieve reproducible motion during the scan time. This was essential to acquire a large number of k-space points/lines in a short time period, which can then be leveraged to have either an increased spatial resolution and SNR or temporal resolution. With more uniform movements, the acquired spatial or temporal resolution can be extended to multiple slices within the volume of coverage.

It was decided to place the patient prone, instead of the normal supine position. This avoids the movement of the knee in XY plane and enables us to choose a smaller field of view.

The construction of the device is best explained with the photograph of the movement device shown in figure 4.1. Keeping MR compatibility in mind, materials were selected (PETG from Simona AG, Krin, Germany) to ensure minimal distortion in the transmit field of the scanner. Two holders were designed to fit around the patient's upper and lower legs, connected by a pneumatic cylinder (with a piston) in the top. The holders were attached to individual base plates with non-magnetic pins, connected by a hinge joint. Velcro tapes were used to fix the legs to the base plates. The knee region was left

free to be able to have a dedicated coil around the same.

The home-made piston is powered by pressurized air from a compressor and a pressure limiter, controlled by an electric unit. Provisions were made to adjust the pressure of the air and control the speed of movement of the device. A light sensor based rotary encoder is incorporated in the hinge joint to synchronize the acquisition and movement. The extent to which the lower holder is moved or the maximum angle to which the leg is lifted can also be adjusted by the rotary encoder. The motion is started by a switch placed on a control board in the console room that also displays the direction of motion. 5 V trigger pulses at the start of each movement cycle, from the control board to the scanner, starts the different segments of acquisition. The movement can be stopped, after the measurement, by the switch in the control board or during the measurement by an emergency switch that is placed next to the patient.

Operation: The patient is positioned on the scanner table without the holders, with their leg above the base plates and the coil in between the plates (shown in detail in figure 4.2). The holders are then placed above their leg and attached to the base plate by the pins. The maximum angle, which depends on the patient size, is determined and the rotary encoder is adjusted for the same. The patient is then moved into the magnet bore for measurement.

4.2.2 RF Array

The existing coils for conventional knee imaging on a 1.5 T whole body scanner either do not allow a free movement of the lower leg or produce inadequate SNR at the regions of interest (ROI), which are the articular cartilage and cruciate ligaments. Multichannel arrays available for imaging the knee can be used to produce high resolution static images, but only a little movement of the knee can be achieved. The standard detachable knee arrays (with one half removed) can be used to effect the whole movement required (within the bore of the scanner) and are compatible with the designed movement device, but the SNR at the region of interest is low (as one needs to remove a half) and it gets further reduced when the acquisition is accelerated. The flexible surface loops that were supplied

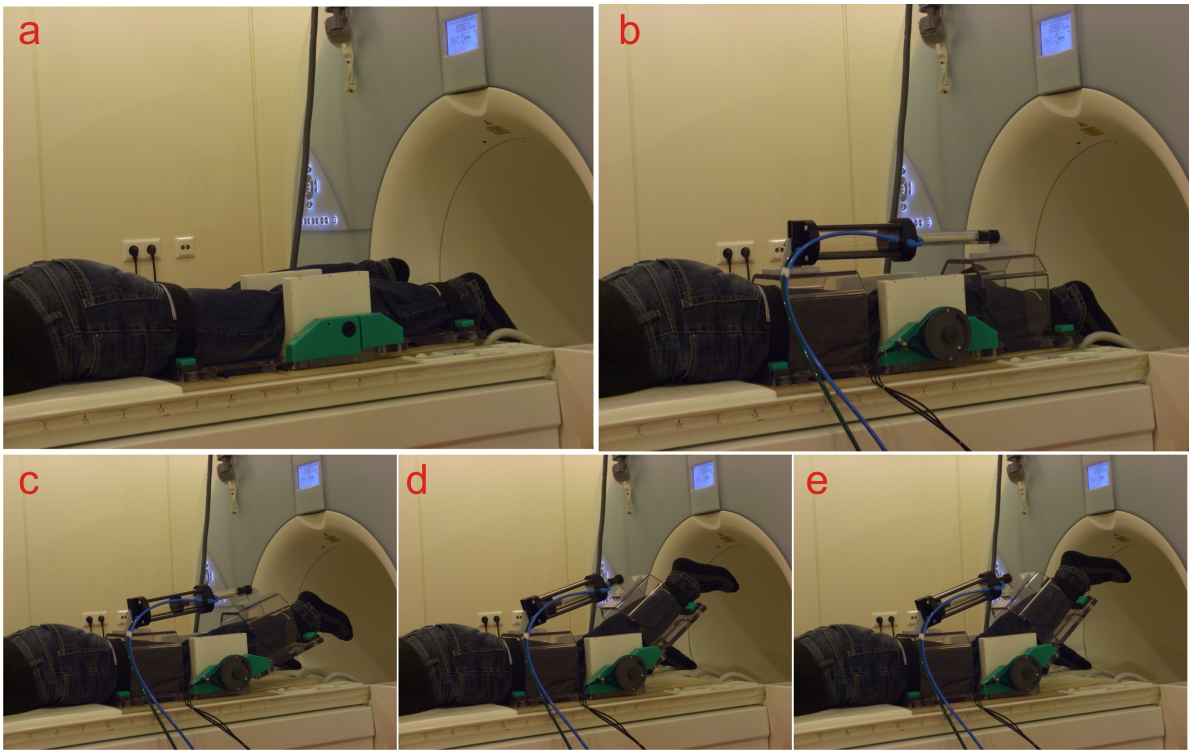

Figure 4.2: ***Human knee array - Coil and movement device setup:*** *The top row of images show how the patient is positioned in the setup and the bottom row of images are the snapshots of the setup in action. The patient is first positioned above the base plates and the coil ('a') after which the holders and the piston are placed ('b'). 'c', 'd' and 'e' shows the movement of the leg outside the bore. The maximum angle (as in 'e') is determined outside the scanner and the rotary encoder is adjusted.*

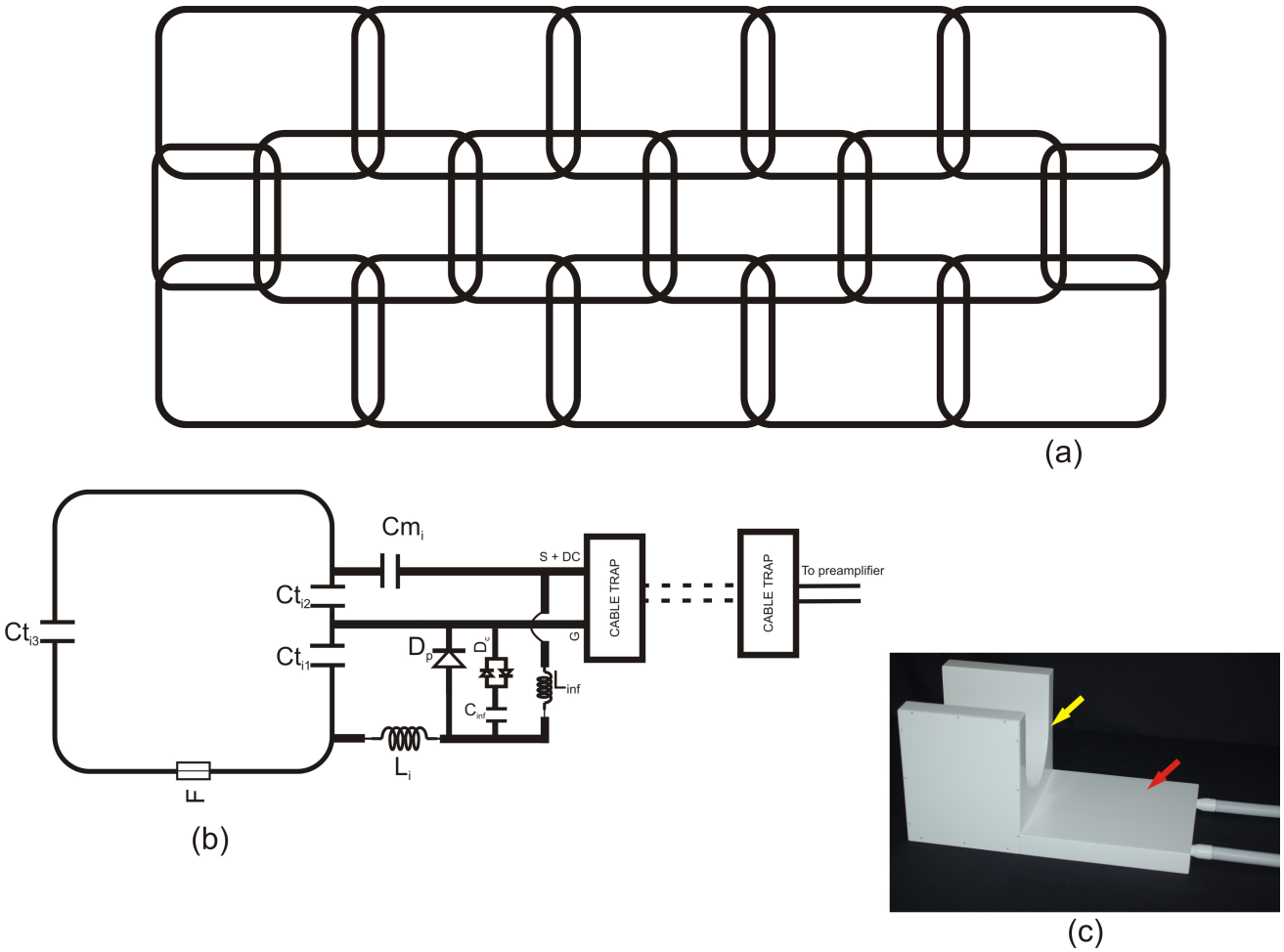

Figure 4.3: ***The distribution of the loops (a), the equivalent circuit of a single RF channel (b) and the constructed coil (c) are shown.*** *In the coil, the loops are placed below the U shaped region (marked by the yellow colored arrow) while the preamplifiers and associated electronics are located in the part of the housing shown by the red colored arrow.*

with the scanner were found unsuitable for the same reason. Hence a dedicated high-density RF array was designed and constructed.

For optimum coverage and compatibility with the movement device, the coil has elements on 3 sides of the knee (Fig. 4.3), leaving the top uncovered to position the leg.

The cruciate ligaments of a human knee of average size lie at a depth of 6 to 12 cm whereas the articular cartilage starts relatively close to the surface at 3 cm. Considering this and the fact that the SNR of an array decreases with distance from the surface [54], 16 elements of size 80 x 60 mm^2 were distributed across a semi-cylindrical surface of diameter 16 cm, with an overlap of 10 mm and extended on both sides by 7.8 cm. This is shown in figure 4.3.

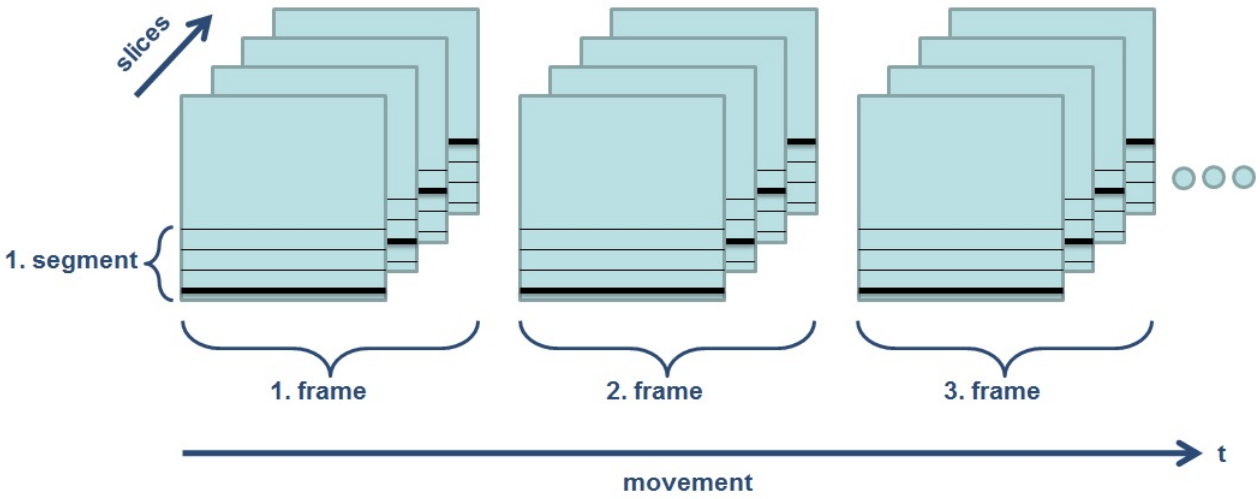

Figure 4.4: ***Dynamic acquisition scheme:*** *The order of acquisition of k-space lines of different slices at subsequent frames can be seen.*

The individual elements were tuned to 63.6 MHz, the Larmor frequency of a 1.5 T whole body MRI scanner (Magnetom Avanto, Siemens Healthcare, Erlangen, Germany) with the adjacent elements overlapped. The preamplifiers for the elements were housed below the base plate of the movement device. This way, the preamplifiers can be close to the elements but not in the ROI and at the same time compatible with the movement device as shown in part 'c' of figure 4.3. Multiple cable traps were incorporated in each channel, as the electrical length between the elements and the preamplifiers was greater than 1/10th of the wavelength in the cable. Phase shifters along with the low input impedance of the Preamplifiers were used to enforce further decoupling between the coil elements [10]. While the elements are actively decoupled during transmission, passive decoupling using anti-parallel diodes and fuses are incorporated for added safety, as shown in part 'b' of figure 4.3. The positioning of the coil and the movement device is shown in figure 4.2.

4.2.3 Sequences

The average duration of one movement cycle is 5 s, though it can be adjusted by the pressure of the air from the limiter. With an aim to achieve a high frame rate in the videos, good SNR in the ROI and a high spatial resolution, it was decided to use segmented FLASH with an interleaved slice scheme shown in figure 4.4.

In a standard segmented FLASH sequence the acquisition time needed for a single frame is reduced resulting in a higher frame rate. But the number of movement cycles to acquire one complete k-space increases, depending on the number of lines acquired per segment. Moreover, the restriction in TR would have limited the flip angle that can be used. To overcome the above constraints, it was decided to interleave apart from segmenting the sequence.

Here, the acquisition of a k-space line in one slice in one segment is followed by the acquisition of the next k-space line in the next slice in the same segment (as marked by bold lines in Fig.4.4). In subsequent movement cycles, the k-space lines of segments are filled. This way, a higher effective TR is achieved and hence higher flip angles can be used, as a higher time is available for magnetization in different slices to relax. This transforms to a better SNR, in a given spatial resolution.

4.2.4 Measurements

In the dynamic acquisition with interleaved sequences, it is important that the movement is completely uniform and repeatable over a large number of cycles. This characteristic of the device (henceforth called reproducibility) was measured by following the movement of a test tube shaped water phantom with agarose, using a radial FLASH sequence with four projections. The 4 projections consisted of one vertical and one horizontal projection with two unused projections in between them, over 50 movement cycles (TR=4.46 ms, 512 repetitions).

The coil elements were characterized on the workbench for their Q factors, isolation (between adjacent elements) and active decoupling (measured as the difference in transmission in a inductively decoupled sniffer loop pair, between the resonant and off-resonant states of elements). Noise scans in the scanner revealed correlations between all elements and the GRAPPA 'g' factor distributions were calculated [56] on a tissue simulating phantom (1.25 g $NiSo_4.6H_2O$ + 5 g NaCl per 1 l of H_20). The constructed coil was also characterized for its *in vivo* SNR using a standard SE sequence (256 x 256, TR 1000 ms, TE 100 ms) and the same was compared to a commercially available 8

channel multi purpose array. The SNR here was calculated using the Pseudo Multiple acquisitions method described in section 2.2.

Dynamic acquisition was performed with the following parameters: Segmented Interleaved FLASH (as described in the sequences section before), TR 5 ms, TE 2.38 ms, FOV 180 x 180 mm^2, Matrix 256 x 256, Slice thickness 2.5 mm, No: of slices 32 with a distance factor of 30 %, 25 frames per movement, Flip angle 60°, Bandwidth 610 Hz/pixel, Number of segments 8. The total acquisition time was 17:04 min.

The total acquisition time varies between patients due to the change in the maximum angle by which the patient's leg is lifted by the movement device, which in turn depends on their size. The echo time was fixed at 2.38 ms for all acquisitions so that there is an opposing phase between fat and water . This enables clear separation between different tissues so that easy image segmentation can be achieved for 3D reconstructions.

4.3 Results

Movement device

The sequences available in the scanner ('field' and 'rf_field', software version VB 17) to obtain the RF and B_0 field distributions were utilized to check for distortions caused by the presence of the movement device. The field maps remain unchanged with and without the device, indicating that there is no visible distortion caused by the same.

The measured reproducibility of the movement device is shown in figure 4.5. While it is readily seen that the movement is perfectly repeatable, there is a difference in the time taken for the upward and downward motions. However, this doesn't affect the acquisition of the dynamic data.

RF Array

The unloaded Q factor of the elements was 250. The loaded Q factor varied between 110 to 140 depending upon the position of the element in the array and size of the knee. This tells us that the receive elements are in the border between coil and sample noise domination.

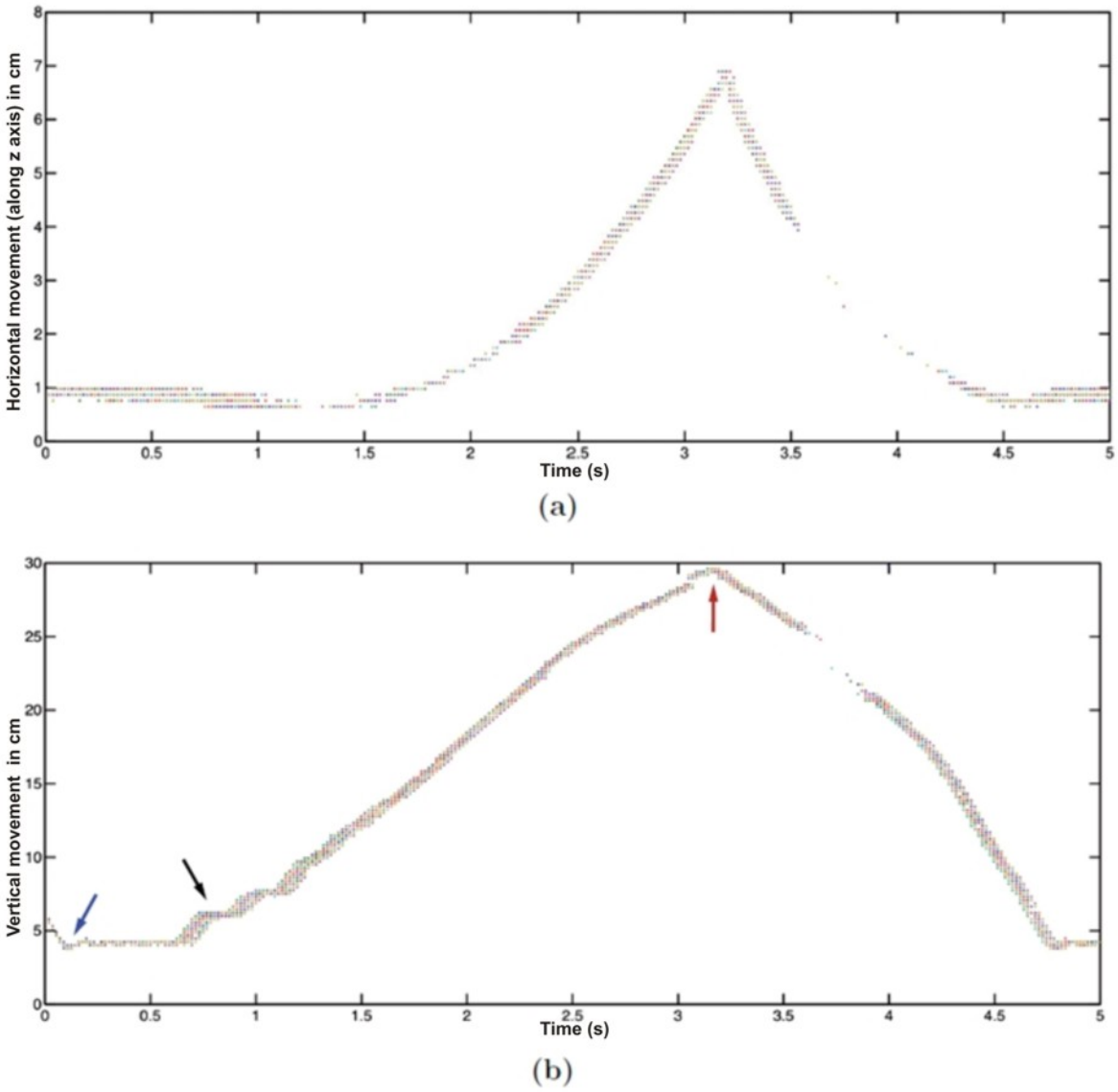

Figure 4.5: ***Reproducibility of the movement device in vertical (a) and horizontal (b) directions, shown over 50 cycles of movement.*** *The data is acquired by placing a tube-shaped phantom in the lower holder and observing the movement with a radial FLASH. The device does have certain non-uniform discrete movements, as marked. But these do not affect the data acquisition in any way as even these discontinuities are repeatable.*

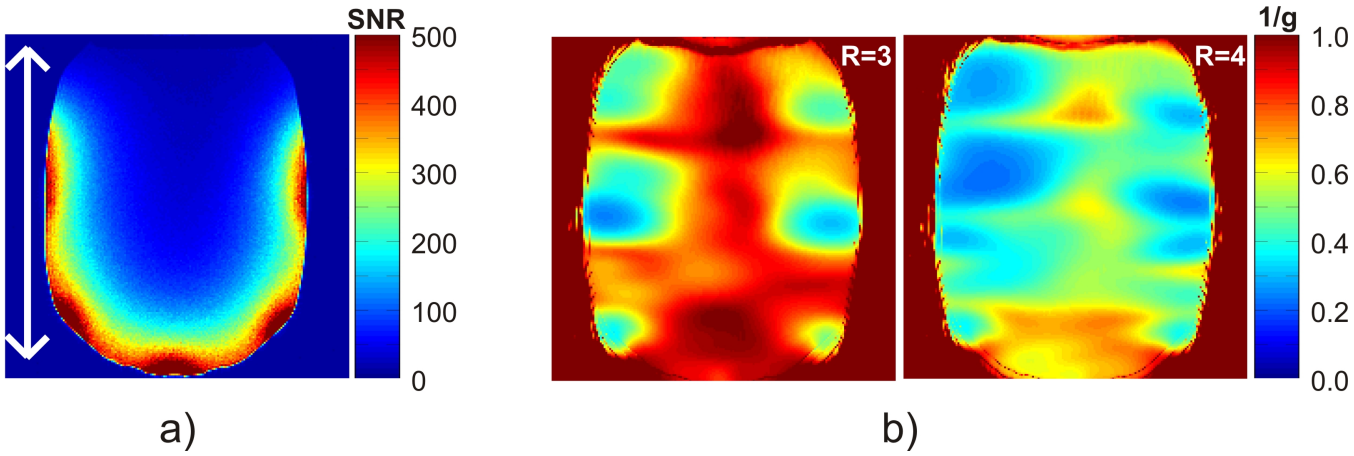

Figure 4.6: ***SNR and 1/g maps:*** *The SNR distribution of the constructed array is shown in part 'a'. The decrease of SNR away from the periphery of the phantom, for a high density array, can be seen.The 1/g maps of the constructed receive array for 3-fold and 4-fold GRAPPA accelerations, along the direction marked in the SNR map, are shown in part 'b'. The 1/g map corresponding to 2-fold acceleration is not shown as it is nearly equal to 1 almost everywhere in the FOV. Although it is possible to also accelerate in HF and LR directions, these maps are not shown, as it is irrelevant for this application.*

The elements show an active decoupling larger than 38 dB. This is important to minimize B_1^+ inhomogeneity during transmission. The isolation between neighboring elements was better than 16 dB. The noise correlation measurements done on the scanner, with the coil loaded by a human knee, reveal an average correlation of 12% between the elements, with the maximum correlation being 30%. The obtained sensitivity profile, as can be seen in the SNR map shown in figure 4.6 does not show any distortion due to element coupling, implying that the elements are sufficiently decoupled. There is no significant change in the above obtained correlation values with the position of the knee.

Figure 4.6 shows the 1/g maps obtained with reconstructions done using GRAPPA for the A-P direction. It should be pointed out that, with the described interleaved acquisition scheme, and with the geometry of the ROI, it is possible to accelerate only in A-P direction. While 2-fold and 3-fold accelerations give images with a tolerable reduction in SNR, R=4 increases the g factors to a significant extent, degrading the image quality.

The *in vivo* comparison of the SNR of the constructed coil with the commercially available 8 channel array is shown in figure 4.7. SNR averaged over the complete knee region shows a significant improvement with the new coil, as stated in the figure description.

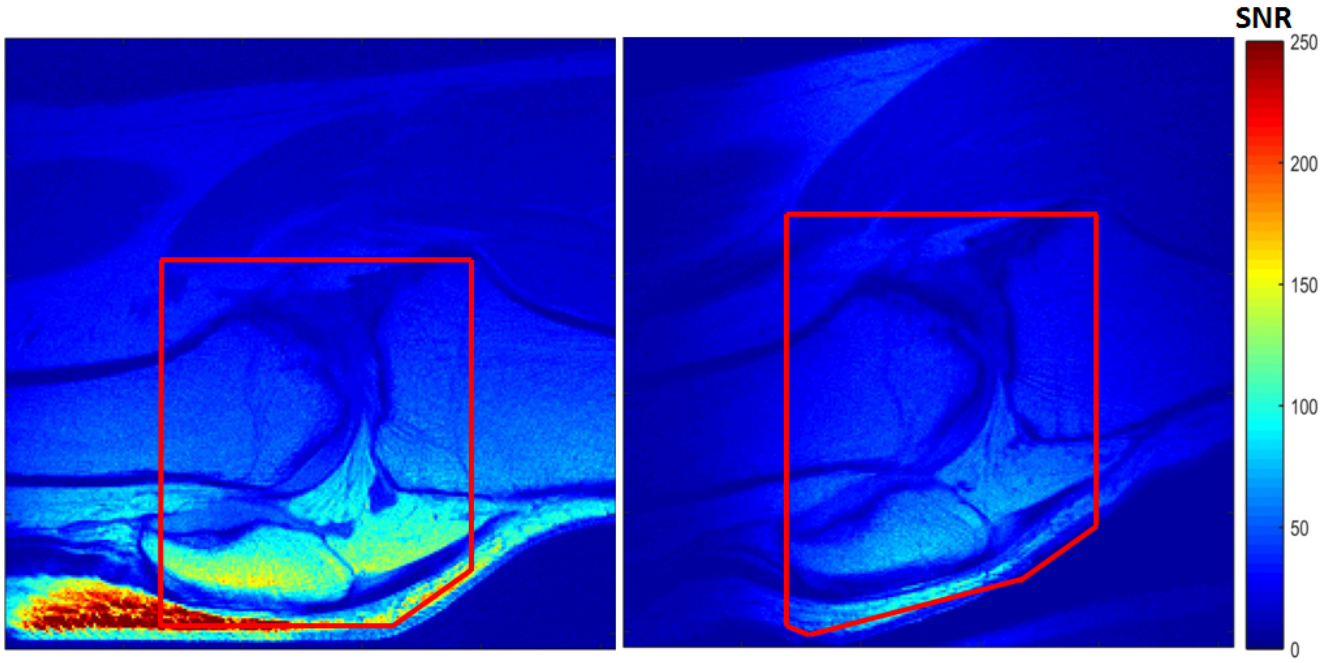

Figure 4.7: ***In vivo SNR comparison*** *of the constructed knee array with a commercially available 8 channel array. The image obtained with the new array is shown on the left whereas the image obtained with the available 8 channel array is shown on the right. The improvement in SNR over the entire knee region is clearly visible. Average SNR over the region marked turns out to be 51 for the constructed array whereas it is 31 for the existing coil.*

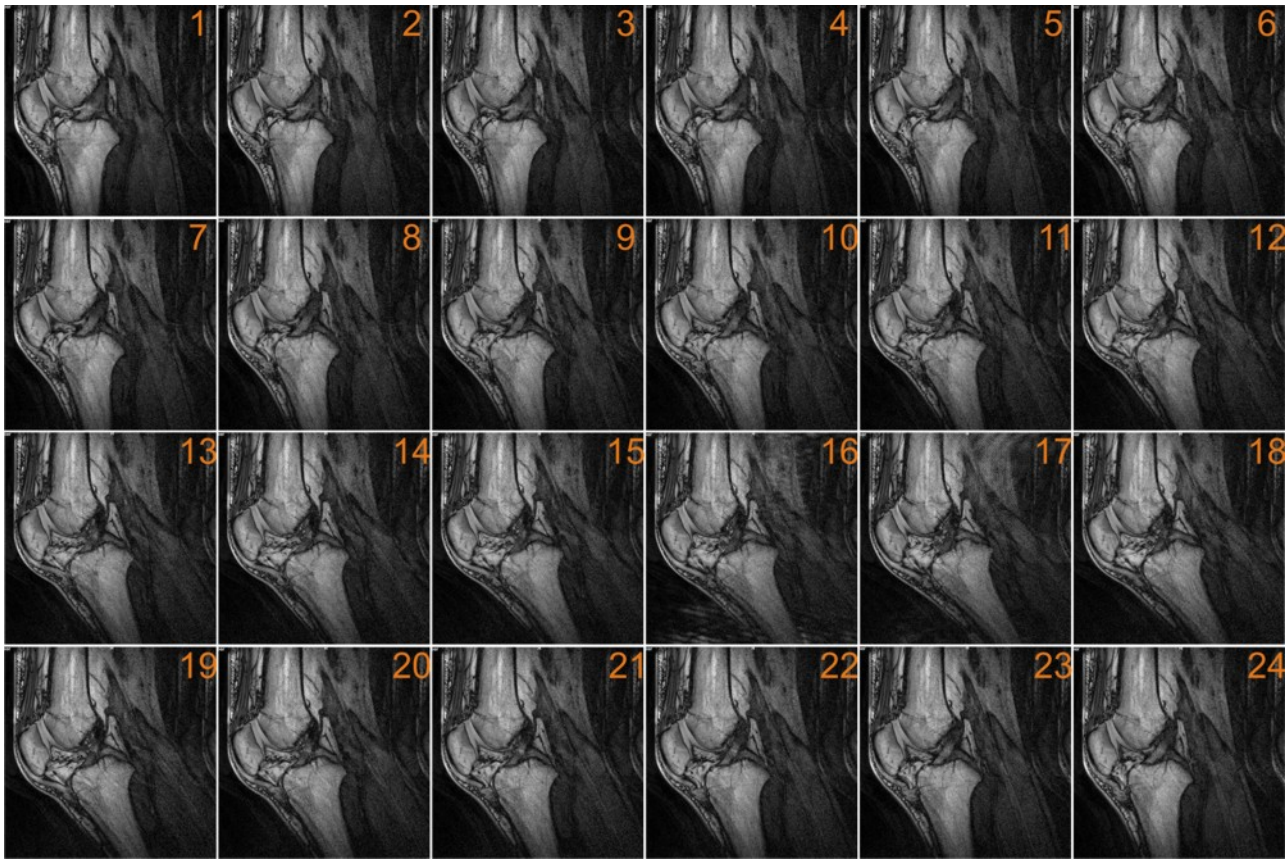

Figure 4.8: ***Snapshots of dynamic imaging*** *of a single slice out of 32 slices at an in-plane resolution of 0.7 x 0.7 mm2 and a temporal resolution of 160 ms. As can be seen in the images, when viewed in ascending order, the femur stays stationary, affixed to the upper holder of the movement device, while the tibia is moved by the lower holder. The images represent one cycle of movement of the lower leg and show the movement of internal structures, like cruciate ligaments.*

Dynamic snapshots

Figure 4.8 shows the snapshots of one slice out of the total dynamic data acquired on the knee of a volunteer. The snapshots are taken from the video reconstructed using DICOM images. In this case, one cycle of movement took 4 s. The leg was moved up by an angle of approximately 35°. The knee can be seen in its maximum bending angle in the 17^{th} frame. The articular cartilage and the cruciate ligaments are visible in the shown slice throughout the movement, at an inplane resolution of 0.7 x 0.7 mm^2 and a temporal resolution of 160 ms. The internal structures are marked in the enlarged dynamic snapshots in figure 4.9. In the same figure the snapshots are also accelerated (up to 4-fold) using GRAPPA. These images give an idea of the decrease in SNR due to the acceleration. The 3D segmentation of the acquired dynamic data are shown in figure 4.10. The constructed movement device and the RF array were used in combination with the normal segmented FLASH as well as the designed interleaved acquisition scheme.

4.4 Discussion

A whole package for improved dynamic imaging of a human knee at a clinically relevant field strength, consisting of an active movement device, a dedicated multichannel array and an optimized acquisition scheme has been presented. Prior to this work, it was possible to acquire high resolution static images of knee at various angles or dynamic single-slice images with low spatio-temporal resolution. Though real-time MRI has been demonstrated with a higher temporal resolution, the spatial resolution obtained limited the study of internal structures. With the characterized setup, 4D MRI, i.e. dynamic MRI at 3D has been demonstrated *in vivo* at sub-mm spatial and a high temporal resolution. The constructed movement device shows enough reproducibility over a sufficient number of cycles to allow the acquisition to be split into multiple cycle and segments. A little mechanical imperfection in the device causes a few uneven discrete steps when the movement is started. But within a second, the movement turns uniform, as can be seen in the reproducibility curve. However these ripples do not affect the acquisition, as they are

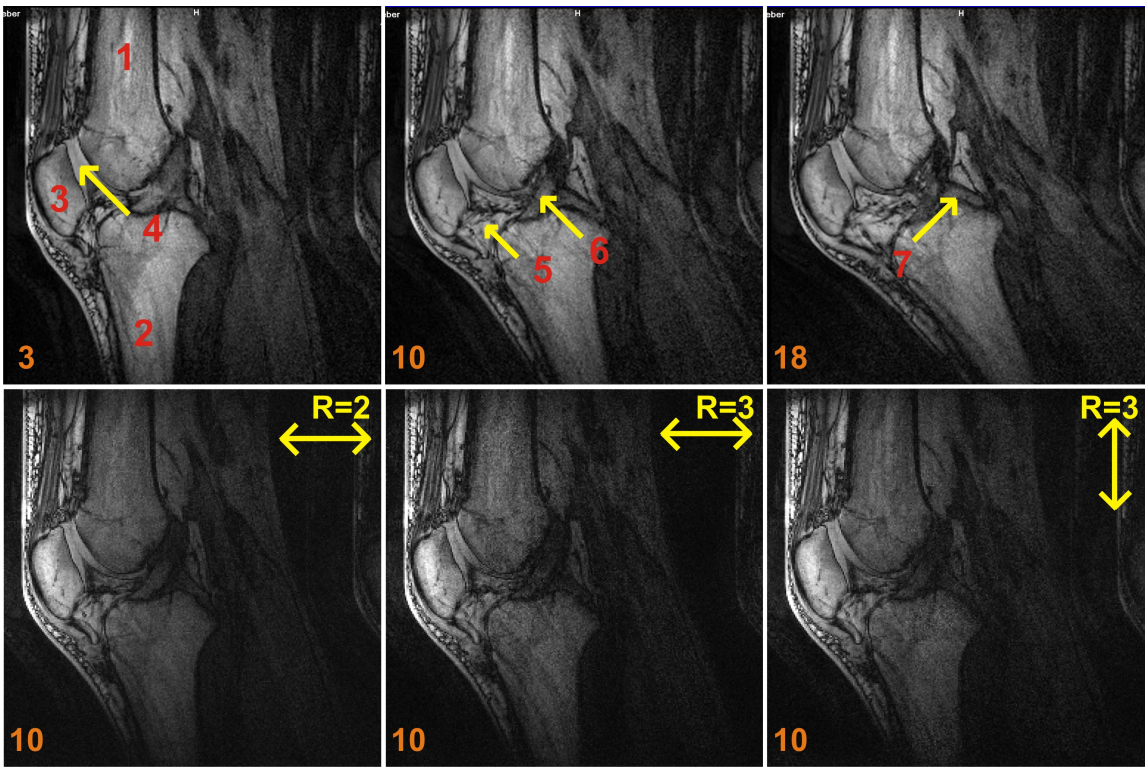

Figure 4.9: ***Snapshots enlarged and accelerated images:*** *A few of the snapshots, enlarged, revealing structures (1 - femur, 2 - tibia, 3 - patella, 4 - articular cartilage, 5 - intrapatellar fat pad, 6 - anterior cruciate ligament, 7 - posterior cruciate ligament) at a temporal resolution of 160 ms are shown in the top row. The bottom row shows 2 fold, 3 fold and 4 fold accelerated images of frame 10 reconstructed using GRAPPA, in A-P direction.*

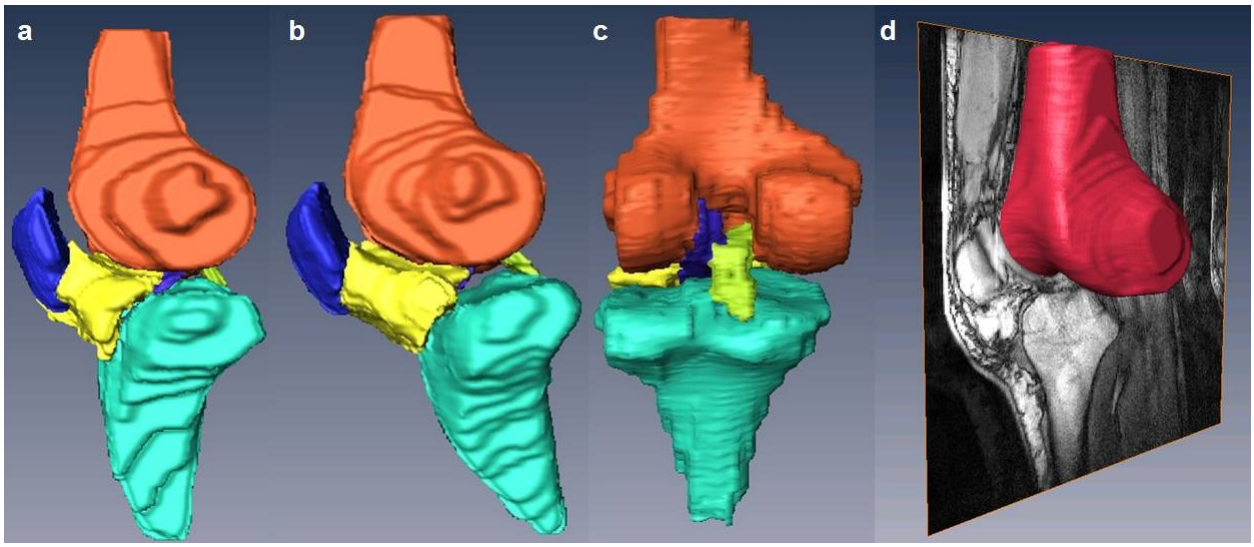

Figure 4.10: ***3D segmentations of the dynamic images at different positions:*** *While a, b and c are from a dataset that was acquired with a normal segmented flash (slice thickness of 5 mm), d was acquired with the described interleaved acquisition scheme (slice thickness of 2.5 mm) at a better spatial resolution, but with the same total acquisition time.*

also perfectly repeatable. The device also provides sufficient space for the construction of an RF array for dynamic imaging.

The constructed RF array does not affect the B_1^+ field as they are well decoupled during transmission. Multiple cable traps in every RF line and preamplifier decoupling ensure that a good isolation is obtained between the receive elements. The SNR reconstruction shows reasonable sensitivity at the region of interest. While in principle, it is possible to accelerate in all 3 directions, acceleration is relevant only in Anterior-Posterior direction due to the geometry of the ROI and the type of acquisition scheme used in this application. This is because, the slices are aligned along the Left-Right direction and the Head-Feet direction is taken for frequency encoding. Nevertheless up to 3-fold acceleration is possible with a tolerable decrease in SNR.

The designed interleaved acquisition scheme has been optimized for acquiring dynamic data over a large number of slices and with a high spatial and temporal resolution, as has been demonstrated. However, any of these parameters can be traded to improve the other. This is explained with following equations.

In a standard segmented acquisition, the number of frames is defined by the following equation:

$$N_{frames} = \frac{T_{cycle}}{TR \cdot \frac{N_{phases}}{N_{segments}}} \tag{4.1}$$

where Tcycle is the time taken for one movement cycle, which depends on the size of the patient, size/weight of the lower leg and pressure applied in the pneumatic cylinder. With the interleaved slice scheme the number of slices becomes,

$$N_{slices} = \frac{N_{phases}}{N_{segments}} \tag{4.2}$$

and hence

$$N_{frames} = \frac{T_{cycle}}{TR \cdot N_{slices}} \tag{4.3}$$

The frame rate can be calculated as

$$fps = \frac{N_{frames}}{T_{cycle}} = \frac{Nsegments}{TR \cdot N_{phases}} \tag{4.4}$$

The total acquisition time T_{total} is given by

$$T_{total} = (T_{cycle} + \Delta T) \cdot N_{segments} \cdot N_{slices} = (T_{cycle} + \Delta T) \cdot N_{phases} \tag{4.5}$$

where ΔT is the time between the end of the acquisition and the next trigger pulse.
The main advantage with the described interleaved acquisition scheme is that a higher SNR can be achieved preserving the total acquisition time, unlike a standard segmented acquisition, where an increase in acquisition time is necessary to obtain a higher SNR. But as has been shown in the above equations, the degrees of freedom are low, as the parameters are interconnected.
In a standard segmented acquisition an increase in temporal resolution can be achieved by increasing the number of segments, with the number of slices remaining constant. The total acquisition time increases and the spatial resolution stays the same. With the interleaved slice scheme increasing the number of segments also results in a higher frame rate (see Eq. 4.4), but the number of slices decreases (Eq. 4.2). The total acquisition time and the in-plane resolution remain the same (Eq. 4.5).

4.5 Outlook

In this work, new hardware (in the form of an active movement device and an optimized RF array) and an acquisition scheme for improved dynamic imaging have been designed, characterized and presented. The constructed movement device represents the actual motion in reality, in a better way compared to quasi-static or quasi-dynamic techniques and its reproducibility gives a possibility to spread the acquisition over multiple movement cycles. The designed RF array is compatible with the movement device and is suitable for imaging the whole knee joint in motion. With a good SNR at the ROI, it also offers the

possibility to accelerate acquisitions in multiple directions. The interleaved acquisition scheme, along with the movement device and array, offers high temporal resolution for the application. The combination of the above can now be used to enhance the diagnosis of knee disorders and study joint mechanics *in vivo*.

As always, there is scope for improvement in the designed devices and sequence. The constructed movement device can be modified to load the patient's knee during the movement as in reality. The coil can be improved with further detachable elements in the top of the housing, based on patient's size. The sequences can be altered to include the demonstrated parallel imaging capabilities of the coil. The above actions are works in progress.

Chapter 5

SNR and Overlap

5.1 Introduction

The design of a coil array for a specific application should take into account a range of factors, as detailed in the chapters on the construction of array coils for minipig and human knees. Once an optimum design is arrived, the actual engineering of the coil would involve a series of steps, one of which is the decoupling of neighboring elements. A preferred method for decoupling neighboring elements is to overlap them. Compared to a shared conductor decoupling or capacitive decoupling, overlapping neighboring elements has advantages in that it offers better spatial coverage and ease in tune & match of elements. But an optimum 'critical' overlap is needed to ensure that the coupling between the neighboring elements is minimum. Minimum coupling in turn ensures that the SNR is not degraded due to a less than optimum overlap. While it may sound simple to achieve the 'critical' overlap, in reality even subtle changes in the dimension of the loops or in their position spoils the isolation between elements.

This brings forth the following questions:

- What if the overlap is not optimum?
- Will the noise from individual channels and their correlation increase?
- How is the SNR affected due to an off-optimum overlap?

- Are the changes consistent with load?

In this chapter, using a study involving two loops, the author tries to answer the above questions and convey the point, as to how crucial this seemingly 'simple' step is and how much the SNR of the two channel array can degrade due to changes in overlap, at different loads.

5.2 Materials and methods

Two sets of loops of size 68 x 86 mm^2 were etched in boards, with provisions for very fine adjustment in overlap, as shown in figure 5.1. The first set was tuned to 63.6 MHz (for the experiment at the field strength of 1.5 T) and the second set to 123.2 MHz (for the experiment at the field strength of 3 T). The loops were then matched to 50 Ω for their optimum overlaps with the isolation between neighboring loops $\geq$20 dB. The loops were actively decoupled during transmission using resonant tank circuits. Toroidal Baluns tuned to the respective frequencies were used to minimize shield currents and phase shifters were used to achieve preamplifier decoupling. Two bottles of mineral oil were used in one case of experiment whereas two bottles of saline water (3.75 g $NiSo_4.6H_2o$ + 5g NaCl per litre of H_2o) were used as loading phantoms for the other case of experiment.

A simple gradient echo sequence (TR 100 ms, TE 10 ms, Slice thickness of 5 mm and a Bandwidth of 100 Hz/pixel) was used to obtain the SNR. The same sequence was repeated with the RF transmit pulse suppressed to obtain the noise data. SNR was calculated using bootstrap statistics ([55]) and averaged over the entire phantom for comparisons.

5.3 Results

The unloaded and loaded Q factors of the loop, that give a measure of the loading with the phantom used are shown in table 5.1:

From the obtained values, it can be seen that the noise from the sample (i.e. the

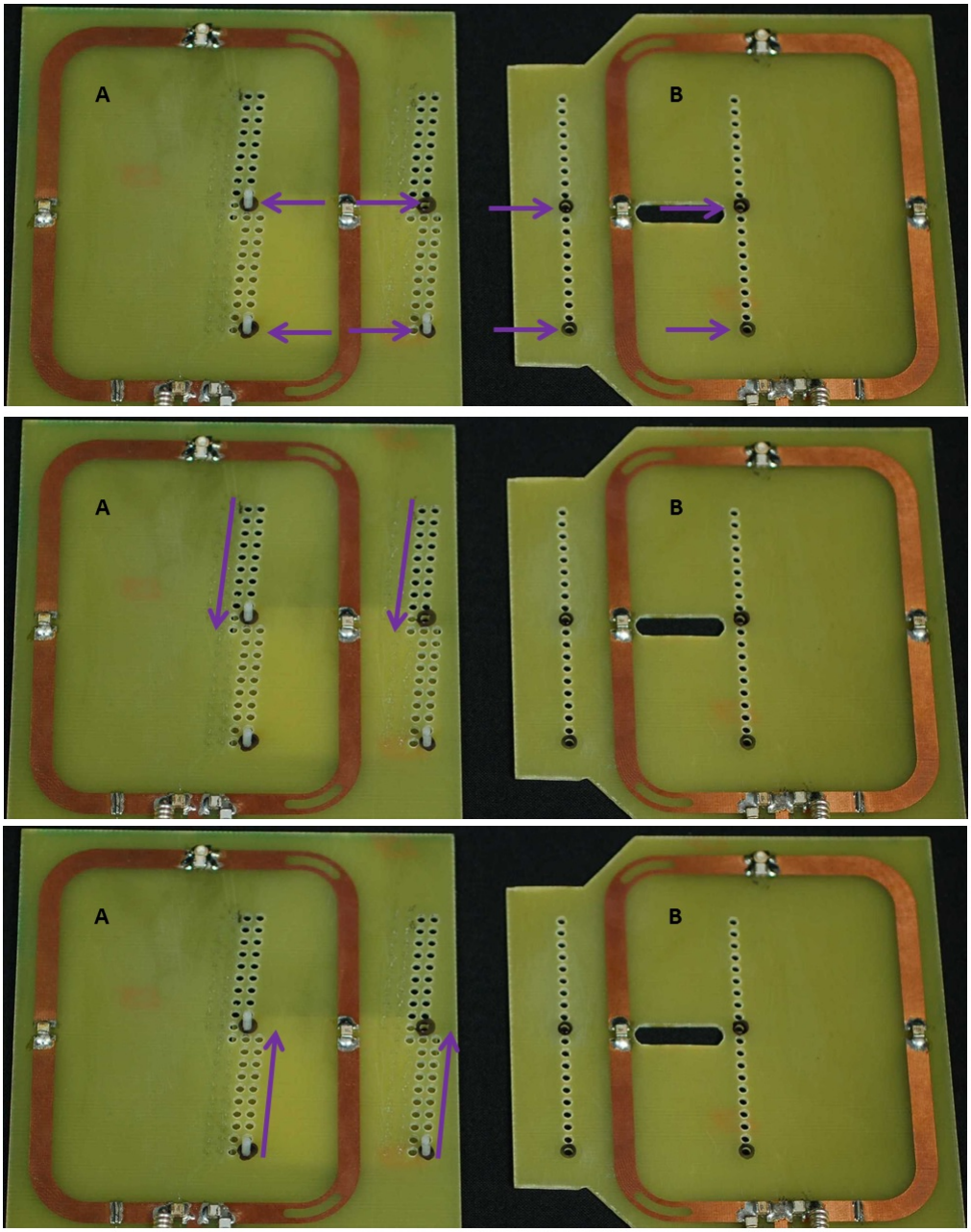

Figure 5.1: ***Rectangular loops used for the study:*** *Two loops of size 68 x 86 mm^2 were used for the study, with 4 capacitor breakpoints for tuning them to the required frequency. Optimum overlap is achieved when loop 'B' is positioned over loop 'A' at the points indicated by the arrow marks in the top figure. The middle figure shows the positions over which loop 'B' is moved over to obtain increasing overlaps. Each movement corresponds to 0.3 mm change in overlap. The bottom figure shows the decrease in overlap achieved.*

Frequency	Unloaded Q	Loaded Q	Q ratio
64 MHz	250	60	4.2
123 MHz	310	30	10.3

Table 5.1: ***Unloaded and loaded Q factors of the loops at the frequencies of operation***

phantom) is approximately 3 times higher than that of the noise obtained from the coil at 64 MHz and around 9 times higher at 123 MHz.

The change in noise levels of individual channels with overlap, obtained from the noise covariance matrices, for 64 and 123 MHz, when the setups were loaded with oil and saline phantoms are shown in figures 5.2 and 5.3.

As seen in the results, there is a large increase in the noise levels of channels with the change in overlap for the cases in which the setups were loaded with oil phantom (approximately 2 times). The change in noise levels for the case where the loops are loaded with saline solution at 64 MHz, also seems to be large. The setup in which the loops were loaded with saline solution at 123 MHz, had a relatively less change in noise levels with change in overlap. It needs to be mentioned here that even for the case of worst overlap, the reflection coefficient (S11) of the loops were better than -14 dB.

The noise correlations between the two channels show a similar trend, with the 123 MHz saline phantom setup showing only minor variations in correlation with changes in overlap, and the rest of the cases showing a larger variation. These are shown in figure 5.4.

The changes in SNR with changes in overlap for the 64 and 123 MHz cases with saline and oil phantoms are shown in figure 5.5. The SNR in these plots are normalized with respect to the optimum overlap case. It can be seen that the SNR changes by up to 25% for the 64 MHz oil phantom case, and around 15% for the 64 MHz saline phantom case. Compared to the above, the change in SNR for the 123 MHz water phantom setup is relatively less, at around 5%.

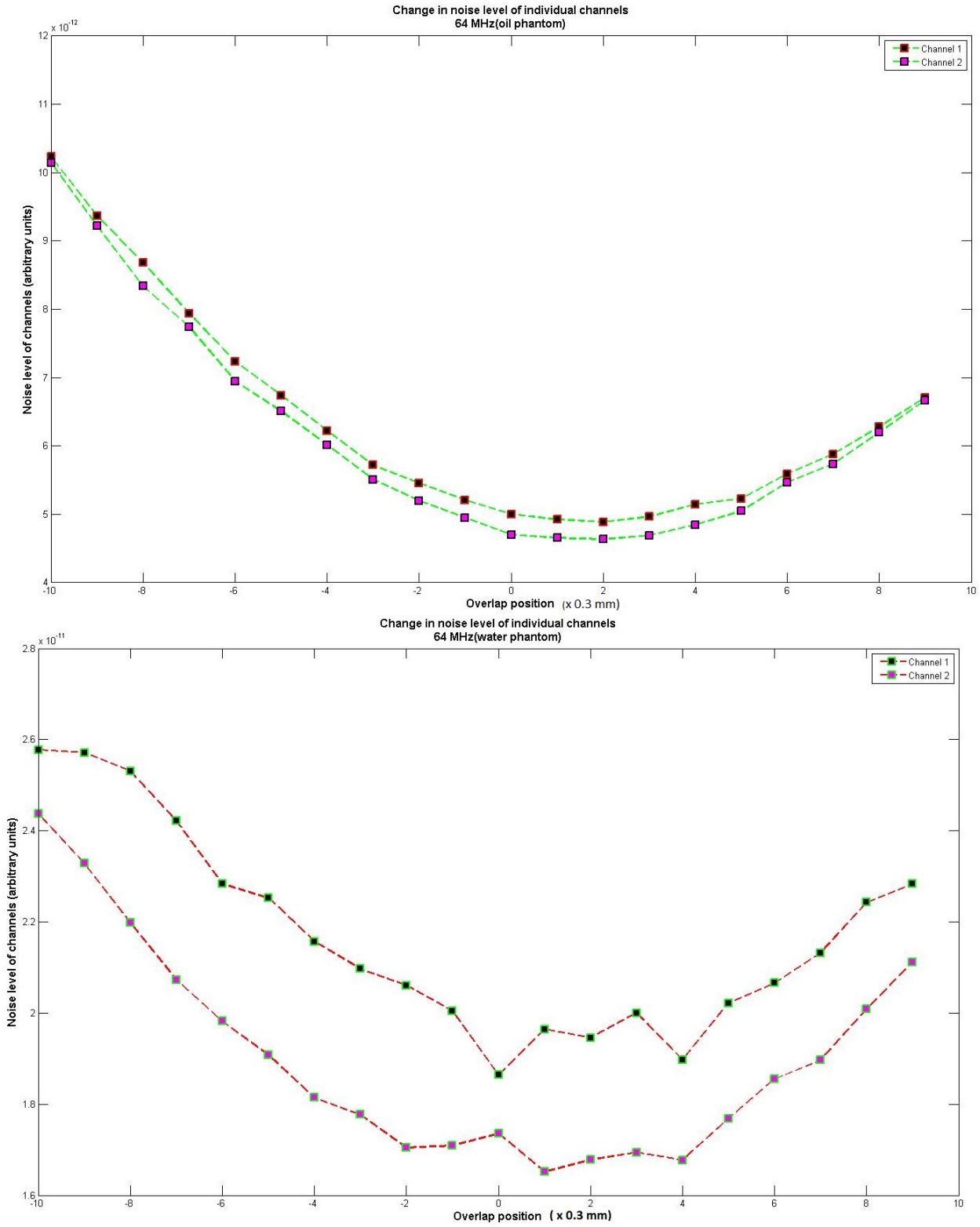

Figure 5.2: ***Change in the noise level of individual channels with the changes in overlap, for both oil and water phantoms, at 64 MHz.*** *The result shown in top figure is for the oil phantom and the result shown in bottom figure is when the loops were loaded with saline solution. Overlap position of 0 corresponds to optimum overlap with a unit change in overlap position corresponding to a movement of 0.3 mm in either of the directions.*

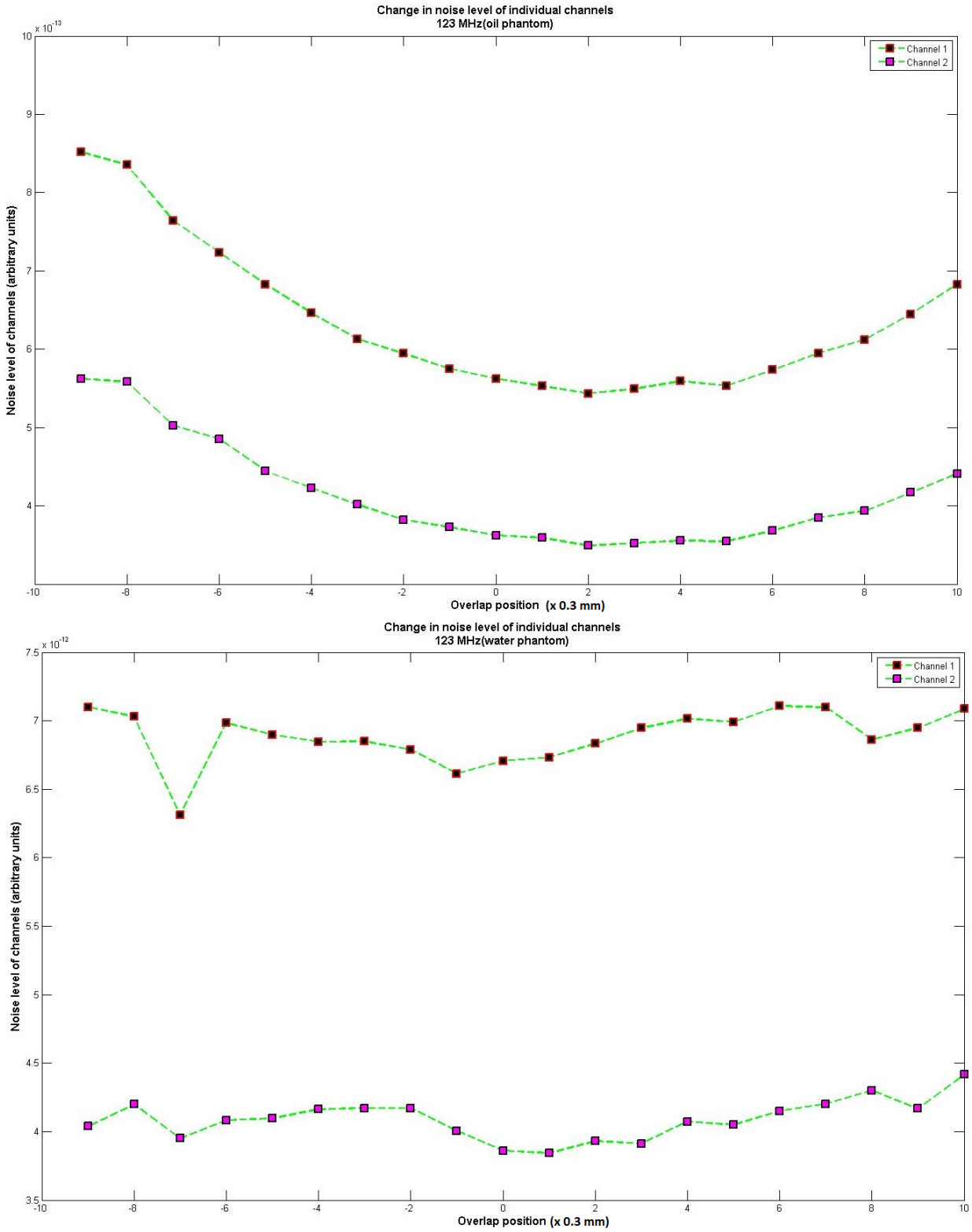

Figure 5.3: ***Change in the noise level of individual channels with the changes in overlap, for both oil and water phantoms, at 123 MHz.*** *The result shown in top figure is for the oil phantom and the result shown in bottom figure is when the loops were loaded with saline solution. Overlap position of 0 corresponds to optimum overlap with a unit change in overlap position corresponding to a movement of 0.3 mm in either of the directions.*

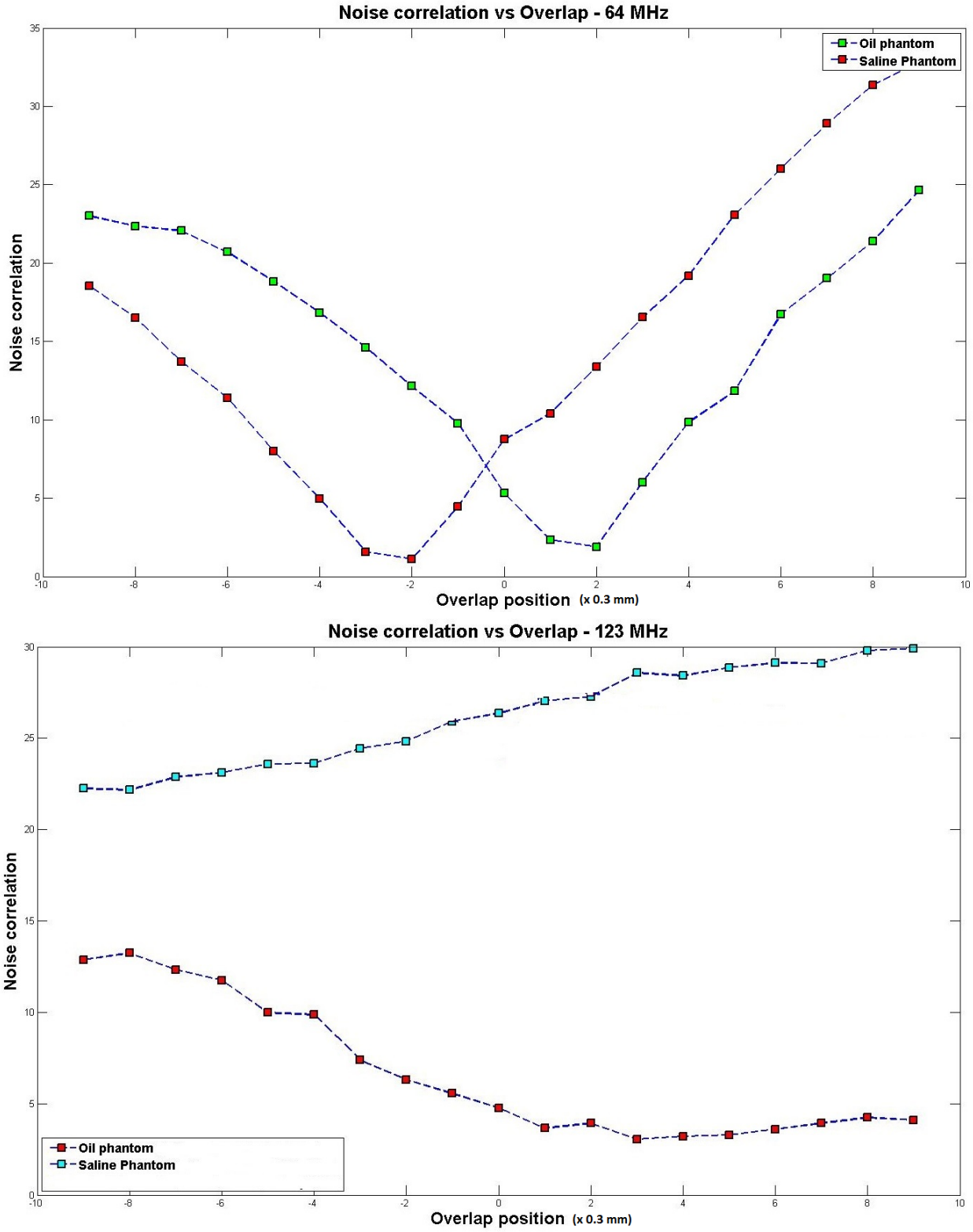

Figure 5.4: ***Change in the noise correlation between channels with changes in overlap, at 64 MHz (top) and 123 MHz (bottom)***. *As can be seen the change in noise correlation with overlap is large for both saline and oil phantoms at 64 MHz and also for the 123 MHz oil phantom setup. This is comparatively less for the 123 MHz water phantom setup.*

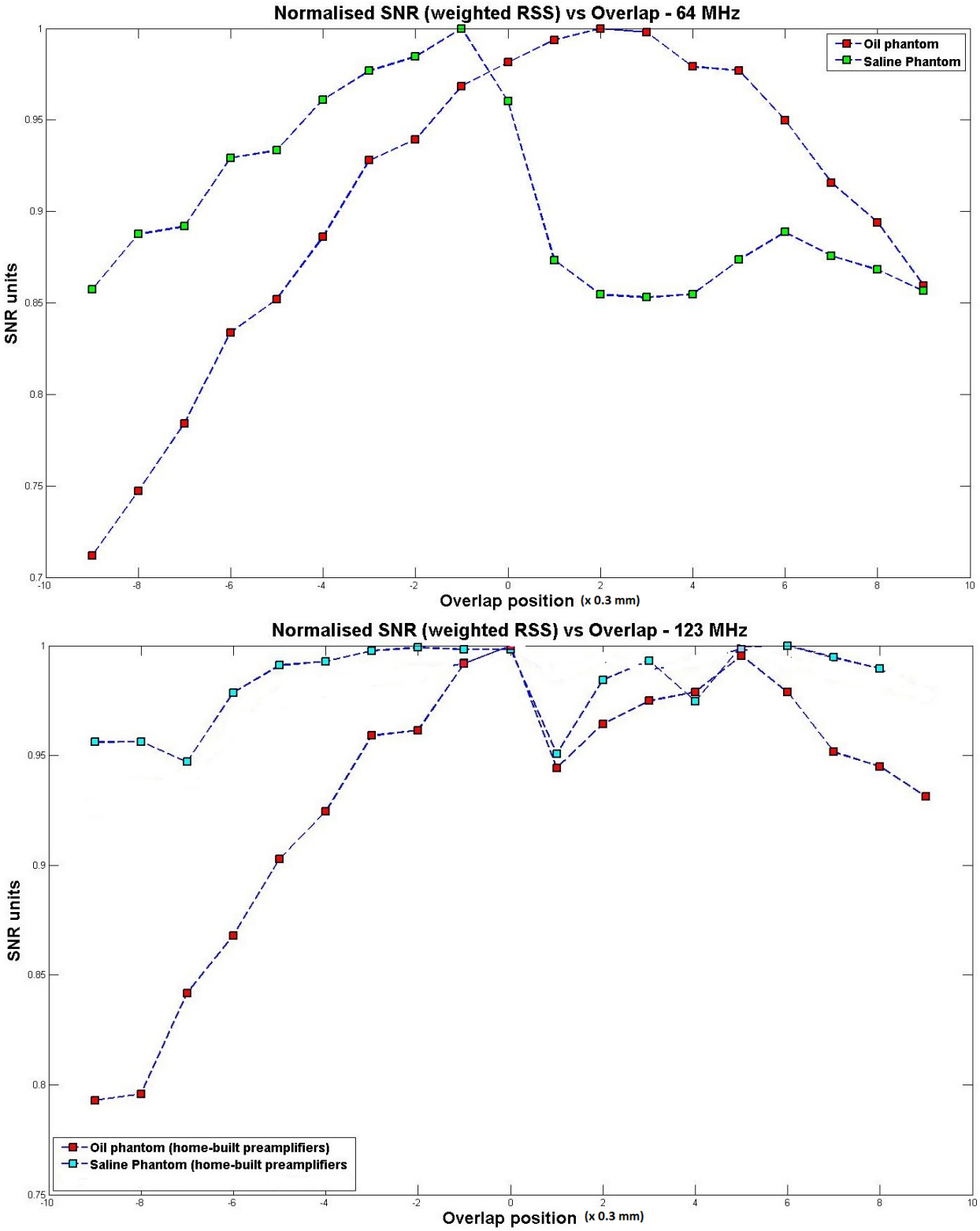

Figure 5.5: ***Change in normalized SNR with changes in overlap, at 64 MHz (top) and 123 MHz (bottom).*** *The change in SNR for the 123 MHz saline phantom is less when compared to the change in SNR in other cases.*

5.4 Discussion

Q ratio, defined as the ratio between the unloaded to loaded Q factors of a coil, is widely used as a measure to ascertain the load offered by an object or a phantom to a coil. The measure increases with increasing frequency, yielding a higher sensitivity as stated in equation 2.6. The results shown in this chapter enable us to understand this ratio and the change in SNR vis-a-vis overlap between neighboring elements.

The results shown are not elaborate to quantify the changes in any array. They rather allow us to understand the importance of overlap, especially in those coil configurations where there are constraints with regards to the element size decreasing the overall fill factor and hence Q ratio.

Figures 5.2, 5.3 and 5.4 show the stark rise in the individual noise levels of channels and the correlation between them with change in overlap. It should be noted that this rise is absent in the case of the loops tuned to 123 MHz, loaded with saline solution. Changes in overlap resulting in a higher coupling between the elements do not seem to affect the noise from the setup, which is highly sample noise dominated. The loop loaded by the highly conductive saline solution couples less with the neighboring loop and hence the noise between them is more uncorrelated. This translates into an SNR that varies less with subtle changes in overlap.

The increase in noise correlation and the corresponding decrease in SNR for those setups with a low Q ratio (typically < 4) means that care should be taken to ensure an optimum overlap, if the best SNR is to be achieved.

Chapter 6

A volume transmit coil for hand and a 12 channel receive array for wrist imaging at 7 T

6.1 Introduction

Rheumatoid arthritis (RA) and Osteoarthritis (OA) are two common diseases affecting adult hands. Patients with RA develop Synovialitis of several small joints in the metacarpus and in the wrist resulting in severe stiffness of their hands accompanied by erosive and destructive changes in the affected bones. With OA, the micro-anatomic basis of the disease, especially at its early stage is unclear [67]. It is still debated whether the initial changes take place in cartilage or bone or other articular tissues. Usually multiple joints throughout the hand (from wrist to distal finger joints) are affected in one disease or the other. In these disorders, it is crucial to detect early minute changes in cartilage and synovial tissue, before irreversible damage occurs.

While the role of MRI in the diagnosis of these diseases is well appreciated, sensitivity and specificity of diagnosis in the smaller joints of wrist and fingers are only moderate [68, 69]. Though MRI findings can be used to predict future damages of joints, standardization and validation are required to ensure accurate diagnosis, reproducibility and reliability

[70].

The above mentioned issues have prompted scientists and engineers to enhance our knowledge of these diseases and improve existing modalities of imaging. In this regard, ultra high field MR imaging of hand/wrist offers an exciting potential to improve diagnosis and our understanding of these maladies. The inherent increase in SNR at 7 T can be used to get images of very high spatial resolution and contrast to reveal fine anatomical details. A range of new hardware and techniques have been proposed [71–75] in this aspect. One such way to improve the SNR is to construct optimized RF coils/arrays.

At 7 T with the unavailability of a body transmit coil, transmit or transceive arrays are usually preferred. But the spatial resolution obtained with the above configurations is limited due to issues ranging from coupling of elements to low filling factor (with regards to hand imaging). Also as the size / wavelength is small for a human hand at the Larmor frequency of ^1H at 7 T (300 MHz), a parallel transmit solution is not necessary. It is proposed here that a single volume transmit coil with receive arrays optimized for different regions is a good solution for this application.

This configuration offers the following distinct advantages:

(i) Possibilities to use high-density receive arrays for reception. The small receive elements give a high quality factor drop, provide a sufficient penetration of sensitivity and offer the known capabilities to accelerate acquisitions.

(ii) Possibility to have receive arrays optimized for different regions in the hand, as a coil optimized to get high resolution images of one region within the hand (for e.g. wrist) cannot be expected to provide high resolution images of other regions (e.g. finger joints).

(iii) A homogeneous B1+ profile over the entire ROI and no issues of coupling among transmit elements.

The above configuration is implemented in this work by a 12 channel high-density RF receive array for wrist along with a volume transmit coil for hand imaging. The

constructed coils are electrically characterized; high resolution *in vivo* images, 'g' factor maps and Specific Absorption Rate (SAR) simulation results are presented.

6.2 Materials and Methods

Transmit coil At 7 T, distortions in transmit profile due to decreased wavelength and propagating waves are known. A uniform transmit profile, similar to the ones offered by birdcage coils at low frequencies, is still elusive in human heads and abdomen. But in the case of hand, these effects are less pronounced due to small electrical dimensions and low volume of conductive regions. Electromagnetic (EM) simulations with a birdcage at 300 MHz and an anatomical data set, showed that a nearly uniform transmit profile can be obtained throughout the hand (Results in next section). Hence it was decided to construct a birdcage as the transmit resonator.

A 24 leg band-pass shielded birdcage with an inner diameter of 180 mm and a length of 210 mm (Fig. 6.1) was constructed. To minimize radiation losses, the birdcage was completely shielded, using a striped copper sheet wound at a radial distance of 1 cm, away from the birdcage. Floating copper flanges were placed on both sides of the birdcage to further reduce radiation and to minimize the effect of electromagnetic fields on other circuitry within the coil. Both the shield and the resonator were etched from copper foils and glued to fiberglass cylinders of said dimensions. The high number of legs and the distance of the shield from the birdcage were chosen empirically to provide an increased tune capacitance (14 pF). This ensured minimum dielectric coupling to the sample and that the resonator is affected little by stray capacitance. With a 5 mm wide rectangular end ring, the individual rungs, which are of same thickness as rings, were interspersed with two capacitors of 42 pF each, to reduce their electrical length (approx. 1/5th of λ in air) and decrease dipole effects [76]. This value of rung capacitor was chosen to be high (relative to the ring capacitors) to have a high pass characteristic in the birdcage. PIN diodes in all legs actively decoupled the coil during reception. With its highest mode tuned to 297 MHz, the birdcage was quadrature driven using a hybrid coupler.

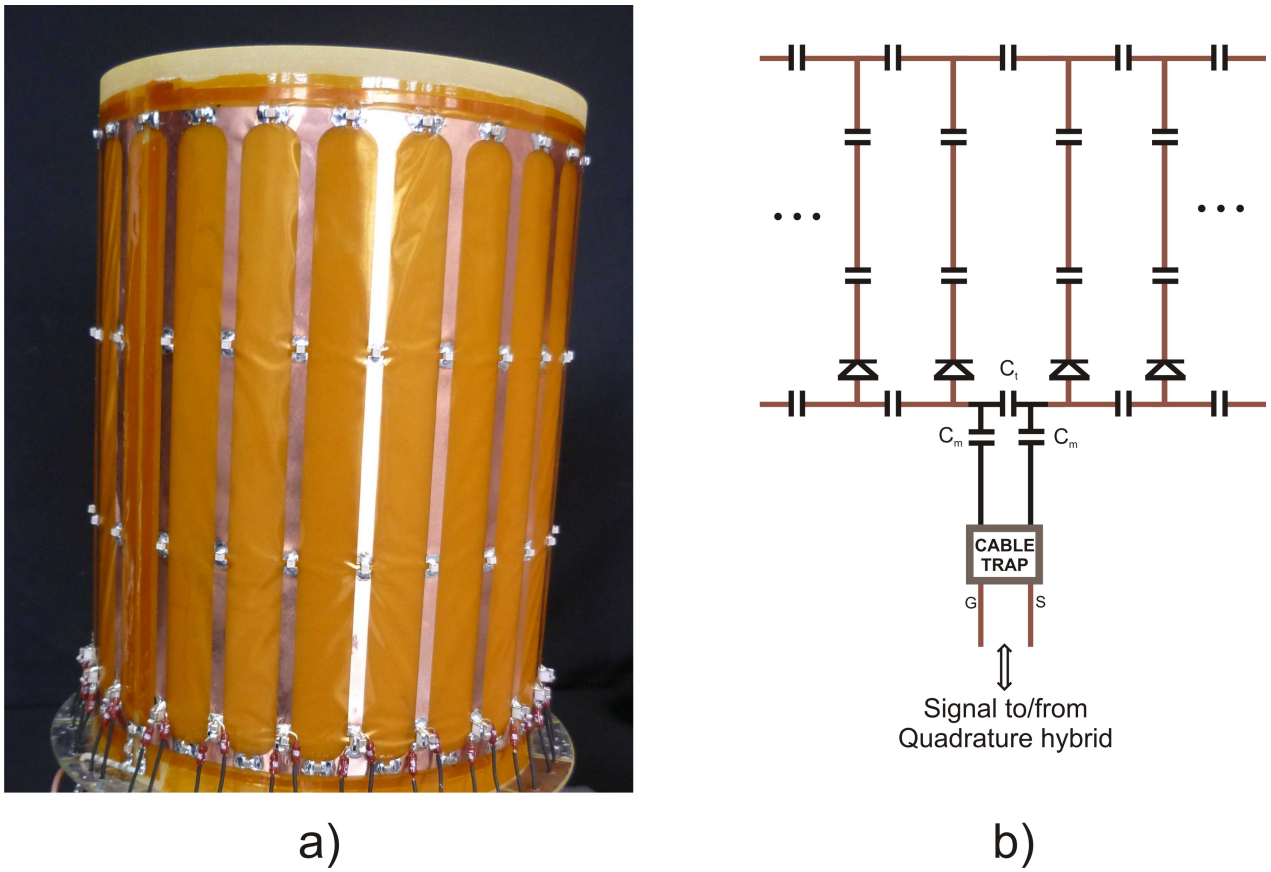

Figure 6.1: ***The Transmit coil.*** *a) Photograph of the band pass birdcage. The relatively high number of legs (24) helps in having a higher tune capacitance and in achieving a uniform B_1^+ field within the coil. b) C_m in both the signal and ground line form the matching circuit along with the tune capacitance C_t. Cable traps attached to both channels provide a symmetric feed. The capacitances in the legs reduce the electrical length while the PIN diodes actively decouple the birdcage. The DC lines for the PIN diodes are interspersed with HF blocking inductors at regular intervals and routed across the floating flange.*

The parallel match configuration (refer part 'b' of Fig.6.1) and cable traps ensured a symmetric feed. A preamplifier connected to the receive port of the hybrid enabled the use of the coil to obtain scout scans/localizers.

Receive array

Due to the large size of the transmit coil, the setup has to be used in 'superman' position, where a patient needs to stretch his/her arm over the head in Z axis. Prolonged duration of examinations in this posture causes an extreme stress to the patient in their upper arm. In the case of complete hand imaging, there is additional stress as a result of keeping the hand extended. If the region of interest is only wrist or/and metacarpals, patients can be allowed to fold in their fingers or keep it in a relaxed posture, so that the overall stress can be reduced (although only to a small extent). Hence, it was decided to have the coil elements distributed over a curved surface (Fig. 6.2) that can be placed over a patient's wrist/metacarpal region, leaving the fingers free to fold.

Considering the depth of the region of interest and possibilities of parallel acquisitions, twelve elements of size 35 x 35 mm^2 were distributed over a curved fiberglass plate of length 12 cm and breadth 13 cm (part 'b' in Fig.6.1), in 4 rows of 3 elements each. Neighboring elements were overlapped to minimize coupling between them, whereas the coupling between 'next-nearest' elements were reduced by connecting the elements to low input impedance Preamplifiers. The elements were actively decoupled during transmission and passive decoupling, along with fuses was incorporated as a safety measure (part 'e' in Fig.6.1). The Preamplifiers were placed in a separate housing. As the electrical length between the elements and the Preamplifiers was high (approx. 1/3rd of λ in air), multiple cable traps were placed in the RF lines, to reduce additional coupling between them. The same RF lines were used to convey the direct current for the PIN diodes used in active decoupling. Provisions in the form of a removable hand holder and a hand rest (parts 'c' and 'd' shown in Fig. 6.2) were designed to provide additional comfort to the patient's hand.

Workbench and MR measurements

The loaded and unloaded Q factors of the coil along with their decoupling were mea-

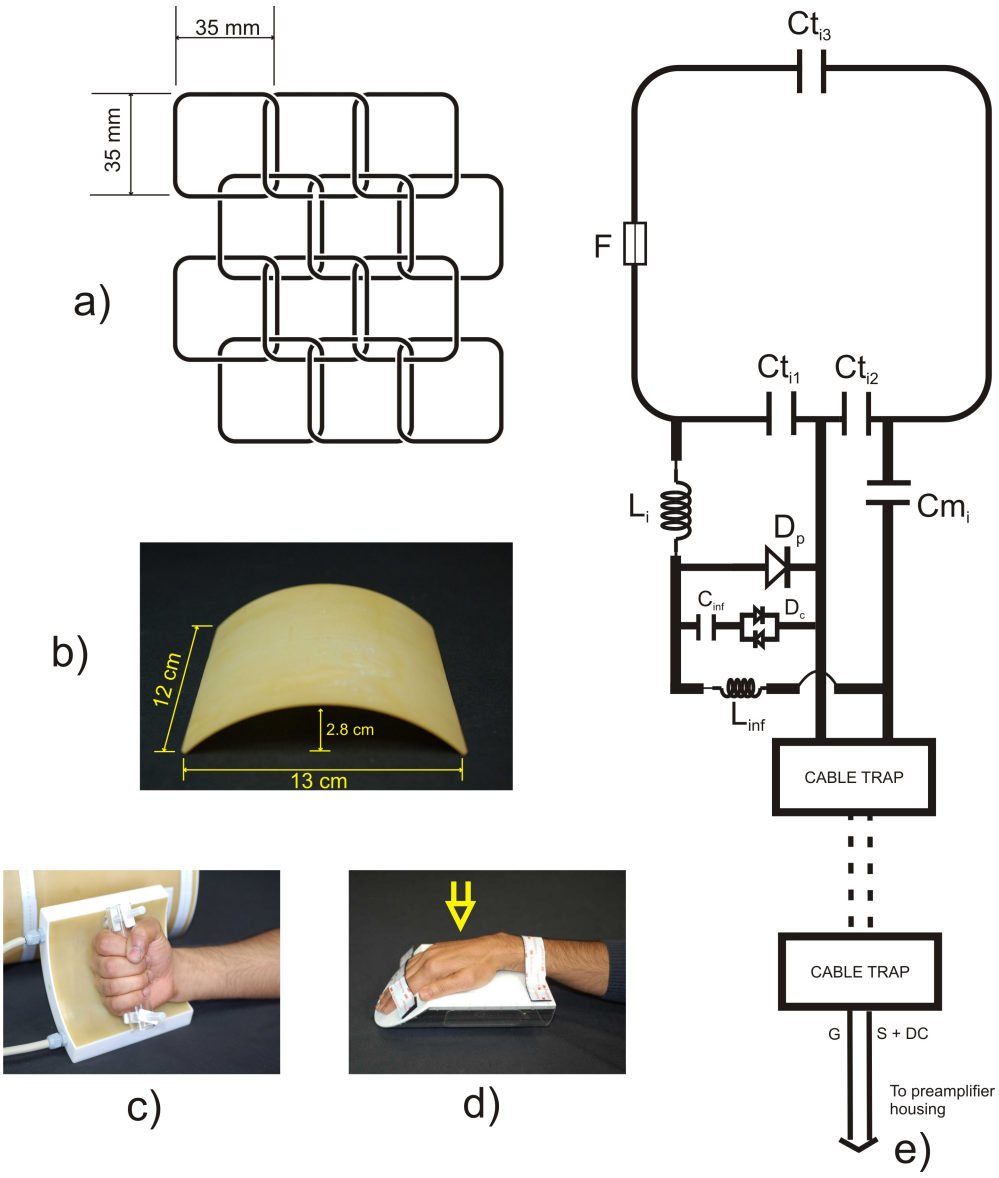

Figure 6.2: ***The Receive array.*** *Loops of size 35 × 35 mm^2 were distributed as shown in a) over a curved plate of dimensions 12 × 13 cm^2 shown in b). Provisions in the form of a hand holder (c) and hand rest (d) were designed so that patients can hold the receive array or rest their hand as per their convenience. The hand rest fits inside transmit coil and the receive array can be fixed above the patients hand, as marked. The coupling and active/passive decoupling circuits are shown in e). Multiple cable traps are incorporated per channel to reduce coupling over cables. The Fuse F and crossed diodes for passive decoupling (D_c) are included for added safety.*

sured in the same way as described in previous chapters. In order to make sure that it is possible to use other receive arrays in combination with the transmit coil, its resonance frequency and reflection (S11) were measured on the bench, with and without the receive array. Additionally the pulse calibration voltages in the scanner were also measured. Noise correlation between the receive elements were measured by taking a noise scan at the scanner (Magnetom 7T, Siemens Healthcare, Germany). A range of tests were performed on the coils, both on the bench and in the scanner to ensure that the coil functions as intended and that *in vivo* imaging on volunteers is safe. These tests included checking the B1+ homogeneity of the transmit resonator with and without the receive array, gradient induced eddy currents, active and passive decoupling of the receive array, and surface temperature under increased power transmissions. *In vivo* images were then acquired with a 2D FISP sequence (TR: 205 ms, TE: 6.21 ms, BW: 200 Hz/pixel, Slice thickness: 0.5 mm, FA: 64°, FOV: 120 x 120 mm2, Matrix size: 640 x 640, Acquisition time: 6:49 min), after obtaining written consent as per the regulations of the internal ethics committee. Both the hand holder and the hand rest were evaluated to assess the patient's decrease in stress caused by the 'superman' position. To evaluate the extent of parallel imaging possible with the receive array, turbo spin echo images (TR: 4.5 s, TE: 34 ms, FOV: 100 × 100 mm^2, Slice thickness: 1 mm, Turbo factor: 5, Matrix size: 512 x 512) were acquired on a cadaver hand. The GRAPPA [52] accelerated images and 'g' factor maps [56] were obtained from the k space data of the acquired images.

SAR simulation of the transmit coil

It is imperative to calculate the SAR of a transmit coil designed for an ultra high-field system to determine the hotspots (if any) and make sure that the transmitted power is restricted to confine them within the limits [77]. In this regard, electromagnetic simulations of the constructed transmit coil were done using a Finite Difference Time Domain solver (SEMCAD, Speag AG, Zurich, Switzerland) and anatomical model of a human hand (ITIS Foundation, Zurich, Switzerland). With a 2×2×2 mm^3 mesh enforced throughout the anatomical region, the simulation model had a total of 23×10^6 cells. The simulation was run for 3.4×10^6 time steps, checked for convergence and SAR values

were calculated as per IEEE averaging standards [78]. The calculated values were then incorporated in to the RF configuration settings of the scanner. Commercially available whole body clinical/research scanners take into account these entered SAR values. Along with the details of the power delivered/reflected from the transmit coil and the patient weight entered, the average power transmitted over a 6 min period is controlled by the scanner. If necessary, the scanners instruct the user to vary the repetition time (TR).

6.3 Results

The unloaded Q factor of the transmit birdcage coil was 250 and it decreased to 120, when loaded with a human hand. This low Q drop of 2.1 is due to the small dimensions of the hand (compared to the resonator size) and small volume of conductive regions. The elements in the receive array, on the other hand showed a Q drop of 7 (350 to 50), implying that the receive elements are highly sample noise dominated. The S11 at frequency of resonance of the transmit coil, 297.2 MHz, loaded with a tissue simulating phantom, measured through the transmit port of the quadrature hybrid, was -21.5 dB and this changed to -21.0 dB when the receive array was introduced. This showed that the resonance of the transmit coil was hardly affected with the addition of the receive array, hence avoiding the need to retune the transmit coil. It was found that the frequency of the homogeneous mode is isolated from other modes of the birdcage, by more than 50 MHz and hence there was no issue of mode coupling. The isolation between the channels of the quadrature transmit coil was -18 dB with a human hand as load. The active decoupling of the transmit coil was found to be 40 dB at the center of the birdcage, indicating that the birdcage is completely de-tuned with the PIN diodes during acquisition. The same measurement, for elements in the receive array, was found to be a minimum of 30 dB. The RF pulse angle calibration at the scanner is done by applying RF pulses of increasing amplitudes, till a 'null' is obtained at the center of the phantom and this amplitude is taken as the value for producing 180° flip angle [79]. This amplitude increased by 10 % upon inserting the receive array implying that there is a slight shielding of the

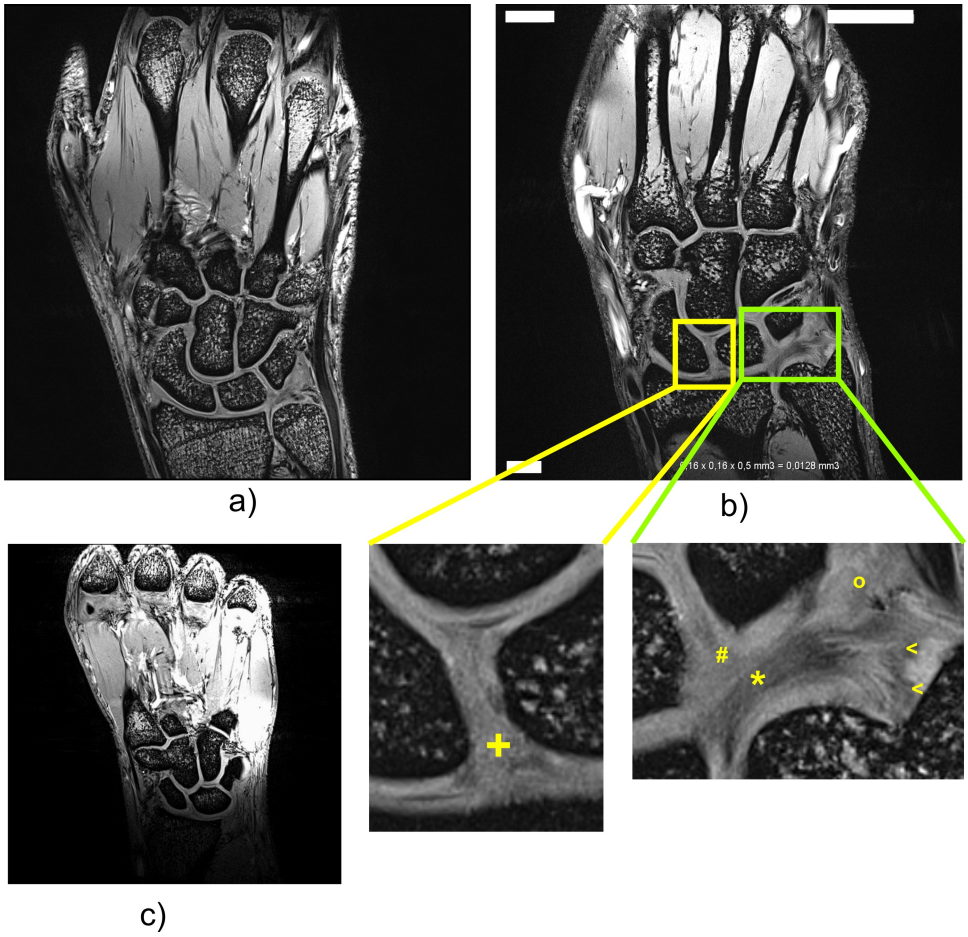

Figure 6.3: ***High resolution In vivo images.*** *a) A 2D FISP image acquired with a resolution of 0.19 x 0.19 x 0.5 mm^3, TR: 205 ms, TE: 6.21 ms, BW: 200 Hz/pixel, FA: 64 deg, Acquisition time: 6:49 min, shows the excellent contrast and spatial resolution obtained. b) An even higher spatial resolution of 0.16 x 0.16 x 0.5 mm^{3}s shows fine anatomical structures: Scapholunate ligament (+), Lunotriquetral ligament (#), triangular fibrocartillage (*), Ulnomeniscal homologue (○), Proximal and distal lamina (¡). c) Use of the hand holder provided a slight additional comfort to the patient, but caused motion artefacts in some patients, as the fingers are not mechanically fixed.*

B1+ produced by the coil, due to the array. The noise correlation measurements of the receive array done at the scanner showed a maximum correlation of 23 % and an average correlation of just 9 %, when the coil was loaded with an oil phantom. The average correlation increased to 21 %, when loaded with a human hand.

The high SNR obtained at the region of interest, is clearly apparent in the image obtained (Fig.6.3) in a resolution of 0.16 x 0.16 x 0.6 mm^3 revealing fine anatomical details as shown. This image was obtained by positioning the hand in a cushion and placing the receive array above the patient's hand. The use of the designed hand holder

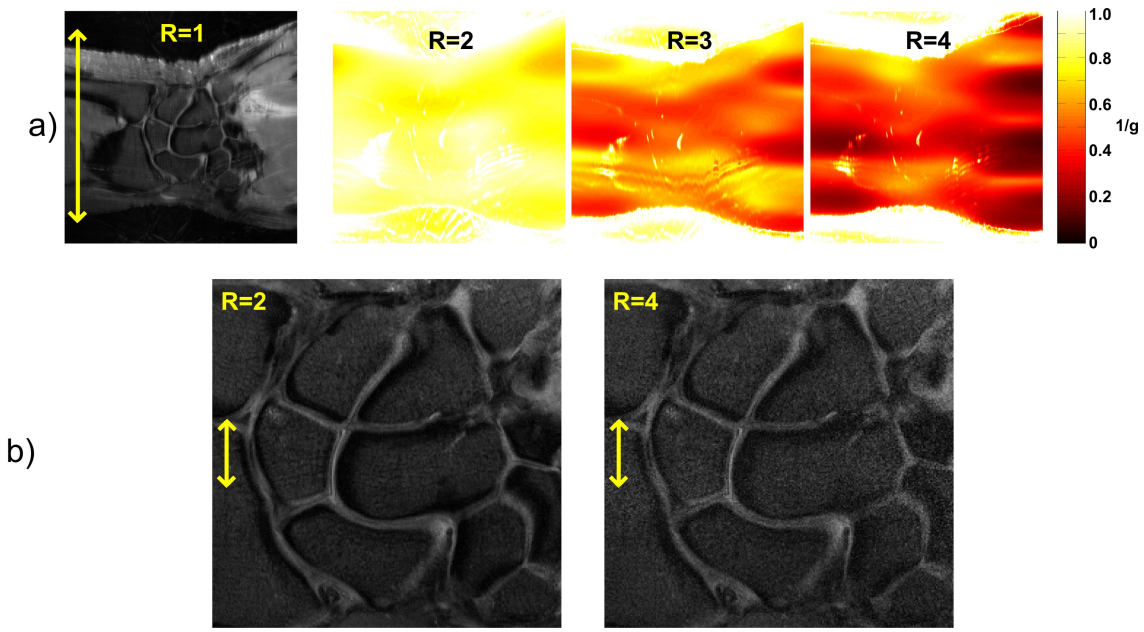

Figure 6.4: ***GRAPPA accelerated images and 1/g maps of a cadaver hand.*** *'a' shows the non-accelerated image (R=1, obtained with Turbo spin echo with turbo factor 5, TR: 4.5 s, TE: 34 ms, FOV: 100 x 100 mm2, Slice thickness: 1 mm, matrix size: 512 x 512) and 1/g maps with a 2-fold (R=2), 3-fold (R=3), and 4-fold (R=4) acceleration in the left-right direction. 'b' shows the reconstructed images for R=2 and R=4, zoomed in the ROI. For the reconstruction, 64 out of 512 lines were used as calibration lines. A similar acceleration is also possible in H-F direction, but is irrelevant to this application.*

provided a little comfort for the patient's hand. But in some cases, it also resulted in movement artifacts and inhomogeneous B_1^- sensitivity profile (as some parts of the coil are held closer to the hand than the rest), as shown in of figure 6.3.

Figure 6.4 shows the turbo spin echo images, non-accelerated and with 2-fold and 4-fold accelerations, reconstructed with GRAPPA, along with the GRAPPA '1/g' maps. While the decrease in SNR with R=2 and R=3 can be tolerated, R=4 causes a significant decrease in SNR.

Results of the EM simulations (Fig.6.5) show the B_1^+ and SAR distribution over the hand with distinct hotspots between the knuckle joints and in the wrist joint. The peak local SAR averaged over 10 g cubes turned out to be 4.33 W/kg. Hence on transmission of an average power of 4.6 W, the local SAR limits imposed by [77] were reached.

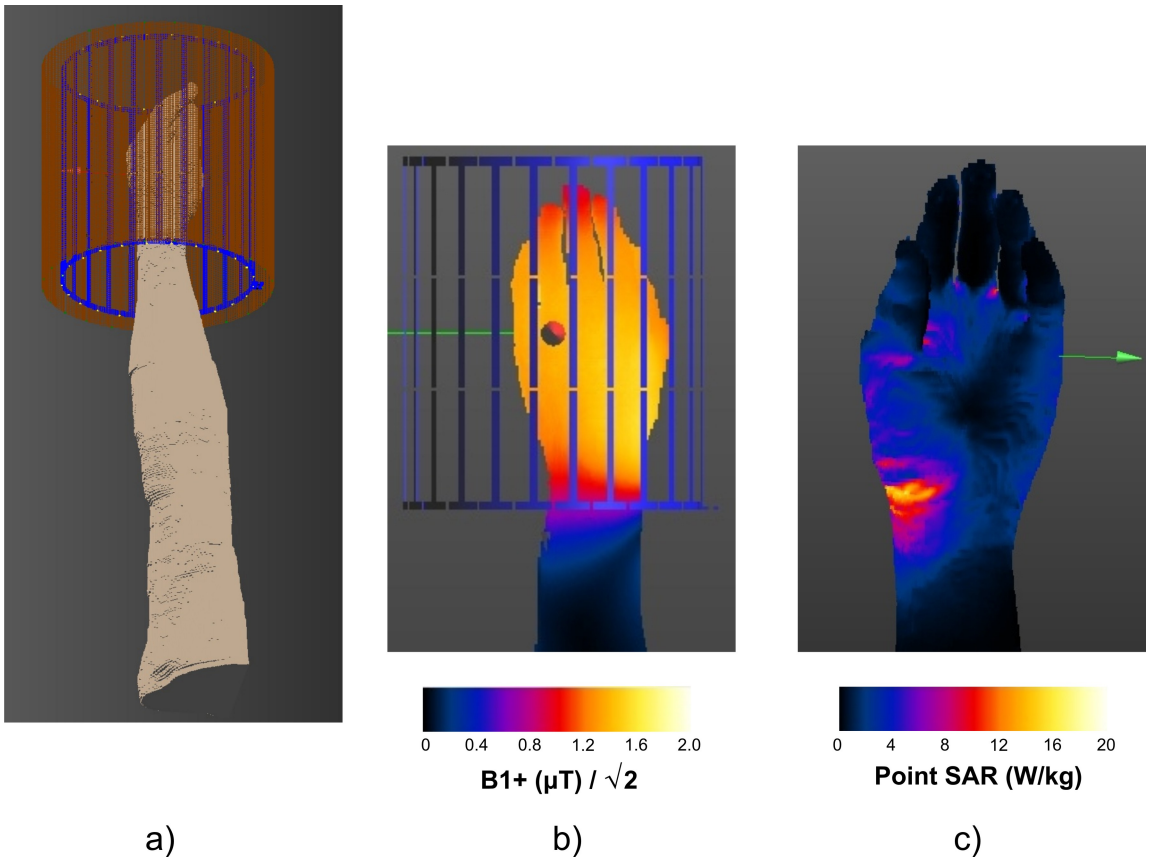

Figure 6.5: ***EM simulation model and results:*** *The FDTD simulation model of the transmit coil, along with its shield and the anatomical model of the arm is shown in 'a'. Only the shown length of the arm until the shoulders was used in simulation. The* B_1^+ *(transmit field) profile in 'b' shows that a near uniform distribution of the field is possible throughout the hand. The characteristic decrease of field near the end rings of the birdcage is also seen. 'c' shows the point SAR distribution with distinct hotspots at the junction of fingers and at the wrist due to the converging currents.*

6.4 Discussion

The obtained results show that birdcage coils can be effectively used as transmit coils for hand imaging at 7 T. Smaller dimensions and low volume of conductive regions of hand (as bones constitute a major portion) produce a low Q drop in the transmit coil. This can be improved by constructing close-fitting elliptical birdcages, but the circular birdcage with the above described diameter was preferred to allow flexible positioning of the hand, the use of hand-holder and other receive arrays. The large diameter along with a high number of legs also produces a uniform B_1^+ over a large region. The dimensions of the resonator with respect to hand and low Q drop also make the resonator less delicate and less susceptible to loads of varying dimensions. As shown the frequency response of the resonator is not affected by the presence of the receive array. Hence the constructed receive array is removable and in principle it is possible to use other receive arrays in combination with the same transmit resonator. Apart from the above, the following aspects of the constructed birdcage contributed in making it stable, with sufficient decoupling between the channels and minimum radiation losses.

(i) A relatively high tune capacitance (reduced influence of stray capacitance to the coil);

(ii) Use of PIN diodes in all legs to decouple the transmit coil;

(iii) Reduction of electrical length of the legs using intermittent capacitors;

(iv) Symmetric feeds with 'parallel' matching and the use of baluns;

(v) Intermittent blocking inductors in the DC lines (every 1/10th of wavelength in air);

(vi) Complete shielding (An unshielded birdcage of the same dimensions produced a poor unloaded Q factor that is 1/10th of the obtained value);

For the designed coil configuration, the Q drop of the receive array is more relevant then the Q drop of the transmit coil in terms of sensitivity and SNR. The designed high density array shows a good Q drop with the high sensitivity and excellent contrast

apparent from the images shown in Fig.3. Overlapping elements, preamplifier decoupling and multiple cable traps per channel have all contributed to the low average correlation observed between channels, at this frequency. The correlation values are much less than the generally accepted limit of 40 %, above which strong artifacts are observed in B_1^- profile. The dimensions are sufficient to cover the whole wrist and metacarpus of even large hands. While the sensitivity is homogeneous in head-feet direction, there is a decrease observed in the anterior-posterior direction, as we move down the surface. This may be improved by having additional elements below the hand, but they were avoided for the following reasons.

(i) Strong coupling between the top and bottom set of elements would have caused an inhomogeneous sensitivity distribution.

(ii) The amount of copper in the high density array in both the upper and lower sets would have shielded the transmit field to a relatively large extent.

As evident from the obtained 1/g maps and the shown accelerated images, a 3-fold acceleration in Left-Right direction is possible without any significant reduction in SNR. A similar parallel acquisition is also possible in the Head-Feet direction, but is irrelevant for imaging the wrist and metacarpus, as there are structures outside the FOV on either side. The accelerations can be effectively optimized and utilized to decrease the time of clinical examinations of hand/wrist, that stress the patient, due to uncomfortable positions. The simulation results show the extent of homogeneity obtained with the transmit field. The distinct SAR hotspots observed at the joints of fingers and wrist are due to currents (induced) converging from fingers along with the lack of high conductive regions like muscles and blood vessels. Compared to similar coils at lower field strengths, this is a large restriction. While this can be mitigated using parallel transmission techniques in a transmit array, the homogeneous B_1^+ field (such as by the constructed coil) cannot be achieved. Simulations done with only hand and with entire arm as load did not cause any significant change in the distribution or actual values of SAR. The hand holder was designed to allow patients to have different positions of hand in the coil to reduce

stress caused by the 'superman' position. Patients can fold their hand and hold the array horizontally or can even turn their hand and hold it vertically within the transmit coil, based on their comfort. While the hand holder reduces the stress in the arm to a small extent, it has to be mentioned that the major amount of stress is the 'superman' position itself. In conclusion, a volume transmit coil for hand and a 12 channel receive array dedicated for wrist/metacarpal region has been constructed, which covers the main joints affected by RA. The coils have been electrically characterized and high resolution *in vivo* images have been presented along with 1/g maps and EM simulation results. Optional positioning aids have been designed to provide added comfort and to achieve proper fixation of the hand in the transmit coil. The constructed volume transmit coil and the high density receive array show promising results in obtaining high resolution MR images. It is hoped that this construction is a step in the direction of improving the existing hardware to get a better knowledge and understanding of Rheumatoid Arthritis and Osteoarthritis.

Summary

Magnetic Resonance Imaging at field strengths up to 3 T, has become a default diagnostic modality for a variety of disorders and injuries, due to multiple reasons ranging from its non-invasive nature to the possibility of obtaining high resolution images of internal organs and soft tissues. Despite tremendous advances, MR imaging of certain anatomical regions and applications present specific challenges to be overcome. One such application is MR Musculo-Skeletal Imaging. This work addresses a few difficult areas within MSK imaging from the hardware perspective, with coil solutions for dynamic imaging of knee and high field imaging of hand.

Starting with a brief introduction to MR physics, different types of RF coils are introduced in chapter 1, followed by sections on design of birdcage coils, phased arrays and their characterization in chapter 2. Measurements, calculations and simulations, done during the course of this work, have been added to this chapter to give a quantitative feel of the concepts explained.

Chapter 3 deals with the construction of a phased array receiver for dynamic imaging of knee of a large animal model, i.e. minipig, at 1.5 T. Starting with details on the various aspects of an application that need to be considered when an MR RF array is designed, the chapter details the complex geometry of the region of interest in a minipig and reasons that necessitate a high density array. The sizes of the individual elements that constitute the array have been arrived at by studying the ratio of unloaded to loaded Q factors and choosing a size that provides the best ratio but still maintains a uniform SNR throughout the movement of the knee. To have a minimum weight and to allow mechanical movement of the knee, the Preamplifiers were located in a separate

box. A movement device was constructed to achieve adjustable periodic movement of the knee of the anesthetized animal. The constructed array has been characterized for its SNR and compared with an existing product coil to show the improvement. The movement device was also characterized for its reproducibility. High resolution static images with anatomical details marked have been presented. The 1/g maps show the accelerations possible with the array. Snapshots of obtained dynamic images trace the cruciate ligaments through a cycle of movement of the animal's knee.

The hardware combination of a high density phased array and a movement device designed for a minipig's knee was used as a 'reference' and extended in chapter 4 for a human knee. In principle the challenges are similar for dynamic imaging of a human knee with regards to optimization of the elements, the associated electronics and the construction of the movement device. The size of the elements were optimized considering the field penetration / sensitivity required for the internal tissues. They were distributed around the curvature of the knee keeping in mind the acceleration required for dynamic imaging and the direction of the movement. The constructed movement device allows a periodic motion of the lower half of the leg, with the knee placed within the coil, enabling visualization of the tissues inside, while the leg is in motion. Imaging has been performed using dynamic interleaved acquisition sequence where higher effective TR and flip angles are achieved due to a combination of interleaving and segmentation of the sequence. The movement device has been characterized for its reproducibility while the SNR distribution of the constructed RF array has been compared with that of a commercially available standard 8 channel array. The results show the improvement in SNR and acceleration with the constructed geometry. High resolution static images, dynamic snapshots and the 3D segmentation of the obtained images prove the usefulness of the complete package provided in the design, for performing dynamic imaging at a clinically relevant field strength.

A simple study is performed in chapter 5 to understand the effects of changes in overlap for coil configurations with different loads and at different frequencies. The noise levels of individual channels and the correlation between them are plotted against subtle

changes in overlap, at 64 and 123 MHz. SNR for every overlap setup is also measured and plotted. Results show that achieving critical overlap is crucial to obtain the best possible SNR in those coil setups where the load offered by the sample is low.

Chapter 6 of the thesis work deals with coil design for high field imaging of hand and wrists at 7 T, with an aim to achieve ultra high resolution imaging. At this field strength due to the increase in dielectric effects and the resulting decrease in homogeneity, whole body transmit coils are impractical and this has led engineers to design local transmit coils, for specific anatomies. While transmit or transceive arrays are usually preferred, to mitigate SAR effects, the spatial resolution obtained is limited. It is shown that a solution to this, with regards to hand imaging, can be a single volume transmit coil, along with high density receive arrays optimized for different regions of the hand. The use of a phased array for reception provides an increased SNR / penetration under high resolution. A volume transmit coil could pose issues in homogeneity at 7 T, but the specific anatomy of hand and wrist, with comparatively less water content, limits dielectric effects to have homogeneous B_1^+ profile over the hand. To this effect, a bandpass birdcage and a 12 channel receive array are designed and characterized. Images of very high spatial resolution (0.16 x 0.16 x 0.16 mm^3) with internal tissues marked are presented. *In vivo* 1/g maps show that an acceleration of up to 3 is possible and the EM simulation results presented show the uniform field along with SAR hotspots in the hand. To reduce the stress created due to the 'superman' position of imaging, provisions in the form of a holder and a hand rest have been designed and presented. Factors that contributed to the stability of the presented design are also listed, which would help future designs of receive arrays at high field strengths.

In conclusion, the coils and related hardware presented in this thesis address the following two aspects of MSK imaging: Dynamic imaging of knee and High resolution imaging of hand / wrist. The presented hardware addresses specific challenges and provides solutions. It is hoped that these designs are steps in the direction of improving the existing coils to get a better knowledge and understanding of MSK diseases such as Rheumatoid Arthritis and Osteoarthritis. The hardware can aid our study of ligament

reconstruction and development. The high density array and transmit coil design for hand / wrist also demonstrates the benefits of the obtained SNR at 7 T while maintaining SAR within limits. This design is a contribution towards optimizing hardware at high field strength, to make it clinically acceptable and approved by regulatory bodies.

Zusammenfassung

Die Magnetresonanztomographie mit Feldstärken bis zu 3 T ist zu einer Standard- Diagnosemethode für eine Vielzahl von Erkrankungen und Verletzungen geworden. Das hat mehrere Gründe, angefangen von ihrer nicht-invasiven Natur bis hin zu ihrer Fähigkeit, hochaufgelöste Bilder von inneren Organen und Weichteilen zu erhalten. Trotz enormer Fortschritte stellt die MR-Bildgebung bestimmter anatomischer Regionen oder bei bestimmten Anwendungen und Fragestellungen eine besondere Herausforderung dar. Eine dieser Anwendungen ist die MR-Bildgebung am Muskuloskelettalen System (MSK). Die vorliegende Arbeit befasst sich mit einigen schwierigen Fragestellungen innerhalb der MSK-Bildgebung aus aus der Perspektive der Hardware-Entwicklung: mit Spulendesigns für die dynamische Bildgebung des Knies und mit MR-Bildgebung der Hand bei hohen Magentfeldern. Nach einer kurzen Einführung in die MR-Physik werden in Kapitel 1 dann verschiedene Typen von Hochfrequenz-Spulen (HF-Spulen) vorgestellt, gefolgt in Kapitel 2 mit Abhandlungen des Designs von Birdcage-Spulen, Phased Arrays und deren Charakterisierung. Außerdem enthält das Kapitel Messungen, Berechnungen und Simulationen, die im Rahmen dieser Arbeit durchgeführt wurden, um einen quantitativen Eindruck von den erläuterten Konzepten zu vermitteln.

Kapitel 3 befasst sich mit dem Aufbau eines Phased-Array-Empfängers für die dynamische Bildgebung des Knies an einem großen Tiermodell (Minipig) bei 1,5 T. Es werden detailliert verschiedene Aspekte erläutert, die bei der Konstruktion eines RF-Arrays berücksichtigt werden müssen. Des Weiteren beschreibt das Kapitel die komplexe Geometrie des Zielbereichs am Knie des Minipigs und die Gründe für ein Array mit vielen Spulenelementen. Die Größe der einzelnen Spulenelemente, aus denen sich das

Spulenarray zusammensetzt, wurden mit Hilfe des Verhältnis von beladenem zu unbeladenem Q- Faktor optimiert und letztendlich eine Größe gewählt, die das beste Verhältnis liefert und gleichzeitig ein einheitliches SNR während des gesamten Bewegungszykluses des Knies garantiert. Um das Gewicht des Spulenarrays zu minimieren und eine möglichst gute mechanische Bewegung des Knies zu ermöglichen, wurden die Vorverstärker in einer separaten Box untergebracht. Außerdem wurde eine Bewegungsapparatur konstruiert, um eine einstellbare periodische Bewegung des Knies des narkotisierten Tieres zu ermöglichen. Das so konstruierte Spulenarray wurde hinsichtlich ihres SNRs charakterisiert und mit einer bestehenden Produktspule verglichen. Die Reproduzierbarkeit der Bewegung des Knies mit Hilfe der Bewegungsapparatur wurde untersucht und demonstriert, außerdem werden hochaufgelöste statische Bilder mit anatomischen Details gezeigt. Die 1/g-Karten zeigen die mit diesem Spulenarray möglichen Beschleunigungsfaktoren. Statische Snapshots, erzeugt aus den dynamisch aufgenommenen Bildern, zeichnen die Kreuzbänder durch einen kompletten Bewegungszyklus des Knies des Tieres hindurch nach.

Die Hardwarekombination aus einem Phased-Array und einer Bewegungsapparatur für das Minipig-Knie wurde als "Referenz" verwendet und in Kapitel 4 auf ein menschliches Knie übertragen und erweitert. Im Prinzip sind die Herausforderungen für die dynamische Bildgebung eines menschlichen Knies in Bezug auf die Optimierung der Elemente, der zugehörigen Elektronik und der Konstruktion der Bewegungsapparatur ähnlich. Die Größe der Spulenelemente wurde unter Berücksichtigung der für das innere Gewebe des Knies erforderlichen Felderzeugung und Empfindlichkeit optimiert. Die Spulenelemente wurden um die Krümmung des Knies herum verteilt, wobei die für die dynamische Bildgebung erforderliche Beschleunigung der Bildgebung und die Richtung der Kniebewegung berücksichtigt wurden. Die konstruierte Bewegungsapparatur ermöglicht eine periodische Bewegung des Unterschenkels, wobei das Knie in der Spule platziert ist. Das ermöglicht die Darstellung des Gewebes im Knie, während das Bein in Bewegung ist. Für die Bildgebung wurde eine dynamische Aufnahmesequenz verwendet, bei der durch eine Kombination aus Verschachtelung und Segmentierung höhere effektive TR-Zeiten

und Flip-Winkel erreicht werden konnten. Die Bewegungsapparatur wurde bezüglich der Reproduzierbarkeit der Bewegung charakterisiert. Außerdem wurde die SNR-Verteilung des konstruierten Spulenarrays mit der eines handelsüblichen 8-Kanal-Arrays verglichen. Die Ergebnisse der Spule mit der optimierten Geometrie zeigen eine Verbesserung hinsichtlich von SNR und Beschleunigung. Hochaufgelöste statische Bilder, dynamische Snapshots und die 3D- Segmentierung der aufgenommenen Bilder belegen den Nutzen der Kombination aus optimierter Spule und Bewegungsapparatur für die dynamische Bildgebung des menschlichen Knies bei einer klinisch relevanten Feldstärke.

In Kapitel 5 wird untersucht, wie sich Änderungen im Überlapp der Spulenelemente bei unterschiedlichen Beladungen und bei verschiedenen Frequenzen auswirken. Das Rauschlevel der einzelnen Kanäle und die Korrelation zwischen ihnen werden bei 64 und 123 MHz gegen kleine Änderungen des Überlapps der Spulenelemente aufgetragen. Ebenfalls gemessen und dargestellt wird das SNR für verschiedene Überlappungs-Szenarien. Die Ergebnisse zeigen, dass es gerade bei Proben mit niedriger Beladung essentiell ist, einen ausreichenden Überlapp zwischen den Spulenelementen herzustellen, um das bestmögliche SNR für eine bestimmte Spulenanordnungen zu erreichen.

Kapitel 6 der Dissertation beschäftigt sich mit dem Spulendesign für die Darstellung von Hand und Handgelenk bei einer sehr hohen Feldstärke (7 T) mit dem Ziel, eine ultrahochaufgelöste Bildgebung zu ermöglichen. Bei dieser hohen Feldstärke sind Ganzkörper-Sendespulen aufgrund der Zunahme von dielektrischen Effekten und der daraus resultierenden Abnahme der Homogenität unbrauchbar, weshalb für solche Szenarien lokale Sendespulen für spezifische Anatomien entwickelt wurden. Um SAR-Effekt zu minimieren werden hier in der Regel Sende- und Empfangsarrays verwendet, wobei die erzielte räumliche Auflösung aber begrenzt ist. In dem Kapitel wird gezeigt, dass in Bezug auf die Bildgebung der Hand die Lösung eine einzelne Sende-Volumenspule in Kombination mit einem mehrkanaligen Empfangsarrays sein kann, welches für den jeweiligen Bereich der Hand optimiert ist. Die Verwendung eines Phased-Arrays für den Empfang sorgt für ein erhöhtes SNR bei gleichzeitig guter Eindringtiefe und hoher Auflösung. Volumen-Sendespulen können bei 7 T Probleme generell Probleme bezüglich der B+1-Homogenität

haben, aber die Anatomie von Hand bzw. Handgelenk bei vergleichsweise geringerem Wassergehalt begrenzen dielektrische Effekte. Für diesen Anwendungsfall wurden ein Bandpass-Birdcage und ein 12-Kanal-Empfangsarray entworfen, gebaut und charakterisiert. Damit wurden Bilder mit sehr hoher räumlicher Auflösung (0,16 x 0,16 x 0,16 mm^3) aufgenommen. In vivo 1/g-Karten zeigen, dass eine Beschleunigung von bis zu einem Faktor von 3 möglich ist, und die vorgestellten EM-Simulationsergebnisse zeigen ein homogenes Feld zusammen mit SAR-Hotspots in der Hand. Um die Belastungen zu reduzieren, die durch die "Superman"-Position während der Bildgebung verursacht werden, wurden Maßnahmen in Form eines Halters und einer Handauflage getroffen und präsentiert. Alle Faktoren, die zur Stabilität des vorgestellten Designs beigetragen haben und die beim künftigen Design von Empfangsarrays bei hohen Feldstärken helfen würden, wurden aufgeführt und diskutiert.

Zusammenfassend lässt sich sagen, dass die Spulen und die zugehörige Hardware, die in dieser Arbeit vorgestellt werden, die folgenden beiden Aspekte der MSK-Bildgebung behandeln: Dynamische Darstellung des Knies und hochaufgelöste Darstellung der Hand bzw. des Handgelenks. Die vorgestellte Hardware adressiert spezifische Herausforderungen und bietet dafür Lösungen. Es bleibt zu hoffen, dass die hier vorgestellten Entwürfe Schritte in Richtung von besseren Spulen darstellen, mit deren Hilfe ein besseres Verständnis von MSK-Erkrankungen wie Rheumatoide Arthritis und Osteoarthritis gewonnen werden kann. Die verbesserte Hardware kann bei der Untersuchung von Bändern helfen, bei deren Rekonstruktionen genauso wie bei deren Entwicklung. Das Empfangsarray- und Sendespulendesign für die Hand bzw. das Handgelenk erzielt Vorteile im SNR bei 7 T bei gleichzeitiger Einhaltung der SAR-Grenzwerte. Dieses Spulendesign liefert einen Beitrag zur Optimierung der Hardware bei hoher Feldstärke, der hoffentlich eine klinischer Akzeptanz und die Zulassung durch die Aufsichtsbehörden erleichtert.

Bibliography

[1] I. I. Rabi, S. Millman, P. Kusch, and J. R. Zacharias, "The molecular beam resonance method for measuring nuclear magnetic moments. the magnetic moments of $_3Li^6$, $_3Li^7$ and $_9F^{19}$," *Phys. Rev.*, vol. 55, pp. 526–535, Mar 1939.

[2] F. Bloch, "Nuclear induction," *Phys. Rev.*, vol. 70, pp. 460–474, Oct 1946.

[3] P. Lauterbur, "Image formation by induced local interactions examples employing nuclear magnetic resonance," *Nature*, vol. 242, pp. 190–191, Mar 1973.

[4] P. Mansfield, "Multi-planar image formation using nmr spin echoes," *Journal of Physics C Solid State Physics*, vol. 10, no. 3, p. L55, 1977.

[5] R. Damadian, "Tumor detection by nuclear magnetic resonance," *Science*, vol. 171, no. 3976, pp. 1151–1153, 1971.

[6] A. Kumar, D. Welti, and R. R. Ernst, "NMR fourier zeugmatography," *Journal of Magnetic Resonance*, vol. 18, no. 1, pp. 69 – 83, 1975.

[7] D. Twieg, "The k-trajectory formulation of the NMR imaging process with applications in analysis and synthesis of imaging methods," *Medical Physics*, vol. 10, no. 5, pp. 610–621, 1983.

[8] E. Haacke, R. Brown, M. Thompson, and R. Venkatesan, *Magnetic Resonance Imaging - Physical principles and sequence design.* Wiley-Liss, 1999.

[9] A. Haase, F. Odoj, M. Von Kienlin, J. Warnking, F. Fidler, A. Weisser, M. Nittka, E. Rommel, T. Lanz, B. Kalusche, and M. Griswold, "Nmr probeheads for in vivo applications," *Concepts in Magnetic Resonance*, vol. 12, no. 6, pp. 361–388, 2000.

[10] P. Roemer, W. Edelstein, C. Hayes, S. Souza, and O. Mueller, "The nmr phased array," *Magnetic Resonance in Medicine*, vol. 16, no. 2, pp. 192–225, 1990.

[11] M. Henkelman, "Measurement of signal intensities in the presence of noise in mr images," *Medical Physics*, vol. 12, no. 2, pp. 232–233, 1985.

[12] C. D. Constantinides, E. Atalar, and E. R. McVeigh, "Signal-to-noise measurements in magnitude images from nmr phased arrays," *Magnetic Resonance in Medicine*, vol. 38, no. 5, pp. 852–857, 1997.

[13] J. De Wilde, J. Lunt, and K. Straughan, "Information in magnetic resonance images: evaluation of signal, noise and contrast," *Medical and Biological Engineering and Computing*, vol. 35, no. 3, pp. 259–265, 1997.

[14] P. M. Robson, A. K. Grant, A. J. Madhuranthakam, R. Lattanzi, D. K. Sodickson, and C. A. McKenzie, "Comprehensive quantification of signal-to-noise ratio and g-factor for image-based and k-space-based parallel imaging reconstructions," *Magnetic Resonance in Medicine*, vol. 60, no. 4, pp. 895–907, 2008.

[15] P. Kellman and E. R. McVeigh, "Image reconstruction in snr units: A general method for snr measurement†," *Magnetic Resonance in Medicine*, vol. 54, no. 6, pp. 1439–1447, 2005.

[16] O. Dietrich, J. G. Raya, S. B. Reeder, M. F. Reiser, and S. O. Schoenberg, "Measurement of signal-to-noise ratios in mr images: Influence of multichannel coils, parallel imaging, and reconstruction filters," *Journal of Magnetic Resonance Imaging*, vol. 26, no. 2, pp. 375–385, 2007.

[17] H. FUJITA, "New horizons in mr technology rf coil designs and trends," *Magnetic Resonance in Medical Sciences*, vol. 6, no. 1, pp. 29–42, 2007.

[18] X. Yang, T. Zheng, and H. Fujita, "Tr switches, baluns, and detuning elements in mri rf coils," in *Proceedings of the Weekend Educational course of the International Society of Magnetic Resonance in Medicine*, 2006.

[19] C. E. Hayes, W. A. Edelstein, J. F. Schenck, O. M. Mueller, and M. Eash, "An efficient, highly homogeneous radiofrequency coil for whole-body {NMR} imaging at 1.5 t," *Journal of Magnetic Resonance*, vol. 63, no. 3, pp. 622 – 628, 1985.

[20] J. Jin, *Electromagnetic analysis and design in Magnetic Resonance Imaging*. CRC Press LLC, 1999.

[21] U. S. D. of Health, *National ambulatory Medical Care Survey*, 1998.

[22] M. Gammons and E. Schwartz. (2011) Acl injury. [Online]. Available: http://emedicine.medscape.com/article/89442-overview

[23] M. Kessler, H. Behrend, S. Henz, G. Stutz, A. Rukavina, and M. Kuster, "Function, osteoarthritis and activity after acl-rupture 11 years follow-up results of conservative versus reconstructive treatment." *Knee Surgery, Sports Traumatology, Arthroscopy*, vol. 16, no. 5, pp. 442–448, 2008.

[24] R. A. van Dijck, D. B. Saris, J. W. Willems, and A. W. Fievez, "Additional surgery after anterior cruciate ligament reconstruction can we improve technical aspects of the initial procedure?" *Arthroscopy: The Journal of Arthroscopic and Related Surgery*, vol. 24, no. 1, pp. 88 – 95, 2008.

[25] N. Mohtadi, D. Chan, K. Dainty, and D. Whelan, "Patellar tendon versus hamstring tendon autograft for anterior cruciate ligament rupture in adults." *Cochrane Database of Systematic Reviews*, vol. 9, 2011.

[26] H. Liu, H. Fan, Y. Wang, S. L. Toh, and J. C. Goh, "The interaction between a combined knitted silk scaffold and microporous silk sponge with human mesenchymal stem cells for ligament tissue engineering," *Biomaterials*, vol. 29, no. 6, pp. 662 – 674, 2008.

[27] P. Vavken, S. Joshi, and M. M. Murray, "Triton-x is most effective among three decellularization agents for acl tissue engineering," *Journal of Orthopaedic Research*, vol. 27, no. 12, pp. 1612–1618, 2009.

[28] J. W. Freeman, M. D. Woods, D. A. Cromer, E. C. Ekwueme, T. Andric, E. A. Atiemo, C. H. Bijoux, and C. T. Laurencin, "Evaluation of a hydrogelâ€"fiber composite for {ACL} tissue engineering," *Journal of Biomechanics*, vol. 44, no. 4, pp. 694 – 699, 2011.

[29] S. Sahoo, H. Ouyang, C. James, H. Goh, T. E. Tay, and S. L. Toh, "Characterization of a novel polymeric scaffold for potential application in tendon/ligament tissue engineering," *Tissue Engineering*, vol. 12, no. 1, pp. 91–99, 2006.

[30] H. L. Koh, A. Kshirsagar, N. J. Herrod, T. A. Carpenter, L. D. Hall, E. B. Hunziker, and J. A. Tyler, "Visualization by magnetic resonance imaging of focal cartilage lesions in the excised mini-pig knee," *Journal of Orthopaedic Research*, vol. 14, no. 4, pp. 554–561, 1996.

[31] K.-Y. Lee, T. C. Dunn, L. S. Steinbach, E. Ozhinsky, M. D. Ries, and S. Majumdar, "Computer-aided quantification of focal cartilage lesions of osteoarthritic knee using {MRI}," *Magnetic Resonance Imaging*, vol. 22, no. 8, pp. 1105 – 1115, 2004.

[32] J. Petersen, P. Ueblacker, C. Goepfert, P. Adamietz, K. Baumbach, A. Stork, J. Rueger, R. Poertner, M. Amling, and N. Meenen, "Long term results after implantation of tissue engineered cartilage for the treatment of osteochondral lesions in a minipig model," *Journal of Materials Science: Materials in Medicine*, vol. 19, no. 5, pp. 2029–2038, 2008.

[33] K. Baumbach, J.-P. Petersen, P. Ueblacker, J. Schröder, C. Göpfert, A. Stork, J. Rueger, M. Amling, and N. Meenen, "The fate of osteochondral grafts after autologous osteochondral transplantation: a one-year follow-up study in a minipig model," *Archives of Orthopaedic and Trauma Surgery*, vol. 128, no. 11, pp. 1255–1263, 2008.

[34] M. Jung, B. Kaszap, A. Redöhl, E. Steck, S. Breusch, W. Richter, and T. Gotterbarm, "Enhanced early tissue regeneration after matrix-assisted autologous mesenchymal stem cell transplantation in full thickness chondral defects in a minipig model," *Cell Transplantation*, vol. 18, no. 8, pp. 923–932, 2009.

[35] A. M. Allen and F. S. Chew. (2011) Mri for anterior cruciate ligament injury. [Online]. Available: http://emedicine.medscape.com/article/400547-overview

[36] P. Colombet, D. Dejour, J.-C. Panisset, and R. Siebold, "Current concept of partial anterior cruciate ligament ruptures," *Orthopaedics and Traumatology, Surgery and Research*, vol. 96, no. 8, Supplement, pp. S109 – S118, 2010.

[37] C. E. Draper, J. M. Santos, L. C. Kourtis, T. F. Besier, M. Fredericson, G. S. Beaupre, G. E. Gold, and S. L. Delp, "Feasibility of using real-time mri to measure joint kinematics in 1.5t and open-bore 0.5t systems," *Journal of Magnetic Resonance Imaging*, vol. 28, no. 1, pp. 158–166, 2008.

[38] J. L. Dragoo, C. Phillips, J. D. Schmidt, S. F. Scanlan, K. Blazek, J. R. Steadman, and A. Williams, "Mechanics of the anterior interval of the knee using open dynamic {MRI}," *Clinical Biomechanics*, vol. 25, no. 5, pp. 433 – 437, 2010.

[39] L. Defrate, R. Papannagari, T. Gill, J. Moses, N. Pathare, and G. Li, "The 6 degrees of freedom kinematics of the knee after anterior cruciate ligament deficiency: an in vivo imaging analysis." *American Journal of Sports Medicine*, vol. 34, no. 8, pp. 1240–46, 2006.

[40] P. Johal, A. Williams, P. Wragg, D. Hunt, and W. Gedroyc, "Tibio-femoral movement in the living knee. a study of weight bearing and non-weight bearing knee kinematics using interventional MRI," *Journal of Biomechanics*, vol. 38, no. 2, pp. 269 – 276, 2005, knee Mechanics: An Update of Theoretical and Experimental Analyses.

[41] V. V. Patel, K. Hall, M. Ries, J. Lotz, E. Ozhinsky, C. Lindsey, Y. Lu, and S. Majumdar, "A three-dimensional mri analysis of knee kinematics," *Journal of Orthopaedic Research*, vol. 22, no. 2, pp. 283–292, 2004.

[42] V. V. Patel, K. Hall, M. Ries, C. Lindsey, E. Ozhiinsky, Y. Lu, and S. Majumdar, "Magnetic resonance imaging of patellofemoral kinematics with weight-bearing." *The*

journal of Bone and Joint surgery: American Volume, vol. 85-A, no. 12, pp. 2419–24, 2003.

[43] D. Witonski and B. Goraj, "Patellar motion analyzed by kinematic and dynamic axial magnetic resonance imaging in patients with anterior knee pain syndrome." *Archives of Orthopaedic and Trauma Surgery*, vol. 119, no. 1-2, pp. 46–9, 1999.

[44] P. J. Barrance, G. N. Williams, L. Snyder-Mackler, and T. S. Buchanan, "Altered knee kinematics in acl-deficient non-copers: A comparison using dynamic mri," *Journal of Orthopaedic Research*, vol. 24, no. 2, pp. 132–140, 2006.

[45] F. T. Sheehan, F. E. Zajac, and J. E. Drace, "Using cine phase contrast magnetic resonance imaging to non-invasively study in vivo knee dynamics," *Journal of Biomechanics*, vol. 31, no. 1, pp. 21 – 26, 1997.

[46] C. B. Ma, K. yang Lee, M. A. Schrumpf, and S. Majumdar, "Analysis of three-dimensional in vivo knee kinematics using dynamic magnetic resonance imaging," *Operative Techniques in Orthopaedics*, vol. 15, no. 1, pp. 57 – 63, 2005.

[47] G. Bode, P. Clausing, F. Gervais, J. Loegsted, J. Luft, V. Nogues, and J. Sims, "The utility of the minipig as an animal model in regulatory toxicology," *Journal of Pharmacological and Toxicological Methods*, vol. 62, no. 3, pp. 196 – 220, 2010.

[48] A. Zembsch, S. Trattnig, J. Walter, K.-H. Pölzl, and P. Ritschl, "Positioning device for optimal active kinematic real-time magnetic resonance imaging of the knee joint: a technical note," *Clinical Biomechanics*, vol. 13, pp. 308–313, 1998.

[49] V. Vedi, A. Williams, S. Tennant, E. Spuse, D. Hunt, and W. Gedroyc, "Meniscal movement: An invivo study using dynamic mri," *Journal of Bone and Joint surgery*, vol. 81, no. 1, pp. 37–41, 1999.

[50] F. Doty, G. E. Jr., C. D. Hauck, and J. P. Staab, "Practical aspects of birdcage coils," *Journal of Magnetic Resonance*, vol. 138, no. 1, pp. 144 – 154, 1999.

[51] C. Chen and D. Hoult, *Biomedical Magnetic Resonance Technology.* CRC-Press, 1989.

[52] M. A. Griswold, P. M. Jakob, R. M. Heidemann, M. Nittka, V. Jellus, J. Wang, B. Kiefer, and A. Haase, "Generalized autocalibrating partially parallel acquisitions (grappa)," *Magnetic Resonance in Medicine*, vol. 47, no. 6, pp. 1202–1210, 2002.

[53] K. P. Pruessmann, M. Weiger, M. B. Scheidegger, and P. Boesiger, "Sense: Sensitivity encoding for fast mri," *Magnetic Resonance in Medicine*, vol. 42, no. 5, pp. 952–962, 1999.

[54] G. C. Wiggins, J. R. Polimeni, A. Potthast, M. Schmitt, V. Alagappan, and L. L. Wald, "96-channel receive-only head coil for 3 tesla: Design optimization and evaluation," *Magnetic Resonance in Medicine*, vol. 62, no. 3, pp. 754–762, 2009.

[55] M. Riffe, K. Blaimer, M. Barkauskas, J. Duerk, and M. Griswold, "Snr estimation in fast dynamic imaging using bootstrapped statistics," in *Proceedings of the International Society of Magnetic Resonance in Medicine*, 2007.

[56] F. A. Breuer, S. A. Kannengiesser, M. Blaimer, N. Seiberlich, P. M. Jakob, and M. A. Griswold, "General formulation for quantitative g-factor calculation in grappa reconstructions," *Magnetic Resonance in Medicine*, vol. 62, no. 3, pp. 739–746, 2009.

[57] J. Taunton, M. Ryan, D. Clement, D. Mckenzie, D. Lloyd-Smith, and B. Zumbo, "A retrospective case-control analysis of 2002 running injuries," *British Journal of Sports Medicine*, vol. 36, pp. 95–101, 2002.

[58] S. Jacobs and B. Berson, "Injuries to runners: A study of entrrants to a 10,000 meter race," *The American Journal of Sports Medicine*, vol. 14, no. 2, pp. 151–155, 1986.

[59] F. Baarveld, C. Visser, B. Kollen, and F. Backx, "Sports related injuries in primary healthcare," *Family Practice*, vol. 28, no. 1, pp. 29–33, 2011.

[60] A. Arnason, A. Gudmundsson, H. Dahl, and E. Johannsson, "Soccer injuries in iceland," *Scandinavian journal of Mediciine and Science in Sports*, vol. 6, no. 1, pp. 40–45, 1996.

[61] W. Maletius and K. Messner, "Eighteen to twenty-four year follow-up after complete rupture of the anterior cruciate ligament." *American Journal of Sports Medicine*, vol. 27, no. 6, pp. 711–717, 1999.

[62] P. Hertel, H. Behrend, T. Cierpinski, V. Musahl, and G. Widjaja, "Acl reconstruction using bone-patellar tendon-bone press-fit fixation: 10-year clinical results," *Knee Surgery, Sports Traumatology, Arthroscopy*, vol. 13, no. 4, pp. 248–255, 2005.

[63] D. Daniel, M. Stone, B. Dobson, D. Fithian, D. Rossman, and K. Kaufman, "Fate of the acl injured patient. a prospective outcome study," *American Journal of Sports Medicine*, vol. 22, no. 5, pp. 632–44, 1994.

[64] T. Brune, A. Borel, T. Gilbert, J. Franceschi, S. Badylak, and P. Sommer, "In vitro comparison of human fibroblasts from intact and ruptured acl for use in tissue engineering," *European Cells and Materials*, vol. 14, pp. 78–90, 2007.

[65] S. Tennant, A. Williams, V. Vedi, C. Kinmont, W. Gedroyc, and D. Hunt, "Patello-femoral tracking in the weight-bearing knee: a study of asymptomatic volunteers utilising dynamic magnetic resonance imaging: a preliminary report." *Knee Surgery, Sports Traumatology, Arthroscopy*, vol. 9, no. 3, pp. 155–162, 2001.

[66] R. Bradford, K. Johnson, O. Wieben, and D. Thelen, "Dynamic imaging of 3d knee kinematics using pc-vipr." in *Proceedings of the 19th Annual meeting of International Society of Magnetic Resonance in Medicine*, 2011.

[67] A. L. Tan, A. J. Grainger, S. F. Tanner, D. M. Shelley, C. Pease, P. Emery, and D. McGonagle, "High-resolution magnetic resonance imaging for the assessment of hand osteoarthritis," *Arthritis and Rheumatism*, vol. 52, no. 8, pp. 2355–2365, 2005.

[68] F. Eckstein, D. Burstein, and T. M. Link, "Quantitative mri of cartilage and bone: degenerative changes in osteoarthritis," *NMR in Biomedicine*, vol. 19, no. 7, pp. 822–854, 2006.

[69] U. Dohn, B. Ejbjerg, M. Court-Payen, M. Hasselquist, E. Narvestad, M. Szkudlarek, J. Møller, H. , Thomsen, and M. Østergaard, "Are bone erosions detected by magnetic resonance imaging and ultrasonography true erosions? a comparison with computed tomography in rheumatoid arthritis metacarpophalangeal joints." *Arthritis Research and Therapy*, vol. 8, no. 4, 2006.

[70] J. Farrant, P. Connor, and A. Grainger, "Advanced imaging in rheumatoid arthritis," *Skeletal Radiology*, vol. 36, no. 4, pp. 269–279, 2007.

[71] J. NordmeyerMassner, N. DeZanche, and K. Pruessmann, "Mechanically adjustable coil array for wrist mri," *Magnetic Resonance in Medicine*, vol. 61, no. 2, pp. 429–438, 2009.

[72] J. A. NordmeyerMassner, M. Wyss, G. Andreisek, K. P. Pruessmann, and J. Hodler, "In vitro and in vivo comparison of wrist mr imaging at 3.0 and 7.0 tesla using a gradient echo sequence and identical eight-channel coil array designs," *Journal of Magnetic Resonance Imaging*, vol. 33, no. 3, pp. 661–667, 2011.

[73] G. Chang, K. M. Friedrich, L. Wang, R. L. Vieira, M. E. Schweitzer, M. P. Recht, G. C. Wiggins, and R. R. Regatte, "Mri of the wrist at 7 tesla using an eight channel array coil combined with parallel imaging: Preliminary results," *Journal of Magnetic Resonance Imaging*, vol. 31, no. 3, pp. 740–746, 2010.

[74] W. E. Kwok, Z. You, J. Monu, G. Seo, and C. Ritchlin, "High resolution uniform mr imaging of finger joints using a dedicated rf coil at 3t," *Journal of Magnetic Resonance Imaging*, vol. 31, no. 1, pp. 240–247, 2010.

[75] A. Iagnocco, C. Perella, M. D'Agostino, E. Sabatini, G. Valesini, and P. Conaghan, "Magnetic resonance and ultrasonography real-time fusion imaging of the hand and

wrist in osteoarthritis and rheumatoid arthritis," *Rheumatology Oxford*, vol. 50, no. 8, pp. 1409–13, 2011.

[76] M. Harpen, "Cylindrical coils near self resonance," *Magnetic Resonance in Medicine*, vol. 30, pp. 489–93, 1993.

[77] IEC, "Particular requirements for the basic safety and essential performance of magnetic resonance equipment for medical diagnosis," *IEC 60601-2-33 3rd Edition*, 2010.

[78] IEEE, "Recommended practice for measurement and computations of rf electromagnetic fields with respect to human exposure to such fields, 100 khz-300 ghz. annex. e peak spatial average sar," *IEEE standards C95.3*, 2003.

[79] N. G. Dowell and P. S. Tofts, "Fast, accurate, and precise mapping of the rf field in vivo using the 180° signal null," *Magnetic Resonance in Medicine*, vol. 58, no. 3, pp. 622–630, 2007.

Acknowledgements and Contributions

At first, I would like to acknowledge Prof. Peter Jakob and Fr. Ulrike Haase. Their support and mentorship towards myself and the whole department/organization, have had a great influence in improving my tech. understanding and shaping me as a person.

While its difficult to describe the positive effect the following people had in my life, I thank all of them from the bottom of my heart in refining me to what I am:

Dr. Titus Lanz and Dr. Daniel Haddad at RAPID Biomedical and MRB Forschungszentrum respectively, for giving me an opportunity to be in their great teams. I would have neither learnt the basics of my chosen domain nor would I have known how to use them to solve problems in applications.

A whole lot of people from RAPID Biomedical - Dr. Frank Resmer for teaching the fundamentals and putting up with my numerous tantrums, Michael Sauer for showing how a person needs to be calm despite sitting opposite to me for many years, Dr. Matthias Mueller for all the energy that he brought into the room, Markus Adriany for showing me how to be lively at all times, Tobias for all the discussions on coding and simulations, Nikola Endres on how to work with boards and Filip Tokic on the importance of mech. modelling - without you all and Aileen (for all the great food at your place), my work would have been quite lonely. It was so much fun sharing the room/dept. with you all.

and a whole lot of people from EP5/MRB - Dr. Daniel Weber for the constant support during the project Forzebra and later as well, Jo. Schrauth, Dr. Felix Breuer, Dr. Martin Blaimer, Dr. Daniel Gareis, Dr. Volker Behr, Dr. Marcos Lopez, Dr. Yuxiang

Ye, Dr. Uvo Hoelscher - all of them have helped me in numerous ways in enhancing my understanding of the subject and reviewing my work.

My life in Germany wouldn't have been complete without some of my friends in Wuerzburg and Aachen...Krishna, Janaki, Yuvraj, Gopi, Ram, Praveen, Mahesh, Imran and the 2 Anoops from God's own country, apart from my numerous Badminton mates. Thanks to the wonderful times fellas. Its not just that I had fun; I also learnt a lot from every one of them. Anoop - I'm defending my thesis :-)

At last, I would have been nowhere without the constant support of my parents and my entire family. You people didn't just bring me up: you are still doing it at this age. My whole hearted salute to them. The SreeSkand kids have made my life so loving: I'm looking forward to have fun with you my whole life.

While I'm indebted to Germany and Wuerzburg (in particular) in many ways, there is one aspect that truly stands out: Wuerzburg - the city where I met a girl (Aruna) who eventually became my better half. Her tireless work, motivation, patience and support is a never-ending source of inspiration to me.

There is a saying in my mother tongue-Tamil- about the region in India where I come from: 'Vandhaarai Vaazha vaikkum Tamizhagam', which means that who ever comes to the region TamilNadu (within India) with whatever they have, the region will make them live a good life. This saying is really true of Germany - the country that transformed me into the person I am.

Acknowledgement of the funding

This work and the studies involved were funded by the Bayerische Forschungsstiftung for Forschungsverbund für "Zellbasierte Regeneration des muskuloskelettalen Systems im Alter (ForZebRA)" under grant no. AZ-810-08 and RAPID Biomedical GmbH. (Rimpar, Germany).

Contributions

I formally acknowledge and thank the contribution of my fellow researchers from EP5, Joachim Schrauth and Daniel Weber (apart from the whole Forzebra team) in the construction/characterization of movement devices, working with the pulse sequences and imaging the animal.

Selected Publications - Sairamesh Raghuraman

Journal Publications

S. Raghuraman, J.Schrauth, D.Weber, F.Resmer, M. Haddad-Weber, F. Breuer, U. Noth, P.Jakob, T. Lanz, D.Haddad, "Dynamic MR imaging of a minipig's knee using a high-density multi-channel receive array and a movement device", *Magnetic Resonance Materials in Physics, Biology and Medicine"*, vol. 26, Issue 2, pp 215-228, 2013.

S.Raghuraman, M.Mueller, S.Zbyn, P.Baer, F.Breuer, K.Friedrich, S.Trattnig, T.Lanz, P.Jakob, "12-channel receive array with a volume transmit coil for hand/wrist imaging at 7 T", *Journal of Magnetic Resonance Imaging*, vol. 38, pp. 238-244, 2013.

Poster Presentations

S.Raghuraman, J.Schrauth, D. Weber et. al., "Dynamic imaging of a minipig's knee using a multi-channel array and a movement device", Proc. ISMRM 2011.

A.Kuehne, H.Waiczies, **S.Raghuraman** et. al., "A comparison of FDTD solvers for simulation of a birdcage coil at 1.5 T", Proc. ISMRM 2011.

S.Raghuraman, M.F.Mueller, M. Sauer et. al. "Variation of Noise correlation and SNR with subtle changes in overlap", Proc. ESMRMB 2011.

S.Raghuraman, F.Resmer, M.F.Mueller et.al., "A 12 channel receive array with a volume transmit coil for hand/wrist imaging at 7 T"', Proc. ESMRMB 2011.

D.Weber, S.Klum, **S.Raghuraman** et. al., "Fast Dynamic Multislice MRI of human knee using a motion device", Proc. ISMRM 2011.

E.Munz, A.Hopfgartner, **S.Raghuraman** et. al., "Motino tracking: Fast high resolution 2D motion quantification and depiction of shivering", Proc. ISMRM 2012.

S.Raghuraman, F.Resmer, M.F.Mueller et. al., "A volume coil and a multichannel receive array for high resolution hand/wrist imaging at 7 T", Proc. ISMRM 2012.